Nanoscale

ROYAL SOCIETY OF CHEMISTRY

REVIEW

View Article Online
View Journal | View Issue

Check for updates

**Cite this:** *Nanoscale*, 2024, **16**, 18165

# Structurally and surficially activated $TiO_2$ nanomaterials for photochemical reactions

Si Yin Tee, *[a] Junhua Kong, [a] Justin Junqiang Koh,[a] Choon Peng Teng,[a] Xizu Wang,[a] Xiaobai Wang,[a] Siew Lang Teo,[a] Warintorn Thitsartarn,[a] Ming-Yong Han*[b] and Zhi Wei Seh *[a]

Renewable fuels and environmental remediation are of paramount importance in today's world due to escalating concerns about climate change, pollution, and the finite nature of fossil fuels. Transitioning to sustainable energy sources and addressing environmental pollution has become an urgent necessity. Photocatalysis, particularly harnessing solar energy to drive chemical reactions for environmental remediation and clean fuel production, holds significant promise among emerging technologies. As a benchmark semiconductor in photocatalysis, $TiO_2$ photocatalyst offers an excellent solution for environmental remediation and serves as a key tool in energy conversion and chemical synthesis. Despite its status as the default photocatalyst, $TiO_2$ suffers from drawbacks such as a high recombination rate of charge carriers, low electrical conductivity, and limited absorption in the visible light spectrum. This review provides an in-depth exploration of the fundamental principles of photocatalytic reactions and presents recent advancements in the development of $TiO_2$ photocatalysts. It specifically focuses on strategic approaches aimed at enhancing the performance of $TiO_2$ photocatalysts, including improving visible light absorption for efficient solar energy harvesting, enhancing charge separation and transportation efficiency, and ensuring stability for robust photocatalysis. Additionally, the review delves into the application of photodegradation and photocatalysis, particularly in critical processes such as water splitting, carbon dioxide reduction, nitrogen fixation, hydrogen peroxide generation, and alcohol oxidation. It also highlights the novel use of $TiO_2$ in plastic polymerization and degradation, showcasing its potential for converting plastic waste into valuable chemicals and fuels, thereby offering sustainable waste management solutions. By addressing these essential areas, the review offers valuable insights into the potential of $TiO_2$ photocatalysis for addressing pressing environmental and energy challenges. Furthermore, the review encompasses the application of $TiO_2$ photochromic systems, expanding its scope to include other innovative research and applications. Finally, it addresses the underlying challenges and provides perspectives on the future development of $TiO_2$ photocatalysts. Through addressing these issues and implementing innovative strategies, $TiO_2$ photocatalysis can continue to evolve and play a pivotal role in sustainable energy and environmental applications.

Received 5th June 2024,
Accepted 8th September 2024

DOI: 10.1039/d4nr02342k

rsc.li/nanoscale

## 1 Introduction

Photocatalysis stands as a promising solution for addressing a wide array of environmental and energy-related challenges by facilitating photochemical catalytic reactions. This process harnesses the abundant and renewable energy of sunlight to drive chemical transformations without requiring additional energy input, thereby positioning it as an attractive avenue for diverse applications. Typically, photocatalysis employs a semiconductor photocatalyst that absorbs photons, generating active electron–hole pairs upon exposure to light. This photoexcitation leads to the generation of electrons in the conduction band (CB) and electronic vacancies or holes in the valence band (VB). Among the numerous photocatalysts derived from a variety of semiconducting materials, including metal oxides,[1] oxysulfides,[2] metal sulfides,[3] oxynitrides,[4] and their composites,[5] metal oxides hold particular importance due to their favorable band gap and band edge positions. Notably, $TiO_2$ has emerged as one extensively studied semiconductor in photocatalysis due to its exceptional optical and electronic properties, as well as its unique chemical and physical character-

---

[a] *Institute of Materials Research and Engineering (IMRE), Agency for Science, Technology and Research (A*STAR), 2 Fusionopolis Way, Innovis #08-03, Singapore 138634, Republic of Singapore. E-mail: teesyi@imre.a-star.edu.sg, sehzw@imre.a-star.edu.sg*
[b] *Institute of Molecular Plus, Tianjin University, Tianjin 300072, China. E-mail: han_mingyong@tju.edu.cn*

istics facilitating a broad spectrum of reactions under solar irradiation. Since its pioneering role in photo-assisted water splitting in the early 1970s,[6] $TiO_2$ has garnered significant attention as a photocatalyst, leading to extensive research into the fabrication, structure, and applications of nanostructured $TiO_2$-based photocatalysts.[7,8] These photocatalysts have found widespread consideration for numerous processes, such as environmental purification,[9–12] water splitting,[13,14] carbon dioxide reduction,[15,16] nitrogen fixation,[17,18] hydrogen peroxide generation,[19,20] alcohol oxidation,[21,22] and many more.

However, despite its remarkable properties, the widespread utilization of $TiO_2$ in photocatalytic applications faces inherent limitations. A primary challenge arises from its relatively large band gap of 3.2 eV, necessitating the use of high-energy photons for activation, primarily in the ultraviolet (UV) region below 400 nm, which represents only a small fraction of the total solar spectrum. Consequently, $TiO_2$ photocatalysts exhibit limited efficiency under natural sunlight conditions, with a substantial portion of solar energy remaining untapped. Moreover, $TiO_2$ is constrained by rapid recombination of electron–hole pairs, resulting in lifetimes typically ranging from $10^{-12}$ to $10^{-11}$ seconds, further diminishing its photocatalytic performance. To overcome these challenges, substantial efforts have been directed towards extending the working spectrum of $TiO_2$ photocatalysts into the visible light range, which accounts for 45% of total solar energy, and enhancing their charge carrier separation capabilities. Various approaches have thus been explored, aiming to unlock the full potential of $TiO_2$ photocatalysts for solar-driven processes, including bandgap engineering, surface modification, defect engineering, nanostructuring, and hybridization.

(I) Band gap engineering involves modifying the electronic structure of $TiO_2$ to shift its band gap, typically achieved through doping with metal or non-metal ions. This introduces donor or acceptor states below or above the conduction or valence bands, respectively, enabling electronic transitions with lower energy compared to pure $TiO_2$. As a result, visible light absorption and photocatalytic activity are enhanced.[23] (II) Surface modification of $TiO_2$, through functionalization or nanoparticle deposition, creates localized energy states within the band gap.[24] For instance, deposition of noble metals like Pt or Au can trap visible light and enhance charge separation, thereby improving photocatalytic activity under visible light irradiation.[24] (III) Defect engineering through introducing hydrogen to $TiO_2$ can create oxygen vacancies and modify its electronic structure, narrowing the band gap and improving visible light absorption.[25] (IV) Nanostructuring $TiO_2$ at the nanoscale can create quantum confinement effects or surface defects, modifying its electronic properties and band gap.[26] With the large surface-to-volume ratio of nanomaterials, abundant surface reaction sites are offered, potentially modulating the catalytic activity of surface atoms and leading to improved catalytic performance.[27–30] (V) Hybridization techniques for $TiO_2$ involve forming composites with various materials such as graphitic carbon nitride, MXenes, metal–organic frameworks, and aerogels. These materials are integrated with $TiO_2$ to enhance its photocatalytic performance by leveraging their unique properties. For instance, graphitic carbon nitride can improve visible light absorption,[31] MXenes can enhance conductivity and charge separation,[32] metal–organic frameworks can provide high surface area and tunable porosity,[33] and aerogels can offer lightweight structures with high surface area.[34] By combining $TiO_2$ with these materials, hybrid composites can achieve superior light absorption, increased charge carrier separation, and improved catalytic activity, addressing the limitations of pure $TiO_2$.

In light of the significant research advancements in the field of $TiO_2$, a brief search of the literature in the Web of Science database for "$TiO_2$" returns over 260 000 results, demonstrating the extensive interest and investigation in this

**Si Yin Tee**

*Si Yin Tee obtained her PhD in Biomedical Engineering from National University of Singapore. Currently, she is working as a research scientist at the Institute of Materials Research and Engineering, A*STAR. Her research focuses on the development of functional metal and semiconductor nanostructures for biomedical, environmental and energy applications.*

**Ming-Yong Han**

*Ming-Yong Han has served at National University of Singapore, Institute of Materials Research and Engineering, and Tianjin University. Throughout his career, Ming-Yong Han has passionately tackled interdisciplinary challenges at the intersections of nanoscience, nanotechnology, biotechnology, and energy/biomedical applications. His contributions are extensive, encompassing the publication of ∼300 papers with ∼30 000 citations (h-index 80) and ∼300 research highlights. He has been honored as a Fellow of the Royal Society of Chemistry (FRSC) and has been recognized as a highly cited researcher in the Web of Science/Scopus.*

material. When specifically searching for "$TiO_2$ photocatalyst", the results narrow to over 30 000, indicating the focused research on its photocatalytic properties. However, this number may still underrepresent the true scope, as many relevant studies might not explicitly label $TiO_2$ as a photocatalyst. This extensive body of research highlights the critical importance of $TiO_2$ in the field of photocatalysis, underlining its significant role and impact in advancing environmental remediation and energy conversion technologies over several decades.

For a quick overview of the research history, we present a brief timeline of milestones in the development of $TiO_2$ photocatalysts for various applications (Fig. 1). The first investigation of $TiO_2$ as a photocatalyst began in the 1970s when it was identified as a semiconductor capable of splitting water under UV light. During the 1980s and 1990s, significant advancements in doping techniques enhanced its photocatalytic efficiency under visible light. The early 2000s introduced engineered nanostructures and facets, which further improved $TiO_2$'s performance. In the 2010s, research focused on defect engineering and developing heterojunctions and composite/hybrid materials, incorporating $TiO_2$ with other semiconductors and noble metals to boost its photocatalytic activity. Recent years have seen progress in single-atom co-catalysts, with atomically dispersed metal atoms on $TiO_2$ tuning active sites, selectivity, and stability. Moving forward, 3D printing technology has enabled the creation of complex $TiO_2$ nanostructures with favorable properties for photochemical reactions. These advancements have expanded $TiO_2$'s applications in environmental remediation and energy conversion, with photoreforming waste polymers into sustainable hydrogen fuel and chemical feedstock marking a significant leap in waste-to-energy technology.

This review provides a comprehensive and interdisciplinary perspective on the advancements in $TiO_2$ photocatalysts, bridging materials science, chemistry, environmental science, and engineering to offer a holistic understanding of their diverse applications. Going beyond general advancements, this review offers a detailed analysis of specific techniques such as doping, metal nanoparticle incorporation for surface plasmon resonance, morphological control, and hybridization. These approaches target three main steps: improving visible light absorption for efficient solar energy harvesting, enhancing charge separation and transportation efficiency, and maximizing charge utilization while ensuring good stability for robust photocatalysis. Recent progress includes the development of single-atom co-catalysts, advanced heterojunctions, and sophisticated 3D printing technologies for creating complex $TiO_2$ nanostructures.

These developments have significantly broadened $TiO_2$'s applications. In the realm of environmental remediation, $TiO_2$ photocatalysts have shown significant promise in breaking down pollutants under visible light, making them viable for water and air purification processes. Their antibacterial properties also present opportunities for public health improvements. For sustainable energy production, $TiO_2$ has been explored extensively for water splitting, which generates hydrogen as a clean fuel. In addition, it is used for carbon dioxide reduction, converting carbon dioxide into valuable fuels, and nitrogen fixation, which is critical for producing ammonia for fertilizers.

Emerging applications such as hydrogen peroxide generation and alcohol oxidation are also discussed, illustrating the broadening scope of $TiO_2$ photocatalysis. The review delves into the novel application of $TiO_2$ in plastic polymerization and degradation processes. Here, $TiO_2$ photocatalysts facilitate the breakdown of plastic waste into valuable chemicals and fuels, offering a sustainable approach to waste management and resource recovery. Recent research highlights the potential of photocatalytic depolymerization of various plastics and the conversion of plastic-derived intermediates into useful products, addressing plastic pollution and promoting circular economy principles (Fig. 2).

Finally, the review presents a summary and outlook on the major challenges and promising perspectives for future research in $TiO_2$ photocatalysts. Overall, the advancements in $TiO_2$-based photocatalysts are anticipated to provide robust solutions to some of the most pressing energy and environmental challenges facing society today. The review highlights the transformative potential of $TiO_2$ photocatalysts in addressing these global issues and sets a clear roadmap for future research directions aimed at maximizing their efficiency and practical applicability.

## 2 Photochemical reactions of $TiO_2$ nanomaterials

$TiO_2$ occurs in nature in three distinct polymorphs: rutile, anatase, and brookite, with rutile being the most abundant followed by anatase and then brookite. In all three forms of $TiO_2$,

**Zhi Wei Seh**

*Zhi Wei Seh is a Senior Principal Scientist at the Institute of Materials Research and Engineering, A*STAR. He received his BS and PhD degrees in Materials Science and Engineering from Cornell University and Stanford University, respectively. His research interests lie in the design of new battery materials beyond lithium-ion technology. As a Highly Cited Researcher, he is widely recognized for designing the first yolk–shell nanostructure in lithium–sulfur batteries, which is a licensed technology. He pioneered the first study of sodium dendrites using cryogenic TEM, and the first anode-free magnesium battery with five times the energy density of standard magnesium batteries.*

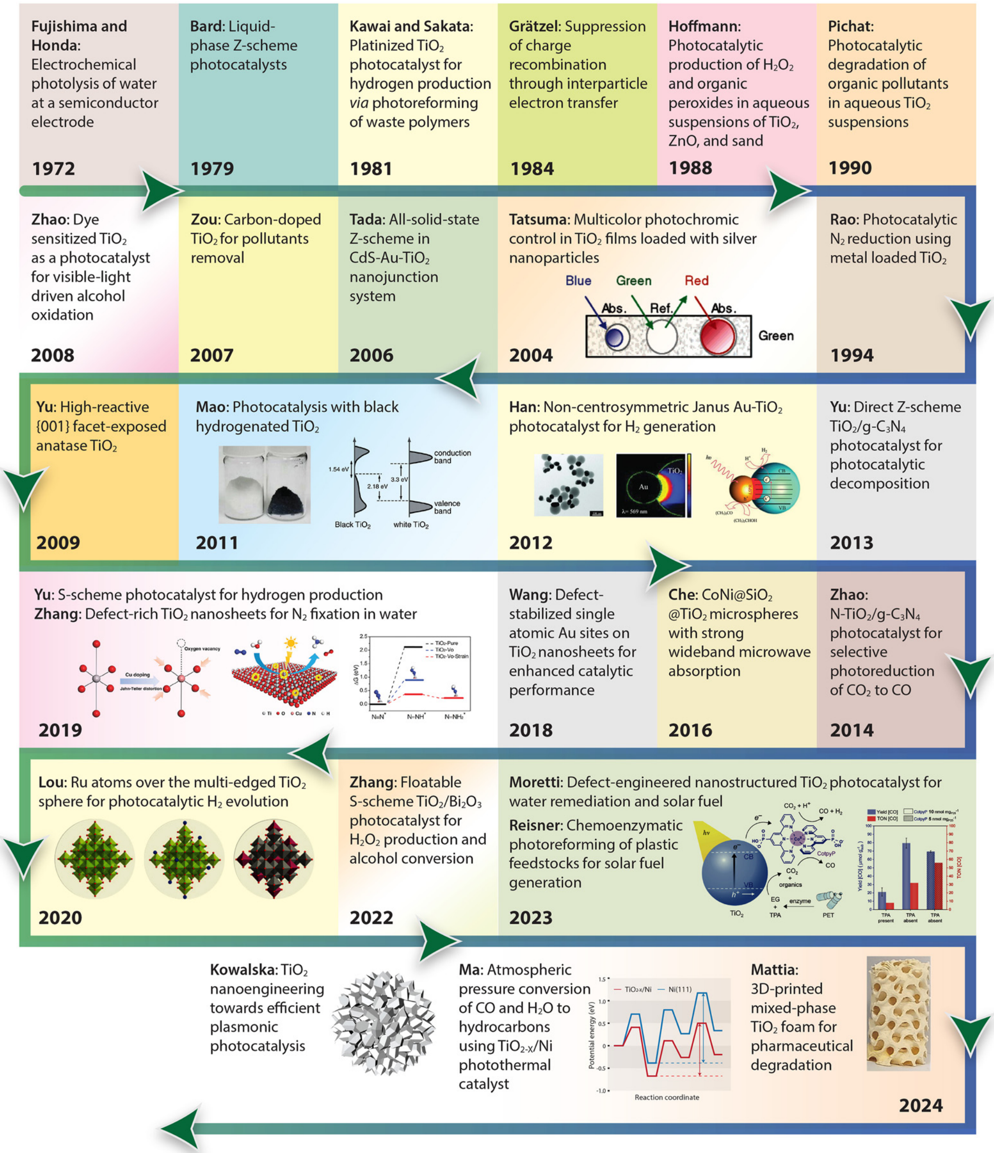

**Fig. 1** Timeline of milestones in $TiO_2$ nanomaterials development, highlighting continuous advancements and innovations in the field. 1972, Fujishima and Honda: Electrochemical photolysis of water at a semiconductor electrode.[35] 1979, Bard: Liquid-phase Z-scheme photocatalysts.[36] 1981, Kawai and Sakata: Platinized $TiO_2$ photocatalyst for hydrogen production *via* photoreforming of waste polymers.[37] 1984, Grätzel: Suppression of charge recombination through interparticle electron transfer.[38] 1988, Hoffmann: Photocatalytic production of $H_2O_2$ and organic peroxides in aqueous suspensions of $TiO_2$, ZnO, and sand.[39] 1990, Pichat: Photocatalytic degradation of organic pollutants in aqueous $TiO_2$ suspensions.[40] 1994, Rao: Photocatalytic $N_2$ reduction using metal loaded $TiO_2$.[41] 2004, Tatsuma: Multicolor photochromic control in $TiO_2$ films loaded with silver nanoparticles. Reproduced with permission from ref. 42. Copyright 2004, American Chemical Society. 2006, Tada: All-solid-state Z-scheme in CdS-Au-$TiO_2$ nanojunction system.[43] 2007, Zou: Carbon-doped $TiO_2$ for pollutants removal.[44] 2008, Zhao: Dye sensitized $TiO_2$ as a photocatalyst for visible-light driven alcohol oxidation.[45] 2009, Yu: High-reactive (001) facet-exposed anatase $TiO_2$.[46] 2011, Mao: Photocatalysis with black hydrogenated $TiO_2$. Reproduced with permission from ref. 25. Copyright 2011, American Association for the Advancement of Science. 2012, Han: Non-centrosymmetric Janus Au-$TiO_2$ photocatalyst for $H_2$ generation Reproduced with permission from ref. 13. Copyright 2012, Wiley-VCH. 2013, Yu: Direct Z-scheme $TiO_2$/g-$C_3N_4$ photocatalyst for photocatalytic decomposition.[47] 2014, Zhao: N-$TiO_2$/g-$C_3N_4$ photocatalyst for selective photoreduction of $CO_2$ to CO.[48] 2016, Che: CoNi@$SiO_2$ @$TiO_2$ microspheres with strong wideband microwave absorption.[49] 2018, Wang: Defect-stabilized single atomic Au sites on $TiO_2$.[50] 2019, Yu: S-scheme photocatalyst for hydrogen production.[51] 2019, Zhang: Defect-rich $TiO_2$ nanosheets for $N_2$ fixation in water. Reproduced with permission from ref. 52. Copyright 2019, Wiley-VCH. 2020, Lou: Ru atoms over the multi-edged $TiO_2$ sphere for photocatalytic $H_2$ evolution. Reproduced with permission from ref. 53. Copyright 2020, American Association for the Advancement of Science. 2022, Zhang: Floatable S-scheme $TiO_2$/$Bi_2O_3$ photocatalyst for $H_2O_2$ Production and alcohol conversion.[54] 2023, Moretti: Defect-engineered nanostructured $TiO_2$ photocatalyst for water remediation and solar fuel.[55] 2023, Reisner: Chemoenzymatic photoreforming of plastic feedstocks for solar fuel generation. Reproduced with permission from ref. 56. Copyright 2023, Wiley-VCH. 2024, Mattia: 3D-printed mixed-phase $TiO_2$ foam for pharmaceutical degradation. Reproduced with permission from ref. 57. Copyright 2024, Royal Society of Chemistry. 2024, Ma: Atmospheric pressure conversion of CO and $H_2O$ to hydrocarbons using $TiO_{2-x}$/Ni photothermal catalyst.[58] 2024, Kowalska: $TiO_2$ nanoengineering towards efficient plasmonic photocatalysis. Reproduced with permission from ref. 59. Copyright 2024, Elsevier.

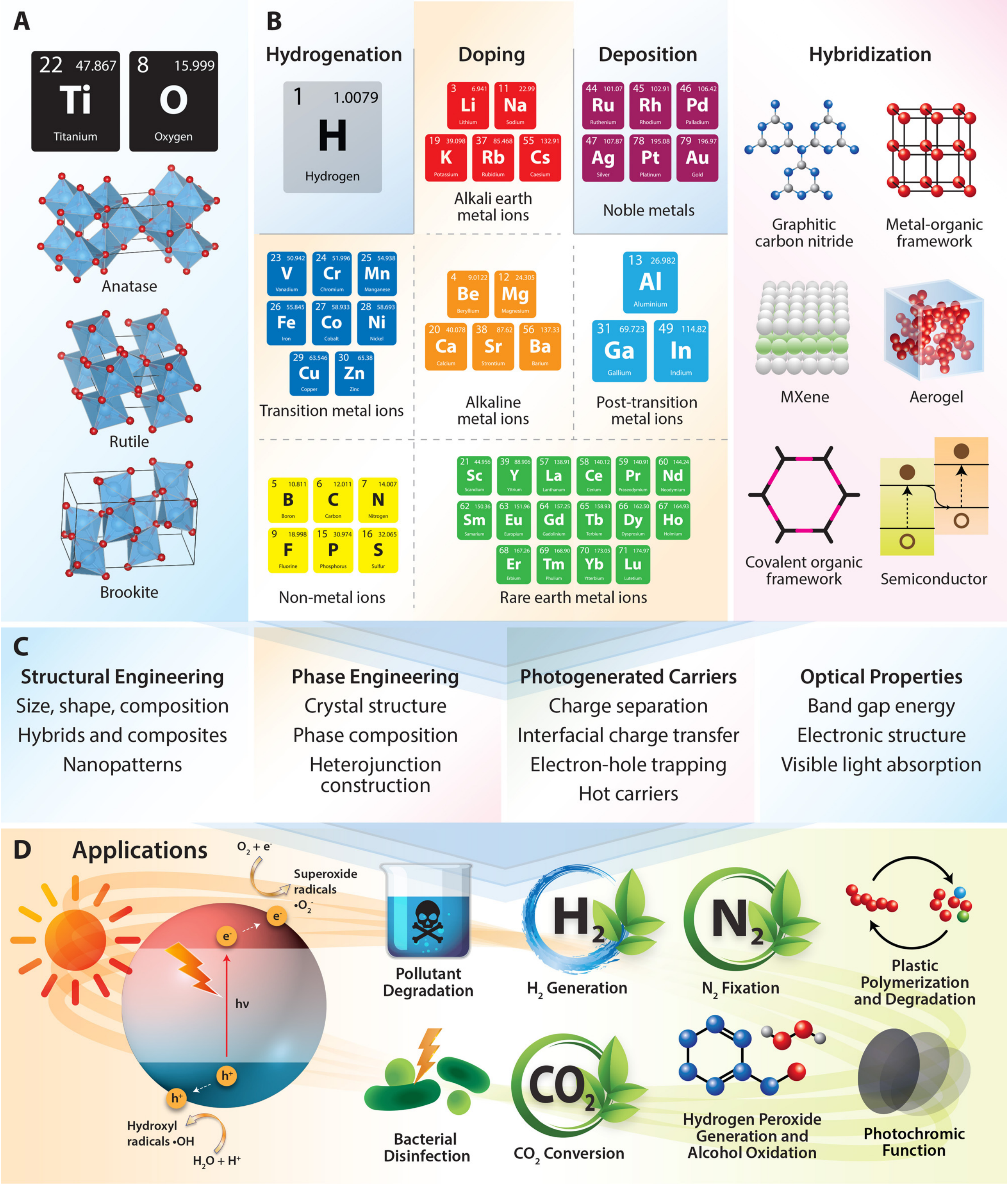

**Fig. 2** An overview on modification strategies of $TiO_2$ for photocatalytic applications. (A) Crystal structures of $TiO_2$ in anatase, rutile, and brookite phases. (B and C) Modification strategies used to optimize structural, electronic, and surface properties of $TiO_2$ semiconductor. Key techniques include hydrogenation (defect engineering), ion-doping (metal/non-metal), noble metal deposition, and hybridization/compositing with other materials. (D) Schematic illustration of the mechanism of $TiO_2$ photocatalysis for applications in environmental remediation, bacterial disinfection, hydrogen generation, carbon dioxide reduction, nitrogen fixation, hydrogen peroxide generation, alcohol oxidation, photochromic functions, plastic polymerization and degradation.

the $TiO_6$ octahedra exhibit distortion, with titanium ions coordinated to six oxygen ions. In anatase, the $TiO_6$ octahedra are arranged in a tetragonal structure where each octahedron shares four edges with neighboring octahedra but lacks corners. This unique configuration results in a lattice with specific characteristics such as high surface area and excellent photocatalytic activity. Rutile also features a tetragonal structure, albeit with a different alignment of the $TiO_6$ octahedra. In rutile, each octahedron shares two opposing edges to create linear chains in the (001) direction, which are interconnected at their corners, leading to a denser crystal lattice compared to anatase. Brookite's orthorhombic crystal structure is distinguished by octahedra sharing three edges and three corners, resulting in a more intricate lattice structure compared to anatase and rutile. Among these polymorphs, rutile is the most thermodynamically stable phase of $TiO_2$, while anatase and brookite are metastable phases that can transition into rutile at elevated temperatures.[60,61] The varied properties and functionalities of these $TiO_2$ polymorphs establish them as essential materials in photochemical reactions (refer to Table 1).

$TiO_2$ photocatalytic reactions rely on the fundamental generation of electron–hole pairs through photoexcitation. When $TiO_2$ is exposed to UV light, electron–hole pairs are generated between the valence band (VB) and conduction band (CB). These pairs subsequently migrate to the surface of the $TiO_2$, where they either undergo recombination and release the energy as heat, become trapped in metastable surface states, or interact with adsorbed electron donors/acceptors. In photodegradation reactions, the holes can directly react with organic compounds or oxidize water to produce hydroxyl radicals ($^{\bullet}OH$), initiating an oxidative process that leads to the breakdown of organic compounds. Meanwhile, the electrons can react with organic compounds to form reduction products or with molecular oxygen to generate superoxides ($^{\bullet}O_2^-$), which can trigger the formation of various reactive oxygen species (*e.g.*, $^{\bullet}O_2^-$, $^{\bullet}OH$, $H_2O_2$, *etc.*).[62] These photogenerated reactive oxidative species play a crucial role not only in degrading organic compounds but also in the photocatalytic inactivation of bacteria by oxidizing their cell walls and inducing cell lysis. In aerobic conditions, bacterial cells are inactivated through oxidation, whereas in anaerobic conditions, bacterial cells are inactivated through reduction, with the cells capable of trapping the electrons to prevent charge recombination.[63]

When a photocatalyst is utilized for water splitting to generate hydrogen, it is essential that the conduction band (CB) level is more negative than the reduction potential of $H^+$ to $H_2$ (0 V *vs.* NHE at pH 0), and the valence band (VB) should be more positive than the oxidation potential of $H_2O$ to $O_2$ (1.23 V *vs.* NHE). This requirement indicates that a minimum photon energy of 1.23 eV is needed to facilitate photocatalytic water splitting, corresponding to a wavelength of approximately 1000 nm. However, an activation barrier exists in the charge transfer process between the solid photocatalyst and water molecules, necessitating a photon energy exceeding the band gap of the photocatalyst to effectively split pure water at a reasonable rate.[14]

In the realm of carbon dioxide reduction, the process involves converting carbon dioxide into valuable chemical products like hydrocarbons or synthetic fuels by leveraging the reactivity of electron–hole pairs generated by the photocatalyst. The photocatalytic reduction of carbon dioxide with $TiO_2$ entails a series of steps facilitated by photoexcited charge carriers. Upon light exposure, $TiO_2$ absorbs photons, creating electron–hole pairs that migrate to the semiconductor's surface. Carbon dioxide molecules adsorb onto the $TiO_2$ surface, where photoexcited electrons can reduce them to form various carbon-based products such as carbon monoxide (CO), methane ($CH_4$), or formic acid (HCOOH). This reduction process involves multiple proton–electron transfer steps, followed by the release of the newly formed carbon-based products from the $TiO_2$ surface into the environment.[64]

**Table 1** Overview of pristine $TiO_2$ photocatalyst in environmental remediation applications

| Photocatalysts | Synthesis methods | Pollutants | Degradation efficiency | Ref. |
|---|---|---|---|---|
| $TiO_2$ nanosheets | Solvothermal | Rhodamine B | >90% in 15 min under UV light | 250 |
| $TiO_2$ nanorods | Hydrothermal | *p*-Cresol | >90% in 75 min under UV-visible light | 267 |
| $TiO_2$ nanostructures | Hydrothermal | Rhodamine B | >90% in 150 min under UV light | 251 |
| $TiO_2$ nanotubes | Hydrothermal | Orange II | 89.46% in 2000 min under UV light | 392 |
| $TiO_2$ nanotubes | Electrochemical anodization | Volatile organic compounds | 72.1% in 30 min under UV-LED | 393 |
| $TiO_2$ nanotubes | Electrochemical anodization | β-Blocker metoprolol | 87.09% (milli-water) and 62.05% (tap water) in 120 min under UV-LED | 394 |
| $TiO_2$ nanotubes | Hydrothermal | $H_2S$ | 10 ppm to 1.0 ppb in 3 h under UV light | 395 |
| Mesoporous $TiO_2$ nanoshell@ polyimide nanofibers | *In situ* complexation-hydrolysis | Methylene blue | 95% in 40 min under UV light | 396 |
| Nano flower-like rutile $TiO_2$ | Hydrothermal | Methylene blue | 98.95% in 180 min under solar light | 252 |
| Raschig rings-supported $TiO_2$ | Sol–gel | Rhodamine 6G | 91% in 30 min under UV light | 397 |
| $TiO_2$ films | Magnetron sputtering | (i) Methylene blue,<br>(ii) *E. coli* bacteria | (i) 45% in 8 h under UVB light,<br>(ii) >90% in 45 min under UVB light | 280 |
| $TiO_2$ sheets | Chemical synthesis/hydrogenation | Rhodamine B | 99% in 75 min under simulated solar light | 398 |
| $TiO_2$ hollow spheres | Hard template-based approach | Ciprofloxacin | 82% in 6 h under simulated solar light with AM1.5G filter, 100 W Xe arc lamp | 55 |
| $TiO_2$ particles | Ultrasound assisted sol–gel | Metformin | 75.4% in 120 min under UV light | 61 |

Similarly, in nitrogen fixation, electron–hole pairs play a pivotal role in catalyzing the reduction of nitrogen molecules to produce ammonia, a critical component in fertilizers and various chemical processes. The thermodynamically non-spontaneous reaction ($N_2 + 3H_2O \rightarrow 2NH_3 + 1.5O_2$), which combines water splitting and nitrogen fixation, can be accomplished with solar energy input. The photocatalytic process of nitrogen fixation can be delineated into multiple stages. Initially, photogenerated electrons are promoted to the CB, creating vacancies (or holes) in the VB. Subsequently, some of these electrons and holes may recombine, while others migrate to the catalyst surface to participate in redox reactions. Specifically, water can be oxidized to oxygen by the holes, whereas nitrogen is reduced to form ammonia through successive transfers of photogenerated electrons and protons sourced from water.[17]

## 3 Modification of electronic structures by doping

Despite significant advancements in the design and improvement of $TiO_2$ photocatalysts, challenges persist when using pure $TiO_2$ due to its low quantum efficiency and limited utilization of visible light. To address these challenges, considerable efforts have been directed towards modifying the electronic structure of $TiO_2$ to shift its absorption into the visible range and enhance its photocatalytic performance. One approach involves doping, which introduces permissible electronic states between the CB and VB by incorporating metal ion (Table 2) and non-metal ion (Table 3) dopants. It is well-known that metal ions incorporated into the $TiO_2$ lattice typically introduce donor states below the conduction band, while non-metal ions contribute to the formation of acceptor states above the valence band (Fig. 3A). These donor and acceptor states play crucial roles in altering the electronic structure of $TiO_2$, affecting its band gap and, consequently, its optical and photocatalytic properties.[62,65] In this section, we outline recent progress in fabricating various $TiO_2$ semiconductors to enhance photoconversion efficiency in the visible light region, employing strategies such as doping with metal ions and non-metal ions.

### 3.1 Metal ions

Metal-ion doping of $TiO_2$ involves the introduction of metal ions into the $TiO_2$ lattice structure to modify its properties. This helps reduce carrier recombination by creating electron trap centers, ultimately enhancing its photocatalytic activity.[66] Various metal ions such as alkali, alkaline earth, transition, and rare-earth can be incorporate into the $TiO_2$ matrix to alter its electronic structure and tailor its photocatalytic activity.

**3.1.1 Alkali earth metal ions.** Doping $TiO_2$ with alkali earth metal ions involves introducing ions like lithium, sodium, potassium, rubidium, and caesium into the $TiO_2$ lattice structure. Alkali metal doping, especially with ions like $Li^+$, has demonstrated potential in improving the photocatalytic properties of $TiO_2$. This enhancement is attributed to several mechanisms, including the reduction of crystallite size, improved crystallinity, and decreased recombination of generated charges.[67] Sodium doping had been known to cause sodium poisoning which degrades the photocatalytic property of $TiO_2$.[68] Accordingly, low sodium content may serve as a recombination center, while higher sodium content favors the formation of brookite or sodium titanate, which are less photoactive than $TiO_2$ in its anatase form.[69] Report suggested that the poisoning effect may arise from a combination of various contaminants, including calcium, potassium, and magnesium, found on glass surfaces rather than solely from sodium doping.[70] Interestingly, sodium doping has been shown to enhance photocatalytic activity in some reports, compared to both the synthesized $TiO_2$ nanopowder and commercially available P25 $TiO_2$. The enhancement was made possible through the com-

**Table 2** Overview of metal-doped $TiO_2$ photocatalyst in environmental remediation applications

| Photocatalysts | Synthesis methods | Pollutants | Degradation efficiency | Ref. |
|---|---|---|---|---|
| Na–$TiO_2$ nano-powder | Sol–gel | Methylene blue | 92.5% in 60 min under UV light, peak $\lambda_{max}$ = 365 nm | 72 |
| Na–$TiO_2$ nanotubes | Electrochemical anodization | Methylene blue | 97.3% in 180 min under solar light | 73 |
| Rb–$TiO_2$ nanoparticles | Sol–gel | Methylene blue | 97% in 60 min under UV light | 77 |
| Mg–$TiO_2$ nanoparticles | Sol–gel | Methyl orange | 47.82% in 120 min under UV light | 80 |
| Ca–$TiO_2$ nanofibers | Sol–gel electrospinning | Rhodamine B | 95% in 100 min under UV light | 399 |
| Ba–$TiO_{2-x}$ ($x$ = 5%) | Template assisted synthesis | Rhodamine B | 99.4% in 30 min under simulated solar light | 400 |
| Ba–$TiO_2$ quantum dots | Co-precipitation | Methylene blue | 99.5% in 120 min under visible light | 81 |
| Fe–$TiO_2$ nanoparticles | Sol–gel | Methyl orange | 98% in 60 min under visible light | 88 |
| Fe–$TiO_2$ nanoparticles | Electrospray-assisted flame spray pyrolysis | *Escherichia coli* | 99.4% in 5 h under UV light | 87 |
| In–$TiO_2$ nanoparticles | Sol–gel | $H_2S$ | 100% in 120 min under UV light | 85 |
| Mo–$TiO_2$ particles | Sol–gel/underwater plasma | Rhodamine B | 96% in 60 min under visible light | 256 |
| W–$TiO_2$ particles | Sol–gel/underwater plasma | Rhodamine B | 96% in 60 min under visible light | 256 |
| Tb–$TiO_2$ coating | Plasma electrolytic oxidation | Methyl orange | 75% in 12 h under simulated sunlight | 92 |
| Nd–$TiO_2$ nanoparticles | Sol–gel | Methyl orange | 96.5% in 120 min under simulated sunlight | 91 |
| Eu–$TiO_2$ nanorods | Hydrothermal | Methyl orange | 100% in 20 min under simulated sunlight | 89 |
| Er–Ce co-doped $TiO_2$ nanoparticles | Sol–gel | (i) *Staphylococcus aureus*, (ii) *E. coli* | (i) 91.23% and (ii) 92.8% in 20 min under simulated double solar radiation | 281 |

**Table 3** Overview of non-metal doped $TiO_2$ photocatalyst in environmental remediation applications

| Photocatalysts | Synthesis methods | Pollutants | Degradation efficiency | Ref. |
|---|---|---|---|---|
| B–$TiO_2$ particles | Sol–gel | (i) Diuron, (ii) *o*-phenylphenol, (iii) 2-methyl-4-chlorophenoxy-acetic acid, (iv) terbuthylazine | (i) and (ii) 70–80% in 120 min, (iii) >90% in 45 min, (iv) 50% in 120 min under solar light | 271 |
| B–$TiO_2$ nanoparticles | Solvothermal | (i) 2,4-Dichloro-phenol, (ii) bisphenol-A, (iii) ibuprofen & flurbiprofen | (i) 75.1% in 5 h, (ii) 97.7% in 4 h, (iii) 81–85% in 5 h under visible light | 275 |
| B–$TiO_2$ nanocrystals | Electrochemical anodization/hydrothermal | Rhodamine B | >90% in 60 min under visible light | 401 |
| B–$TiO_2$ nanoparticles | Co-precipitation | Rhodamine B | >90% in 90 min under visible light | 99 |
| C–$TiO_2$ particles | Controlled hydrolysis | Caffeic acid | >90% in 120 min under visible light | 402 |
| C–$TiO_2$ core–shell nanostructures ($TiO_2$@C) | *In situ* polymer, Encapsulation–graphitization | Methylene orange | >90% in 30 min under UV light | 104 |
| C–$TiO_2$ single-crystal nanorods | Hydrothermal | (i) Methylene blue, (ii) Rhodamine B, (iii) *p*-Nitrophenol | (i) 98.3% in 60 min, (ii) 99.4% in 20 min, (iii) 63% in 80 min under visible light | 403 |
| C–$TiO_2$ nanoparticles | Vapour-assisted solvothermal | (i) Phenol, (ii) Methyl orange | (i) 94.6% in 75 min, (ii) >90% in 75 min under visible light | 404 |
| C–$TiO_2$ core–shell nanostructures | Sol–gel | Methylene blue | 90.1% in 120 min under visible light | 107 |
| C–$TiO_2$ nanoparticles | Hydrothermal | Rhodamine B | >90% in 120 min under UV light | 109 |
| Biochar–$TiO_2$ particles | Hydrolysis | Methyl orange | 83.23% in 150 min under UV light | 405 |
| C/C-doped $TiO_2$ hollow microsphere | Sol–gel | Rhodamine B | 96% in 140 min under UV light | 406 |
| C–nanohorns–$TiO_2$ nanoflowers | Solvothermal | Methylene blue and methyl orange | 90% in 4 h under solar light | 407 |
| N–$TiO_2$ nanoparticles | Sol–gel | Rhodamine B | 90% in 40 min under visible light | 116 |
| N–$TiO_2$ nanoparticles | Sol–gel | Methyl orange | 90% in 200 min under UV-vis light | 257 |
| N–$TiO_2$ nanoparticles | Graft polymerization | Methyl orange | 65% in 60 min under visible light | 408 |
| N–$TiO_2$ nanoparticles | Plasma-assisted electrolysis | Methyl orange | 91% in 300 min under visible light | 409 |
| N–$TiO_2$ nanoparticles | Co-precipitation | Rhodamine B | 99.2% in 540 min under visible light | 410 |
| N–$TiO_2$ nanoparticles | Solvothermal | Methylene blue | 92% in 500 min under visible light | 119 |
| P–$TiO_2$ particles | Post-phosphation | Bisphenol A | 92% in 67 min under sunlight | 411 |
| P–$TiO_2$ powders | Microwave-hydrothermal | Methylene blue | >90% in 100 min under visible light | 258 |
| P–$TiO_2$ nano-powders | Emulsion-based sol–gel | Methylene blue | >90% in 30 min under simulated solar light | 412 |
| P–$TiO_2$ nanoparticles | Solvothermal/heat treatment | Ciprofloxacin | >90% in 60 min under visible light | 277 |
| Mesoporous P–$TiO_2$ | Microwave-assisted sol–gel | Sulfamethazine | >90% in 300 min under visible light | 413 |
| P–$TiO_2$/polyacrylic composite | Sol–gel | Formaldehyde | 100% in 60 min under visible light | 90 |
| S–$TiO_2$ nanoparticles | Solvothermal | Phenol | 85.4% in 10 h under visible light | 139 |
| S–$TiO_2$ nanorods | Oxidant peroxide method assisted hydrothermal | Methyl orange and phenol | 80% in 120 min under visible light | 138 |
| S–$TiO_2$ nanoparticles | Hydrothermal | Rhodamine B | 80% in 60 min under visible light | 134 |
| S–$TiO_2$ particles | Flame spray pyrolysis | Acetaldehyde | 75% in 300 min under visible light | 137 |
| S–$TiO_2$ nanoparticles | Sol–gel | Diclofenac | 93% in 4 h under visible light | 136 |
| Meso-macroporous S–$TiO_2$ nanoparticles | Ball-milling | (i) Methylene blue, (ii) Methyl orange, (iii) 4-Nitro-phenol | (i) 98% in 100 min, (ii) 60% in 100 min, (iii) 50% in 80 min under visible light | 135 |
| F–$TiO_2$ nanorods | Hydrolysis/refluxing process | Methylene blue | 90% in 130 min under visible light | 414 |
| F–$TiO_2$ hollow spiny nanocubes | Hydrothermal/photoreduction | Phenol | 58.6% in 60 min under visible light | 143 |
| F–$TiO_2$ nanoparticles | Hydrothermal | 4-Methoxybenzyl alcohol | 56.4% in 240 min under visible light | 142 |
| F–$TiO_2$/exfoliated bentonite | Sol–gel | Toluene | 11% in 80 min under visible light | 144 |

bined effect of reduced electron–hole recombination rate, increased surface area, and enhanced crystallinity.[71–73]

For the larger alkali ions, potassium doping is considered effective for stabilizing the anatase phase of $TiO_2$, as alkaline elements promote the formation of anatase crystalline phase. Doping with potassium can control the agglomeration of $TiO_2$ particles, improve photocatalytic efficiency, enhance the adsorption of reactants on the catalyst, reduce the electron–hole recombination rate, and increase the specific surface area of $TiO_2$.[74] For instance, K-doped $TiO_2$ thin films with a concentration of 10 wt% resulted in a reduction in the optical band gap energy of $TiO_2$ from 3.5 to 3.0 eV, thereby enhancing light absorption capabilities.[75] Furthermore, the presence of hydroxyl groups on the surface of K-doped $TiO_2$ is likely to

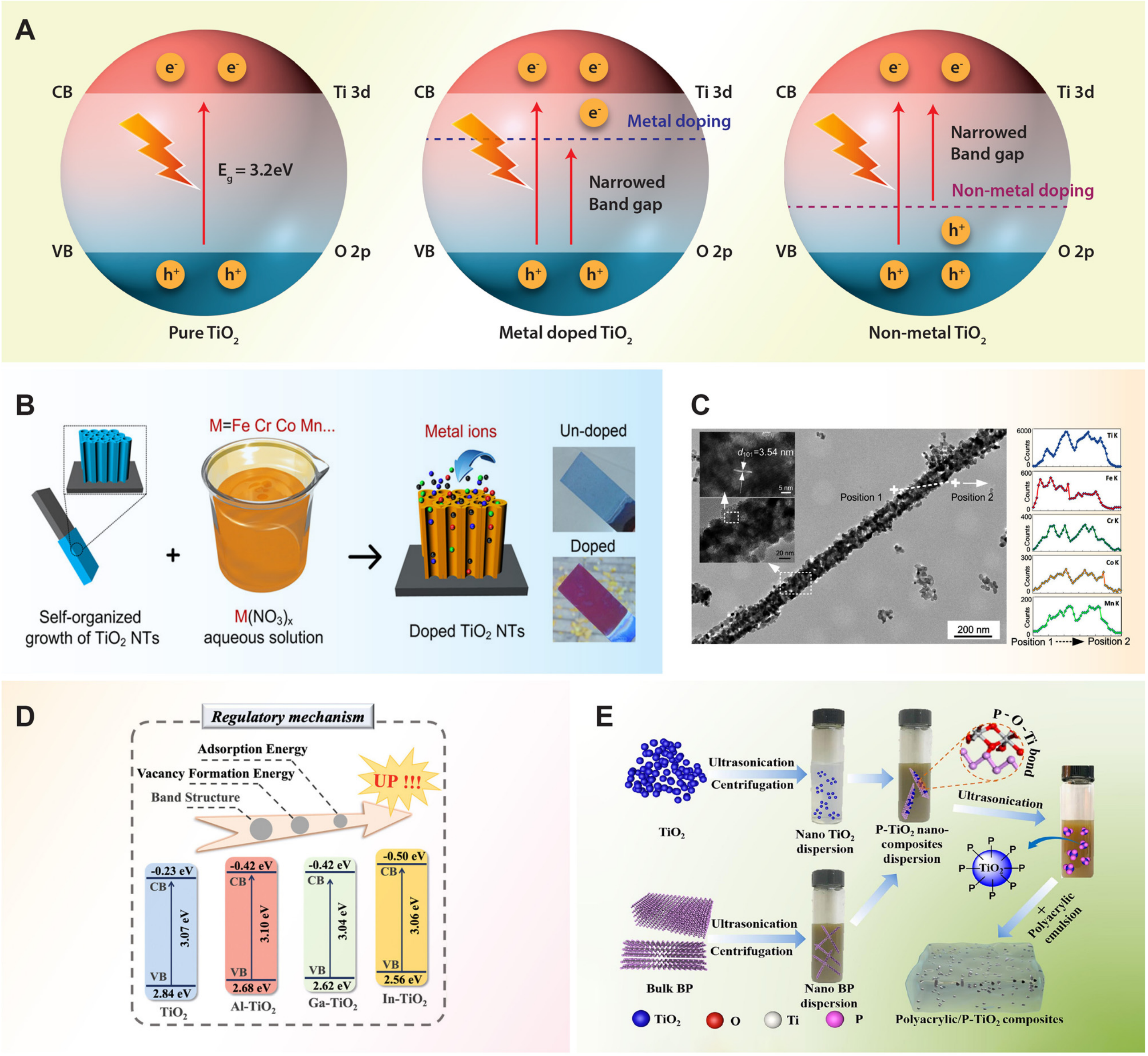

**Fig. 3** (A) Schematic diagram of photocatalytic mechanisms of pure, metal and non-metal doped $TiO_2$ semiconductor. (B) Metal ions doping of transition metal ions (Cr, Co, Fe, Mn) doped $TiO_2$ nanotubes through anodization in an aqueous solution. (C) Transmission electron microscopy (TEM) image of transition metal ion doped $TiO_2$ nanotube with corresponding elemental composition line scans. Reproduced with permission from ref. 84. Copyright 2019, American Chemical Society. (D) Band structure position of trivalent metal ions (Al, Ga, In)-doped $TiO_2$. Reproduced with permission from ref. 85. Copyright 2024, American Chemical Society. (E) Schematic illustration of fabricating phosphorus doped $TiO_2$/polyacrylic composites by using black phosphorous as the phosphate source. Reproduced with permission from ref. 90. Copyright 2024, Elsevier.

enhance its photocatalytic activity and hydrophilic properties.[76] This makes it suitable for various applications such as synthesizing water-dispersible coatings and achieving optimal photovoltaic performance. For rubidium doping, it can induce distortion in the $TiO_2$ lattice, promoting the formation of oxygen vacancies. These vacancies act as traps for capturing photo-generated electron–hole pairs, reducing their recombination rate. Furthermore, rubidium doping converts $Ti^{4+}$ into $Ti^{3+}$ through charge compensation, potentially forming impurity levels in the titania lattice that restrain carrier recombination and extend light absorption. Meanwhile, rubidium oxide on the $TiO_2$ surface can transfer and capture electrons, thereby reducing the recombination rate of photo-generated carriers.[77] Metal dopants with larger ionic radii may not substitute $Ti^{4+}$ in the $TiO_2$ lattice easily, leading them to diffuse on the surface and inhibit the growth of $TiO_2$ grains, ultimately enhancing its photocatalytic properties.[78]

**3.1.2 Alkaline earth metal ions.** Doping $TiO_2$ with alkaline earth metal ions involves introducing ions like magnesium, calcium, strontium, or barium into the $TiO_2$ lattice structure. In a comparative study of alkali and alkaline earth metal doping in Mn/$TiO_2$, it was observed that sodium, potassium, and calcium doping led to the deactivation of the photocatalyst, whereas magnesium doping enhanced the photoactivity. This suggests that alkaline earth metal doping, particularly with magnesium, provides a more significant enhancement to the photocatalytic properties of $TiO_2$.[79] Specifically, magnesium doping leads to an increase in oxygen vacancies, which can be attributed to the differences in electronegativity and ionic radius between Ti and Mg during the substitution of $Ti^{4+}$ by $Mg^{2+}$ in the lattice. These oxygen vacancies play an important role in photocatalytic reactions by serving as electron acceptors, thus reducing the recombination rate of electron–hole pairs.[80] Similarly, doping $TiO_2$ with the alkaline earth metals like strontium and barium can alter the oxide's optical absorption characteristics by modifying the band gap energy.[81,82] The dopants may act as an electron trap, thereby inhibiting the recombination rate of electron–hole pairs.

### 3.1.3 Transition metal ions.

Transition metal ions possess multiple valences and unfilled d-electron structures, allowing them to introduce impurity levels within the band gap of $TiO_2$. These impurities serve as shallow traps for photogenerated electrons or holes, effectively reducing the recombination of electron–hole pairs.[83] Transition metal ions, such as Cr, Co, Cu, Fe, and Mn, can be introduced into $TiO_2$ nanotubes by anodization (Fig. 3B) while preserving their ordered tubular structures (Fig. 3C). These ions may occupy interstitial or substitutional positions in the lattice, depending on their respective radii compared to $Ti^{4+}$. For instance, $Fe^{3+}$ (69 pm) and $Cr^{3+}$ (75.5 pm) ions, with smaller radii similar to $Ti^{4+}$ (74.4 pm), are likely to occupy substitutional positions in the lattice of $TiO_2$, while a larger radius like $Co^{2+}$ (79 pm) may occupy interstitial positions. On the other hand, $Cu^{2+}$ (88 pm) and $Mn^{2+}$ (97 pm) ions, with larger radii than $Ti^{4+}$, are also expected to occupy interstitial positions, potentially facilitating the separation of electron–hole pairs. This dual doping mechanism enhances the absorption of visible light, contributing to improved photocatalytic performance.[84] Notably, Group IIIA trivalent metal ions like $Al^{3+}$ (50 pm), $Ga^{3+}$ (60 pm), and $In^{3+}$ (81 pm) possess a radius similar to $Ti^{4+}$, enabling partial substitution within the $TiO_2$ lattice. This substitution leads to doped $TiO_2$ with minimal lattice distortion and no alteration of the crystal structure. In addition, this doping introduces a shallow acceptor level above the valence band in the energy band structure (Fig. 3D), leading to a substantial increase in the carrier concentration of photocatalysts and enhances light quantum efficiency.[85]

The roles of transition metal ions in charge trapping, recombination, interfacial transfer, and photocatalytic activity were systematically studied by doping six types of transition metal ions, including V, Mn, Fe, Cu, Ce, and W, into the surface lattice of $TiO_2$ powders. Among these ions, Fe and Cu were found to enhance interfacial charge transfer by inhibiting defect-mediated annihilation, promoting d–d transitions, and inducing thermally induced de-trapping. Conversely, Mn ions introduced states in the mid-band-gap region, leading to the trapping of charge carriers and significant consumption *via* intra-atomic relaxation. Additionally, Ce and W ions formed strong bonds with $O^{2-}$ radicals, thereby limiting charge utilization and photocatalytic performance.[86] Particularly, Fe metal ions are widely studied for doping into the $TiO_2$ lattice due to their notable effects. However, the efficacy of Fe-doped $TiO_2$ has been hindered by the formation of an amorphous contamination layer, primarily composed of iron oxide, on the nanoparticle surface.[87] The removal of the contamination layer through acid treatment has proven to be effective in enhancing the photocatalytic activity from 24% to 98%.[88]

### 3.1.4 Rare earth ions.

Rare earth elements constitute of a unique group within the periodic table, comprising 17 elements including scandium, yttrium, and the lanthanides from lanthanum to lutetium. Lanthanides are part of the f-block of the periodic table, characterized by the filling of 4f orbitals. The f-orbitals of rare earth ions are relatively low in energy and spatially diffuse, making them available for bonding with Lewis bases. This interaction can result in the formation of stable coordination complexes where the Lewis base molecule or ion acts as a ligand surrounding the rare earth ion. Doping $TiO_2$ with rare earth ions presents a promising strategy for enhancing its photocatalytic performance by introducing unfilled 4f orbitals into the $TiO_2$ lattice. These unfilled orbitals serve as effective electron traps, capturing photoexcited electrons and preventing their recombination with holes. As a result, the lifetime of charge carriers within the $TiO_2$ lattice is extended, leading to improved photocatalytic performance. Moreover, the presence of rare earth elements has been observed to increase the temperature at which the anatase to rutile transformation occurs in $TiO_2$.[89] This higher transformation temperature is beneficial for maintaining the desired anatase phase, which is typically more favorable for photocatalysis.

Doping $TiO_2$ with 1 mol% neodymium results in modified $TiO_2$ with solely the anatase phase, demonstrating superior photocatalytic activity.[91] This enhancement is attributed to the formation of bonds between the rare earth element and $TiO_2$, which not only increases photocatalytic reactivity but also restrains the generation of the rutile phase within the $TiO_2$ structure. The exclusive formation of the anatase phase and the facilitation of bonding interactions with the rare earth element led to improved performance in the modified $TiO_2$ composition. The study of Tb-doped $TiO_2$ photocatalytic activity revealed that the substitution of $Ti^{4+}$ ions with $Tb^{3+}$ ions induce the creation of oxygen vacancies within the $TiO_2$ lattice, due to a large mismatch in ionic radii and charge imbalance.[92] As the $Tb^{3+}$ content increases, the absorption edge of the material shifts gradually towards higher wavelengths. This observed red shift is attributed to charge-transfer transitions between the f electrons of $Tb^{3+}$ ions and either the conduction or valence band of $TiO_2$. The study of different rare earth ions, including $Pr^{3+}$, $Eu^{3+}$, $Er^{3+}$, $Y^{3+}$, $Ho^{3+}$, $Yb^{3+}$, and $Nd^{3+}$, reveals that $TiO_2$ doping with these ions leads to enhanced photocatalytic activity.[93–95] Among these ions, $Ho^{3+}$

stands out for its significant absorption in the visible light region, which can contribute to improved photocatalytic performance under visible light irradiation.[96] This finding highlights the importance of selecting appropriate dopants with favorable electronic structures to maximize the utilization of visible light for photocatalysis.

### 3.2 Non-metal ions

The development of metal-incorporated $TiO_2$ visible light photocatalysts often encounters challenges such as low thermal stability, photo-corrosion, and increased likelihood of serving as recombination centers due to the localized d-states of the dopants deep in the band gap of $TiO_2$.[97,98] To address these drawbacks associated with metal-incorporated photocatalysts, extensive research has focused on modifying $TiO_2$ with non-metal elements to achieve stable visible-light-active $TiO_2$. Non-metal-incorporated $TiO_2$ crystals have shown greater success compared to metal doping because they can introduce mid-gap states acting as electron donors or acceptors within the band gap of $TiO_2$. These mid-gap states effectively reduce the band gap energy and enhance the photoconversion efficiency of $TiO_2$ in the visible light region.

**3.2.1 Boron-doped $TiO_2$.** Doping with boron represents an effective strategy to reduce the band gap of $TiO_2$ by substituting oxygen atoms in the $TiO_2$ lattice with boron atoms, thereby broadening its visible light absorption.[99] Boron incorporation into the $TiO_2$ lattice can occur through three mechanisms: (1) substitutional doping, involves the replacement of oxygen atoms; (2) interstitial doping, which entails the addition of boron atoms; or (3) a combination of both types of doping within the $TiO_2$ lattice. Notably, the stability of interstitially doped B-$TiO_2$ is superior to that of substitutional doping due to the high formation energy of the latter. Substitutionally doped B-$TiO_2$, while metastable, tends to decompose into boron oxide.[100,101]

**3.2.2 Carbon-doped $TiO_2$.** Carbon is a promising dopant for narrowing the band gap of $TiO_2$ by creating a hybrid orbital above the valence level of $TiO_2$, thereby increasing its capacity for visible light absorption.[102–108] Various carbon sources, including carbon nanotubes, graphene, and natural carbon materials, have been reported to enhance the optical and photocatalytic activities of $TiO_2$ matrices. One crucial aspect for enhancing photocatalytic activity lies in controlling the dopant source during the synthesis process. Carbon doping influences the degree of crystallinity, which in turn governs the photocatalytic sites and activity. For instance, hydrothermal synthesis of titanate precursor with different carbon sources (*e.g.*, resorcinol, phloroglucinol, ethylene glycol, and glycerol) was found to alter the phase structure and influence the ratio of anatase to brookite in mixed phase structures of $TiO_2$.[109] These mixed crystal phases exhibited lower band gap energy and reduced photogenerated electron–hole recombination rates. In another example, C-doped $TiO_2$ catalysts prepared *via* a sol–gel method from titanate precursor and glucose show enhanced anatase to rutile phase transformation due to carbon doping from the glucose source.[110] This occurs through the formation of Ti–O–C bonds, which are positioned within the interstitial locations of the $TiO_2$ lattice at the interfaces of the anatase $TiO_2$ domains. Successful anatase crystallization suppresses the electron–hole recombination rate by reducing the number of defects, thereby improving photocatalytic activity.

In many cases, doping techniques are utilized to enhance visible light absorption in photocatalytic materials, but they often result in the formation of defect sites, which can compromise photocatalytic activity. One strategy to mitigate the probability of charge recombination is to encapsulate C-doped $TiO_2$ particles with nano-sized graphene.[111] This approach aims to facilitate the effective transfer of photogenerated electrons to surface active sites by reducing the interfacial charge-transfer resistance between C-doped $TiO_2$ and reactants. As a result, the prolonged lifetime of photogenerated charges over the C-doped $TiO_2$ nanoparticles enables the generation of a large number of hydroxyl radicals with high oxidizing power for photodegradation purposes.

Another approach to modifying $TiO_2$ with carbon involves the formation of core–shell nanostructure photocatalysts. In this method, carbon-modified $TiO_2$ core–shell nanostructures were fabricated using an acidified sol–gel system with titanium-*n*-butoxide and a regenerated cellulose membrane.[104] This approach has been shown to enhance the visible light photocatalytic performance. The synergistic effect of the carbon shell and $TiO_2$ promotes the formation of a large number of hydroxyl radicals due to the carbon's photosensitizer behavior, thus supporting higher photocatalytic activity. The enhanced visible light absorption capability is primarily attributed to the incorporation of carbon dopants at interstitial positions in the $TiO_2$ lattice, forming O–Ti–C or Ti–O–C bonds. In addition, the formation of the carbon core–shell nanostructure occurs through a carbonaceous layer grafted onto the surface of $TiO_2$ *via* Ti–O–C and Ti–OCO bonds. In this study, the calcination temperature is identified as an important parameter for controlling the thickness of the carbon shell coating on $TiO_2$, as well as its crystallinity, surface area, and optical properties. Specifically, increasing the calcination temperature from 75 to 500 °C results in a narrowing of the band gap from 2.95 to 2.80 eV, and an increase in the thickness of the carbon shell from 0.40 to 1.20 nm, respectively. However, excessive carbon thickness is found to be detrimental to photocatalysis because it can shield the passage of light and hinder reactant adsorption on the $TiO_2$ surface.

**3.2.3 Nitrogen-doped $TiO_2$.** Among non-metal dopants, nitrogen emerges as a highly promising candidate for altering the band gap of $TiO_2$ due to its intrinsic properties, including comparable atomic size to oxygen, small ionization energy, and stability.[112–114] The doping of nitrogen in $TiO_2$ leads to the mixing of N 2p with O 2p states, resulting in a narrower band gap compared to pure $TiO_2$ by shifting the edge of the valence band upward. Several techniques and methodologies have been developed to incorporate nitrogen into $TiO_2$, including direct nitridization,[115] sol–gel,[116] electrochemical methods,[117] hydrothermal,[118] and solvothermal reactions,[119] sputtering,[120] and ball milling with nitrogenous compounds.[121] In principle, oxygen-rich conditions, such as those employed in wet processes like sol–gel methods, induce the formation of nitrogen atoms in interstitial positions of the $TiO_2$ lattice. In contrast, oxygen-deficient (reducing) conditions favor the incorporation of nitrogen atoms in oxygen lattice sites, resulting in substitutional doping.[120,122] Substitutional doping reduces the band gap of $TiO_2$ to approximately 3.06 eV, while interstitial doping can further narrow it to ~2.46 eV. The presence of nitrogen promotes a red-shift in absorption spectra and lowers the energy formation of oxygen vacancies, consequently enhancing photocatalytic activity through efficient electron trapping and electron–hole separation.[123,124] The correlation between oxygen vacancies and photocatalytic properties depends on the concentration of nitrogen doping. At low nitrogen concentrations, interstitial doping dominates, promoting oxygen vacancies. Conversely, high levels of nitrogen incorporation encourage substitutional doping, which reduces the concentration of oxygen vacancies. For highly doped anatase, a cubic titanium oxynitride phase was discovered which offers valuable insights into the fundamental shift in absorption wavelength. This shift enables excellent photocatalytic performance using visible light, signifying a significant advancement in the field.[125]

**3.2.4 Phosphorus-doped $TiO_2$.** The doping of phosphorus into $TiO_2$ lattices results in absorption in the visible light region due to the impurity energy level in the band gap, typically in the form of $P^{5+}$ ions. Chemically, it is more favorable to incorporate $P^{5+}$ ions into the $TiO_2$ lattice by substituting $Ti^{4+}$ ions to form Ti–O–P bonds, rather than incorporating $P^{3+}$ ions by substituting $O^{2-}$ ions to form Ti–P bonds.[90] This preference is ascribed to the significantly larger formation energy required for phosphorus substituting oxygen in $TiO_2$ (15.48 eV) compared to phosphorus substituting titanium (1.32 eV).[126]

Early studies on phosphorus-modified $TiO_2$ primarily focused on improving thermal stability and surface area.[127,128] Surface modification of $TiO_2$ with phosphoric acid is a common technique for preparing P-doped $TiO_2$ photocatalysts. Phosphate anions from phosphoric acid adsorb strongly on the surface of $TiO_2$, significantly influencing the interfacial and surface chemistry of $TiO_2$.[129] The incorporation of phosphorus into the $TiO_2$ lattice using phosphoric acid as the phosphorus source *via* a sol–gel method resulted in a redshift in the absorption edge due to the formation of Ti–O–P bonds in the crystal lattice.[130] Furthermore, phosphorus doping affects the crystallization of $TiO_2$ by inhibiting crystal growth and suppressing the phase transformation from anatase to rutile. Apart from these observed merits, the enhanced visible light activity is primarily attributed to increased hole signal intensity, indicating efficient trapping of photogenerated holes.

Apart from post-treating $TiO_2$ with phosphoric acid, other methods of introducing phosphorus into $TiO_2$ include using elemental red phosphorus *via* a ball milling process[131] or decomposing black phosphorus *via* high-intensity ultrasonication.[90] In the case of black phosphorus, it can absorb onto the $TiO_2$ surface through electrostatic interactions, leading to the formation of uniformly dispersed P–$TiO_2$ composites. These P–$TiO_2$ composites can then be blended with a polyacrylic matrix to prepare functional coatings with photocatalytic properties (Fig. 3E). During the decomposition process of black phosphorus, $P^{5+}$ ions are produced and incorporated into the crystal lattice of $TiO_2$ to form P–O–Ti bonds. This incorporation leads to the generation of more defects in the P–$TiO_2$ crystals, which helps trap electrons and suppress the recombination of electron–hole pairs. Consequently, the photocatalytic ability of P–$TiO_2$ is expected to be superior to both $TiO_2$ and black phosphorus.

**3.2.5 Sulfur-doped $TiO_2$.** The modification of $TiO_2$ with sulfur doping results in band-gap narrowing by introducing localized states within the band gap structure of $TiO_2$.[132] However, incorporating sulfur into $TiO_2$ poses challenges due to the larger ionic radius of sulfide ions ($S^{2-}$, 1.84 Å) compared to oxide ions ($O^{2-}$, 1.22 Å). This discrepancy in size leads to a higher formation energy for the substitution of sulfur to form Ti–S bonding compared to Ti–O bonding. In principle, sulfur doping in $TiO_2$ can occur through various mechanisms, including the substitution of $Ti^{4+}$ (0.65 Å) by $S^{6+}$ and/or $S^{4+}$ (~0.51 Å), or the direct incorporation of $S^{2-}$ into the $TiO_2$ lattice. The substitution of $Ti^{4+}$ by $S^{6+}$ or $S^{4+}$ ions is more chemically favorable due to their smaller ionic radii compared to $S^{2-}$ ions.[133] In another words, the sulfur dopant can act as both cationic and anionic substitution in $TiO_2$ ($S^{6+}$, $S^{4+}$, $S^{2-}$).

The early studies on sulfur doping of $TiO_2$ have shown that the band gap modification is achieved by substituting lattice oxygen with $S^{2-}$ ions to form Ti–S bonds, representing anionic substitution.[133] In this work, S-doped $TiO_2$ was synthesized through the oxidative annealing of titanium disulfide. This doping of sulfur induces a significant shift in the absorption edge towards lower energy by mixing the S 3p states with the VB.[134] The use of titanium disulfide as starting material was later extended in hydrothermal oxidation reaction to prepare anionic S-doped $TiO_2$.[134] Subsequent to thermal annealing, various chemical processes have been developed for synthesizing S-doped $TiO_2$, including ball milling,[135] sol gel,[136] flame spray pyrolysis,[137] oxidant peroxide method,[138] hydrothermal reaction,[134] and solvothermal reactions.[139] The choice of preparation method and sulfur sources significantly influences the ionic form of sulfur doping in $TiO_2$. Studies have shown that thiourea and carbon disulfide as sulfur sources favor the formation of anionic sulfur doping in the $TiO_2$ crystal lattice. When $TiS_2$ or $CS_2$ is used, most of the sulfur from $TiS_2$ or $CS_2$ is oxidized, leaving residual S as $S^{2-}$, which replaces oxygen atoms in the O–Ti–O framework. Conversely, using thiourea as the sulfur source promotes the cationic doping of S atoms into the $TiO_2$ crystal lattice.[138,140]

**3.2.6 Fluorine-doped $TiO_2$.** Fluorine has been utilized in multiple capacities to enhance the photocatalytic performance of $TiO_2$. It has been utilized as a capping agent and/or dopant in $TiO_2$ to modify both their surface and bulk properties. This modification leads to increased specific surface area, creation of surface oxygen vacancies, enhanced visible light absorption, and slower charge recombination.[141–144] The induced oxygen vacancies, associated with the formation of $Ti^{3+}$ species, contribute to improved electronic conductivity and appear at energy levels 0.3 to 0.8 eV below the conduction band minimum of $TiO_2$.[141,145] In addition, fluorine has been employed as a structure-directing agent, facilitating the generation of $TiO_2$ with exposed high-energy (0 0 1) facets, which exhibit superior photocatalytic activity compared to other facets.[23,146,147] Despite the dominance of the (101) facet, efforts have been made to selectively modify $TiO_2$ during synthesis to favor the growth of the less thermodynamically favored (001) facet.[148] Fluorine ions are particularly notable for their role in controlling the growth of $TiO_2$ facets.[149,150]

To attain optimal photocatalytic performance, numerous studies on F-doped $TiO_2$ have focused on controlling fluorine doping concentration during synthesis. For instance, in a hydrothermal synthesis of F-doped rutile single crystalline $TiO_2$, the optical band gap of the photocatalyst was effectively adjusted from 3.05 to 2.58 eV by varying the fluorine doping concentration.[141] Besides, the concentration of fluorine doping has been identified as a crucial factor in shaping the morphology of $TiO_2$. Using $TiCl_4$ as a precursor, a range of $TiO_2$ hierarchical nanostructures, including pompon-like and football-like microspheres composed of aligned rutile and anatase nanoparticles, have been synthesized using a hydrothermal method in the presence of NaF.[151] An incremental increase in the concentration of NaF leads to a sequential red shift of the absorption band edge of F-doped $TiO_2$ compared to pure $TiO_2$. Consequently, the band gap of F-doped $TiO_2$ can be tuned from 3.0 eV to 2.2 eV, with the degree of tuning dependent on the fluorine doping concentration.

## 4 Noble metals-supported $TiO_2$ hybrids

The integration of noble metals onto the surface of $TiO_2$ introduces new functionalities by leveraging the intrinsic properties of metal nanoparticles, significantly enhancing their performance as photocatalysts. Noble metal nanoparticles, such as silver (Ag) and gold (Au), exhibit strong absorption across the UV to near-infrared (NIR) spectrum due to their surface plasmon resonance, which can be tailored by controlling their size, shape, and surrounding medium.[29] Despite Ag's susceptibility to oxidation, it remains a top candidate for plasmonic applications due to its low optical loss in the visible and NIR spectral regions. On the other hand, Au offers superior stability alongside excellent performance in the visible and NIR ranges. While aluminium and copper are alternative plasmonic materials, their poor chemical stability limits their applicability. Palladium (Pd) and platinum (Pt) are catalytically active metals, but both do not support strong plasmonic resonances at visible wavelengths. In hybrid systems formed by depositing noble metals onto $TiO_2$, these metal nanoparticles serve as antennae, efficiently absorbing visible light and generating energetic electrons and holes in the semiconductor.[152,153] This synergistic effect between $TiO_2$ and noble metals enhances photoreactivity across a broad range of the solar spectrum, overcoming the inherent limitations of wide band gap $TiO_2$ semiconductors.

In contrast to conventional semiconductor photocatalysis, plasmonic photocatalysis exhibits two distinct features: the Schottky junction and localized surface plasmon resonance (LSPR).[154] In semiconductor-noble metal hybrid systems, when illuminated with UV light, the excited electrons of the semiconductor are transferred from the CB to the Fermi level of noble metals, leading to the separation of electron–hole pairs. This metal–semiconductor interface, known as the Schottky junction, promotes charge separation and transfer at the interface. Meanwhile, LSPR plays a crucial role in plasmonic photocatalysis by inducing the collective oscillation of conduction electrons at the interface of metallic structures upon excitation by incident electromagnetic radiation of the same frequency. When noble metals absorb visible light through LSPR, charge carriers in the noble metals are directly injected from excited plasmonic metal nanostructures into the semiconductor, contributing to strong visible light absorption and the generation of active charge carriers.[155] Both the Schottky junction and LSPR significantly enhance the photocatalysis process and the overall photocatalytic efficiency of $TiO_2$ semiconductor (Table 3).

### 4.1 Ag on $TiO_2$

Functionalizing Ag nanoparticles presents challenges related to stability, aggregation, and size control, compounded by their susceptibility to oxidation over time, which can degrade their surface properties. However, the work of Awazu *et al.* represents a significant advancement in plasmonic photocatalysis by combining $TiO_2$ with optically active Ag nanoparticles.[156] In this approach, the excitation of surface plasmons on the Ag nanoparticle surface amplifies the near-field amplitude at specific wavelengths in the near UV region, leading to higher concentrations of charge carriers in $TiO_2$ and thereby increasing the efficiency of photocatalysis. The important feature to enable plasmonic photocatalysis in this study is to deposit $TiO_2$ on Ag nanoparticles coated with thin protective $SiO_2$ shell to prevent oxidation. This protective shell ensures that the photodegradation rate by the $TiO_2$ photocatalyst modified with protected Ag nanoparticles is 7 times faster than that of pure $TiO_2$ under UV irradiation. Alternatively, a polymer shell can be used to protect Ag nanoparticles from oxidation, forming a core–shell structure with an Ag core and a polymer shell. For instance, polyacrylic acid is employed for polymer encapsulation on the Ag nanoparticles using Layer-by-Layer synthesis, enabling precise control of the polymer shell thickness at the nanoscale without compromising the plasmon-induced enhancement of the near-field.[157] The $TiO_2$ photocatalyst modified with protected Ag core–shell structures demonstrates a 15% enhancement in their photocatalytic activity in air compared to pure $TiO_2$. Notably, this enhanced activity is retained over time, even upon aging in air, whereas $TiO_2$ modified with bare Ag nanoparticles loses its plasmonic properties gradually.

This phenomenon can be attributed to the progressive oxidation of the unprotected Ag nanoparticles to $Ag_2O$ at the surface, causing the detrimental loss of their plasmonic properties.

The performance of the plasmonic photocatalyst $Ag/TiO_2$ is a strong function of the size and shape of Ag nanostructures.[158] Tailoring the size and shape of Ag nanostructures enables the control of the properties of Ag surface plasmons, in turn tuning their impact on the photocatalytic activity of $TiO_2$. The enhanced photochemical activity of $Ag/TiO_2$ composite systems is largely dependent on the plasmon-mediated transfer of energy from Ag nanoparticles to $TiO_2$ to increase the concentration of electron–hole pairs in the composite. In this case, the Ag nanocubes exhibit superior amplifications in the photochemical reactivity relative to that of the Ag nanospheres and nanowires of similar size for identical Ag mass (volume). The enhancement reactivity of nanocubes can be explained by their large extinction cross-section, more specifically, a higher scattering efficiency.

### 4.2 Au on $TiO_2$

The photocatalytic activity of $Au/TiO_2$ is influenced by various factors including the Au loading, phase composition, particle size, shape, surface area, and spatial structuring.[24,159–161] Studies have shown that smaller Au nanoparticles tend to favor enhanced photocatalytic performance.[162–165] This size effect is attributed to the shift of the Fermi energy to a more negative potential for smaller nanoparticles, reducing the potential difference between the CB of $TiO_2$ and the Fermi level of the metal nanoparticles. As a result, electron accumulation in the metal nanoparticles increases, leading to an upward shift of the Fermi level to the CB of $TiO_2$, promoting rapid electron transfer from $TiO_2$ to metal nanoparticles for improved photooxidation reactions by photoexcited holes. Conversely, chemically aggregated nanospheres or nanorods may not be as beneficial to the photocatalytic activity of $TiO_2$ due to differences in their co-catalytic efficiency, influenced by factors such as the percentage of surface-active atoms and Fermi energy shifts resulting from changes in size, shape, and surface-to-volume ratio. Nanorods, for instance, might reduce substrate adsorption and block light penetration on the oxide surface, leading to lower photogeneration of charged species and reduced photoactivity. To control the dispersibility of the co-catalyst nanoparticles, Tatsuma *et al.* prepared $Au/TiO_2$ composites using the electron trap-mediated deposition method, leveraging the electron traps present in $TiO_2$.[166] This method offered higher dispersibility of the Au co-catalyst compared to the photodeposition method whereby the amount of deposited Au could be controlled and preventing overloading.

Numerous studies have demonstrated that plasmonic metals, when integrated with $TiO_2$ semiconductor in structurally optimized configurations, can significantly boost light absorption.[167,168] Li *et al.* developed spinous $TiO_2$-based octahedral nanocages through a template-assisted approach, resulting in enhanced photocatalytic performance compared to spinousless nanocages.[169] Zhao *et al.* designed an oxygen vacancy-rich 2D $Au/TiO_2$ hybrid nanosheet derived from 2D Mxene, achieved *via in situ* growth of Au nanoparticles on preformed $TiO_2$ nanosheets.[170] The synergistic interplay between Au active species and abundant oxygen vacancies from $TiO_2$ significantly lowered the reaction barrier and improved catalytic reactions. Guo *et al.* fabricated a hierarchical forest-like plasmonic superstructure consisting of vertically printed macro-sized $TiO_2$ pillar arrays as tree trunks, dense $TiO_2$ nanorod arrays as branches, and self-assembled Au nanoparticles as leaves. This plasmonic superstructure effectively absorbs light through surface plasmon resonance effects and multiple scattering, offering high light absorption capacity and interconnect mass transfer channels (Fig. 4).

### 4.3 Multimetals on $TiO_2$

Noble metals like Ag, Au, Pt, and Pd serve as potent co-catalysts in $TiO_2$, offering numerous benefits to the photocatalytic process. They essentially act as electron traps, assisting in the separation and transfer of charges on the semiconductor surface. This facilitates the creation and movement of electron–hole pairs, thereby improving catalytic reactions.

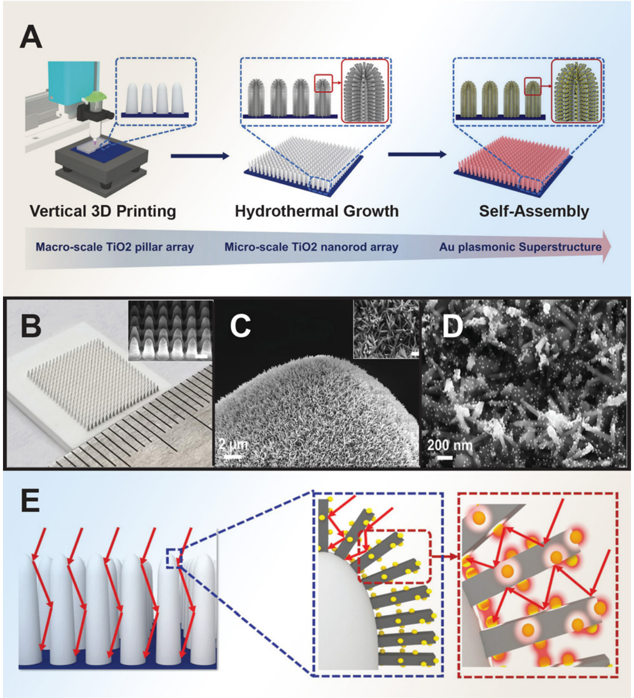

**Fig. 4** Fabrication of forest-inspired hierarchical Au plasmonic superstructure. (A) Printing of $TiO_2$ pillar arrays and hydrothermal grown layer of dense $TiO_2$ nanorod arrays, followed by self-assembling Au nanoparticles on the hierarchical $TiO_2$ structure. (B) Optical image of a printed $TiO_2$ pillar array. (C) Scanning electron microscopy (SEM) images of the $TiO_2$ nanorods growing on the top surface of a 3D printed $TiO_2$ pillar. (D) SEM image of Au nanoparticles assembled on $TiO_2$ nanorods. (E) Schematic illustration of the light-trapping approaches of Au plasmonic superstructure through the multiple light scattering of the vertically aligned pillars and nanorods in multiscale and LSPR effects of Au nanoparticles. Reproduced with permission from ref. 185. Copyright 2021, Wiley-VCH.

Furthermore, they contribute to modifying the energy levels and band structures of $TiO_2$, broadening its light absorption spectrum to include visible light, and ultimately enhancing its overall photocatalytic performance.[13,171,172] On the other hand, multi-metallic nanoparticles of noble metals represent a novel class of nanomaterials with distinct properties compared to monometallic nanoparticles.[173–176] They offer enhanced versatility and technological utility due to their unique properties and the ability to tune their LSPR properties through configurational and elemental modifications.[176–178] These multi-metallic nanoparticles exhibit multi-functionality, wide tunability, and multiple plasmon bands, making them ideal components for $TiO_2$ photocatalysts.[179,180] Bimetallic combinations like Au–Ag,[181,182] Au–Pd,[183] and Au–Pt[184] loaded onto $TiO_2$ have demonstrated efficient photocatalytic activity, due to their ability to efficiently separate electron–hole pairs at the alloy/$TiO_2$ junction. Moreover, controlling the morphology and structure of plasmonic nanoparticles supported on $TiO_2$ can significantly influence product selectivity in photocatalytic reactions.

Studies on visible-light-responsive Au–Ag alloy nanoparticles loaded onto $TiO_2$ have demonstrated successful control over the apparent photocatalytic activity by altering the alloy composition. The photocatalytic reactions were found to be based on plasmon-induced charge separation.[179,186] For instance, colloidal suspensions of $Au_xAg_{1-x}$ alloys with composition $x$ ranging from 0.2 to 1 exhibit an intense SPR band in the broad visible light range of 420 to 520 nm. When $Au_{0.3}Ag_{0.7}$ alloy nanoparticles are deposited on $TiO_2$, this plasmonic photocatalyst generates SPR at 490 nm, corresponding to the maximum intensity of solar light.[179] The $TiO_2$ photocatalyst containing 1% of each metal (Ag, Au, Pt, Pd) in an alloy structure exhibited a remarkable increase in photoactivity compared to monometallic nanoparticles.

## 5 Defective $TiO_2$ nanomaterials

Defect engineering in $TiO_2$ involves intentionally introducing imperfections or vacancies into the crystal lattice to tailor its properties for specific applications. The prevalence of these defects has been extensively investigated through theoretical calculations and experimental analyses due to its ability to modify the electronic structure, charge carrier dynamics, and surface reactivity of $TiO_2$.[55,187] Oxygen vacancies and $Ti^{3+}$ interstitials are two commonly studied defects in $TiO_2$, which are known to influence the electronic properties of $TiO_2$ by generating intermediate bands, hence reducing its band gap.[188,189] Moreover, oxygen vacancies can enhance the donor density and facilitate the separation and mobility of photogenerated electron–hole pairs.[190] By strategically controlling the types and concentrations of defects, defect engineering enables the development of $TiO_2$-based materials with enhanced performance.

Oxygen vacancies are introduced into the $TiO_2$ lattice through various methods, including annealing in an oxygen-deficient atmosphere or as a byproduct of doping processes involving anions or cations.[125,191] These vacancies can create intermediate energy states within the band gap of $TiO_2$, effectively extending its light absorption into the NIR region. As a result, $TiO_2$ materials with oxygen vacancies exhibit enhanced photoactivity, particularly under visible light irradiation. Black $TiO_2$, rich in oxygen vacancies, has been shown to significantly improve the photocatalytic performance compared to white (stoichiometric) $TiO_2$. Additionally, colored $TiO_2$ materials such as blue or gray variants can be obtained through hydrogenation, resulting in sub-stoichiometric oxide. These sub-stoichiometric oxides possess altered chemical compositions and structures, characterized by features like surface disordered shells, oxygen vacancies, $Ti^{3+}$ centers, and surface hydroxyl groups or Ti–H bonds.[188]

In 2011, Chen *et al.* introduced black $TiO_2$ with a narrowed band gap of 1.5 eV to enhance full spectrum sunlight absorption by subjecting $TiO_2$ nanoparticles to hydrogen thermal treatment.[25] This process induced disorder layers on the $TiO_2$ surface, resulting in the formation of defective black $TiO_{2-x}$ nanoparticles and giving rise to an increase in photocatalytic activity. Following this, Hu *et al.* developed black $TiO_2$ hollow spheres with a narrow bandgap using a template-free solvothermal approach.[192] The $TiO_2$ hollow frameworks, stabilized by encircled protectors like amine molecules, maintained high structural integrity and improved crystallinity of the anatase phase during high-temperature hydrogenation. The thermal hydrogenation process created a disordered shell layer over the crystalline $TiO_2$ core, with dispersed $Ti^{3+}$ within the hollow structure frameworks. The resulting mesoporous black $TiO_2$ hollow spheres exhibited a high photo-response in visible-light absorption and significantly improved photocatalytic activity, attributed to their high crystallinity, hollow structure, $Ti^{3+}$ content in the frameworks, and surface disorderliness.

To date, various synthetic techniques beyond hydrogenation have been explored to synthesize black $TiO_2$ with broad spectrum absorption. These methods include metal reduction, plasma-assisted processes, $NaBH_4$ reduction, electrochemical reduction, laser ablation in liquid, and oxidation approaches.[193] In the case of black $TiO_2$ hollow spheres synthesized *via* aluminum reduction, the formation of oxygen vacancy defects generates mid-gap states, facilitating electron excitation at lower energies.[194] This electron transition from the valence band to the oxygen vacancy mid-levels, or *vice versa*, enables absorption of visible and infrared light. However, despite these optical enhancements, photogenerated electrons residing at the energy levels of oxygen vacancies are unable to participate in hydrogen production ($H^+ \rightarrow H_2$) as their energy levels are situated below the reduction potential of $H_2O/H_2$. Consequently, this absence of photocatalytic activity under visible light illumination highlights a limitation in utilizing these oxygen vacancies for hydrogen production.

Sub-stoichiometric titania ($TiO_{2-x}$), also known as colored titania (gray, blue, brown, or black), exhibits efficient light absorption across the UV to the IR region of the solar spectrum. Numerous studies have highlighted its enhanced photoactivity in various oxidation reactions under visible light compared to ordinary white (stoichiometric) $TiO_2$.[188,195] The synthesis of these materials typically involves thermal treatment of $TiO_2$ in different reducing atmospheres, including vacuum, Ar, $H_2$/Ar, and pure $H_2$.[196] Generally, increasing the reduction level results in a higher defect density, such as oxygen vacancies and $Ti^{3+}$ centers, within the $TiO_2$ lattice, leading to darker-colored $TiO_2$ powder.

## 6 Composites of $TiO_2$ nanomaterials

Composite photocatalysts have emerged as promising materials for overcoming the intrinsic limitations of individual semiconductor photocatalysts. The tailored properties of composite photocatalysts play an essential role in maximizing their photocatalytic performance by improving light absorption, charge separation, redox capability, and chemical reactivity.[197,198] For instance, the inclusion of carbon-based materials such as graphene or carbon nanotubes in $TiO_2$-based nanocomposites has been particularly effective. When combining $TiO_2$ with graphene, excited electrons from the conduction band of $TiO_2$ can transfer to graphene through a percolation mechanism. This transfer results in the formation of a heterojunction at the interface which effectively separates the photoinduced electron–hole pairs, thereby suppressing charge recombination.[199] Hybridization with carbon quantum dots results in the formation of new electronic structures and an increase in the photo-response.[200] Combining $TiO_2$ with various materials such as carbon nitride, metal–organic frameworks, Mxene, and aerogels can lead to the development of advanced composite photocatalysts with enhanced properties and functionalities.

### 6.1 $TiO_2$/$C_3N_4$

Carbon nitride (g-$C_3N_4$) is a 2D polymer composed of carbon and nitrogen atoms arranged in a graphitic structure. Due to its polymeric nature, the surface chemistry of g-$C_3N_4$ can be readily modulated through surface engineering at the molecular level.[201] In comparison with $TiO_2$, g-$C_3N_4$ has a moderate band gap ranging from 2.7 to 2.8 eV, allowing it to absorb visible light with an onset around 450 to 460 nm.[202] Since the metal-free semiconductor was reported to generate hydrogen from water by Wang *et al.* under visible-light irradiation,[203] g-$C_3N_4$ has been widely employed as a guest semiconductor to modify $TiO_2$. The favorable alignment of band positions between g-$C_3N_4$ and $TiO_2$ confers a greater driving force for charge transfer across the heterointerface in constructed $TiO_2$/g-$C_3N_4$ heterostructures. This alignment promotes spatial separation of photogenerated electron–hole pairs, consequently enhancing the overall photoconversion efficiency of the system.[204–206]

### 6.2 $TiO_2$/MXene

Titanium carbide ($Ti_3C_2$, a member of the 'MXene' family) has emerged as a new class of promising 2D materials because of their unique properties including high conductivity, high structural, chemical stability, and tailored surface chemistry.[207,208] Moreover, $Ti_3C_2$ has a large proportion of Ti, which can be readily transformed into $TiO_2$.[209] The Schottky junction formed at the interface between $Ti_3C_2$ and $TiO_2$ could promote the photoinduced charge separation. By a hydrothermal oxidation of layered $Ti_3C_2$, the Ti atoms on $Ti_3C_2$ afforded the Ti source and nucleating sites for the *in situ* growth of highly active (001) facets $TiO_2$ nanosheets on $Ti_3C_2$, and it also forms an interfacial heterojunction between 2D $Ti_3C_2$ and $TiO_2$ to prevent the defect-induced recombination. This is related to the large gap in work function of the two phases between –OH terminated $Ti_3C_2$ (1.8 eV) and $TiO_2$ (001) surface (4.924 eV), thus hindering the electron transfer from $TiO_2$ to $Ti_3C_2$, instead allowing the flow of photogenerated holes. As such, the low function –OH terminated $Ti_3C_2$ serves as a reservoir of holes through the hole trapping by the Schottky-junction, yielding the spatial separation of photogenerated electrons and holes.[198,210]

### 6.3 $TiO_2$/MOF

Metal organic frameworks (MOFs) are a new generation of organic-inorganic hybrid porous materials, making up by metal ions/clusters connected by organic ligands. These structures provide a large surface area and tunable pore sizes, making them excellent candidates for hosting catalytic metal clusters within their frameworks. The metal clusters can function as active sites for catalytic reactions. $TiO_2$ can be synergistically coupled with the catalytic properties of metal clusters within the MOFs structure. This synergy allows for efficient utilization of photoexcited electrons generated by $TiO_2$ in driving catalytic reactions facilitated by the metal clusters. By adjusting parameters such as pore size, surface area, and $TiO_2$ loading, the photocatalytic activity and selectivity of the composite material can be optimized for specific catalytic applications. To give an illustration, combining $TiO_2$ nanosheets with exposed (001) facets and $NH_2$-UiO-66 (MOF) *via* an *in situ* growth strategy offers a promising approach for producing bifunctional materials capable of both capturing and photocatalytically reducing cardon dioxide ($CO_2$) under UV-vis light irradiation. This strategy leverages the strengths of $TiO_2$ nanosheets and $NH_2$-UiO-66 MOF while allowing intimate contact between the two components, with the formation of a heterojunction for effective charge transfer.[211] Photogenerated electrons from $TiO_2$ can readily transfer to the catalytic sites within MOFs, facilitating gaseous adsorption and subsequent catalytic reactions.

### 6.4 $TiO_2$/COF

Covalent organic frameworks (COFs) are a novel class of crystalline organic polymers constructed from light elements such as carbon, hydrogen, nitrogen, oxygen, and sulfur.[212–214] These frameworks are linked *via* strong covalent bonds, which bestow them with remarkable stability and robustness. COFs are characterized by unique properties including low density, large surface area, tunable pore size and structure, and easily customizable functionality.[215–217] Despite these advantages, the photocatalytic performance of pure COFs is limited by high recombination rates of photoinduced electron–hole pairs. To address this limitation, COFs are often integrated with $TiO_2$ to form composites. $TiO_2$, with its band gap of approximately 3.2 eV, is highly effective in visible light-assisted photocatalysis, making it an ideal candidate for integration with COFs.[218–220] This combination aids in the formation of heterostructures, significantly enhancing the photocatalytic functionality. $TiO_2$/COF composites utilize COFs as efficient photosensors, improving light absorption and overall applicability. The formation of heterojunctions and band gap narrowing in $TiO_2$/COF composites optimizes the interaction between $TiO_2$ and COFs, which have a band gap between 2 and 2.8 eV. This optimization reduces the recombination rate of photoinduced electron–hole pairs, thereby enhancing the production of active species and overall photocatalytic activity.[21,221]

### 6.5 $TiO_2$/aerogel

Aerogels are a fascinating class of highly porous materials composed of a network of interconnected nanostructures which exhibit high surface areas, open pores, low densities, and unique physical properties.[222,223] Aerogel can be prepared using sol–gel process followed by supercritical drying, allowing for the production of aerogel in various shapes and sizes that suitable for different applications.[224,225] Particularly, $TiO_2$ aerogels consisting of a network of interconnected $TiO_2$ nanoparticles have emerged as a highly favorable architecture, offering ample active sites for photocatalytic reactions and long diffusion pathways for photogenerated electrons. Additionally, $TiO_2$ aerogels have been observed to possess surface trap states where large amounts of photogenerated electrons can be stored upon illumination, which enhances their photocatalytic activity by promoting efficient charge separation and utilization in redox reactions. It was reported that the as-synthesized aerogel can store 1.7 times more electrons relative to commercial anatase nanoparticles.[226]

### 6.6 $TiO_2$/other semiconductor composites

Heterojunction photocatalysts are engineered by combining two distinct semiconductor materials. This coupling takes advantage of the unique electronic properties of each semiconductor, creating an interface where efficient charge separation can occur. When these heterojunctions are exposed to light, they generate electron–hole pairs in both semiconductor components.[227–229] The type-II heterojunction, one of the most studied types, features staggered band structures where electrons accumulate in one semiconductor (photocatalyst II) and holes in the other (photocatalyst I), promoting efficient charge separation for photocatalysis.[38,230,231] While the type-II heterojunction configuration enhances charge separation, it also reduces redox ability, which is not ideal for photocatalysis.

Traditional Z-scheme photocatalysts, proposed to address the limitations of type-II heterojunctions, improve charge-separation efficiency while maintaining strong redox abilities.[36] This system consists of two semiconductors with suitable intermediate couples, such as $Fe^{3+}/Fe^{2+}$, $IO^{3-}/I^{-}$, and $I^{3-}/I^{-}$, arranged in staggered band structures.[232] In operation, photogenerated holes in the VB of photocatalyst I react with electron donors (D), creating electron acceptors (A). Simultaneously, photogenerated electrons in the CB of photocatalyst II react with A, forming D. The retained electrons in the CB of photocatalyst I and holes in the VB of photocatalyst II are then available for reduction and oxidation reactions, respectively.[233] This charge-transfer mode endows the system with strong redox ability and spatially separated redox reaction sites, enhancing photocatalytic performance by facilitating more efficient and selective redox reactions. However, this system is limited to the solution phase, faces side reactions, light shielding issues, and pH sensitivity.[234]

The all-solid-state Z-scheme was introduced to overcome the limitations of traditional Z-scheme photocatalysts by replacing shuttle redox ion pairs with a solid conductor. In a three-component heterojunction (CdS–Au–$TiO_2$), both the holes in CdS and electrons in $TiO_2$ are injected into Au.[43] This scheme utilizes a solid conductor instead of shuttle redox ion pairs, making it suitable for both liquid and gas applications and significantly shortening the charge-transfer length, thus accelerating charge transfer.[235] In a typical all-solid-state Z-scheme, the CB electrons of photocatalyst II migrate to a solid conductor upon light irradiation and then to the VB of photocatalyst I. This innovation allows for applications in both liquid and gas phases and accelerates charge transfer, significantly enhancing the efficiency of the photocatalytic process. Despite these advancements, it faces challenges such as Schottky barriers, preferential electron transfer leading to neutralization at the conductor, and difficulties in synthesis and assembly.

Direct Z-scheme heterojunctions, evolving from traditional and all-solid-state Z-scheme heterojunctions, refine the concept by eliminating intermediate redox couples or conductors.[236,237] Instead, they couple an oxidative and a reductive photocatalyst based on their VB and CB positions. This setup optimizes charge transfer and enhances photocatalytic activity by ensuring that electrons from the low VB photocatalyst are injected into the VB of the high CB photocatalyst.[47,238] $TiO_2$, known for its low VB position, is frequently used as an oxidative photocatalyst and is often coupled with high CB photocatalysts such as CdS,[237] $ZnIn_2S_4$,[239] and $Cu_2O$.[240,241] In this scheme, electrons excited to the CB of the low VB photocatalyst are injected into the VB of the high CB photocatalyst, optimizing charge transfer and enhancing photocatalytic activity.

Despite their advantages, Z-scheme heterojunctions face confusion and theoretical challenges. The S-scheme heterojunction, a recent advancement, addresses the limitations of Z-scheme heterojunctions by improving charge separation and maintaining strong redox abilities.[51,234] It comprises an oxidation photocatalyst (OP) and a reduction photocatalyst (RP), where the RP has more negative CB and Fermi levels, and the OP has more positive VB. Electron transfer from the RP to the OP due to Fermi level differences generates an internal electric field and band bending, enhancing photo-induced carrier transfer. Under illumination, electrons in the OP's CB migrate to the RP's VB and combine with holes, differing from the type-II mechanism. This carrier transfer resembles a "step" at a macroscopic level and an "N" shape at a microscopic level, optimizing photocatalytic performance.[242] A recent study reveals that the $TiO_2$/perovskite ($CsPbBr_3$) S-scheme heterojunction demonstrates electron transfer from $CsPbBr_3$ quantum dots to $TiO_2$, resulting in an internal electric field directed from $CsPbBr_3$ to $TiO_2$ upon hybridization.[243] Upon light irradiation, this internal electric field drives the photoexcited electrons in $TiO_2$ to $CsPbBr_3$, forming an S-scheme heterojunction in the $TiO_2$/$CsPbBr_3$ nanohybrids that significantly enhances electron–hole pair separation. However, the S-scheme is still in its early stages and requires further research to overcome significant conceptual and practical challenges.

## 7 Applications of $TiO_2$ nanomaterials

The objective of engineering functional $TiO_2$ materials with tailored electronic properties through morphological control, crystal phase manipulation, doping, and hybridization, is to optimize their performance in photocatalytic applications. Extensive efforts have been dedicated to leveraging $TiO_2$ for a wide range of photooxidation reactions such as photodegradation of organic pollutants and photocatalytic disinfection (Tables 1–5). Furthermore, $TiO_2$ has shown promise in photo-

**Table 4** Overview of noble metal modified $TiO_2$ photocatalyst in environmental remediation applications

| Photocatalysts | Synthesis methods ($TiO_2$/noble metals) | Pollutants | Degradation efficiency | Ref. |
|---|---|---|---|---|
| Ag nanoparticles/ mesoporous $TiO_2$ | Pyrolysis/photodeposition | (i) Methylene blue,<br>(ii) Phenol | (i) >90% in 300 min, (ii) 85% in 210 min under visible light | 260 |
| Ag/$TiO_2$ particles | Commercial/electrochemical method | 2-Chlorophenol | 94% in 6 h under UV light | 415 |
| Amine-adsorbed Ag/ $TiO_2$ particles | Sol–gel | Phthalic acid | >90% in 210 min under visible light | 416 |
| Ag/$TiO_2$ nanoparticles | Chemical synthesis | Methylene blue | 89.2% in 60 min under solar light | 417 |
| Biochar-coupled Ag and $TiO_2$ particles | Hydrolysis/photodeposition | Methyl orange | 85.38% in 60 min under UV light | 418 |
| Ag/$TiO_2$ particles | Laser pyrolysis/wet impregnation and chemical reduction | Methyl orange | 90% in 120 min under visible light | 419 |
| Ag/β-cyclodextrin $TiO_2$ membrane | Hydrothermal method/ electrospinning | Dimethyl-hydrazine | 96.8% in 80 min under visible light | 270 |
| Au/$TiO_2$ nanotubes | Electro-spinning/deposition–precipitation | Methylene blue | >80% in 140 min under visible light | 420 |
| Mesoporous Au/$TiO_2$ | Sol gel/deposition–precipitation | Safranin-O | 97% in 60 min under UV light and 87% in 90 min under solar light | 421 |
| One-dimensional Au/ $TiO_2$ nanoforests | Chemical synthesis/ photoreduction | (i) Rhodamine B,<br>(ii) *p*-Nitrophenol,<br>(iii) Phenol | (i) >90% in 60 min under UV and >80% in 60 min under visible light, (ii) >40% in 60 min under UV light, (iii) >45% in 60 min under UV light | 422 |
| Au/$TiO_2$ nanofibers | Electro-spinning | (i) Methylene blue,<br>(ii) Rhodamine B | (i) 88% in 3 h under solar light, (ii) >90% in 3 h min under solar light | 12 |
| Au/$TiO_2$ film | Commercial/sputtering | Methylene blue | 60% in 60 min under 532 nm laser | 423 |
| Au/$TiO_2$ nanostructures | Chemical synthesis | Methylene blue | 97% in 150 min under visible LED light | 168 |
| Au/$TiO_2$ nanorod | Hydrothermal/wet impregnation | Bisphenol A | 40% in 120 min under visible light ($\lambda_{max}$ = 520 nm) | 164 |
| Pt/$TiO_2$ particles | Commercial/Photo-deposition | (i) Acetaminophen,<br>(ii) Panadol | (i) 99% and (ii) 83% in 180 min under simulated solar light | 424 |
| Pt/$TiO_2$@polymeric matrix | Commercial/chemical-reduction | Methylene blue | 83% in 130 min under UV and 94% in 400 min under sunlight | 262 |
| Pd/$TiO_2$ particles | Chemical synthesis/photo-deposition | Amoxicillin | 97.5% in 5 h under visible light | 425 |
| Pd/$TiO_2$ particles | Chemical synthesis/incipient wetness impregnation | Methyl violet | 95% in 20 min under UV light | 426 |
| Pd/$TiO_2$ particles | Sol–gel | (i) Methylene blue,<br>(ii) Methylene orange | (i) 99.4% and (ii) 92.6% in 120 min under UV light | 263 |
| Pd/$TiO_2$ films | Sol–gel | Phenol | 80% in 5 h under UV light and 23% in 5 h under visible light | 427 |
| Au/Pt–$TiO_2$ nanopillar arrays | Glancing angle deposition/ successive ion layer adsorption and reaction | Methyl orange | 40% in 120 min under UV light | 184 |
| Ag@Au/$TiO_2$ nanotubes | Electro-chemical anodization/ displacement reaction | (i) Methyl orange,<br>(ii) Cr(IV) ions | (i) 98.1% and (ii) 70.2% in 120 min under solar light | 428 |
| $Au_{0.4}Ag_{0.6}/TiO_2$ | Chemical synthesis | Methylene blue | 99% in 120 min under visible light | 261 |
| $Ag_{0.1}Au_{0.1}Pt_{0.1}Pd_{0.1}/TiO_2$ | Sol gel/ions reduction | Toluene | 86% in 60 min under LED light ($\lambda_{max}$ = 465 nm) | 429 |

**Table 5** Overview of $TiO_2$ heterojunction photocatalyst in environmental remediation applications

| Photocatalysts | Synthesis methods | Pollutants | Degradation efficiency | Ref. |
|---|---|---|---|---|
| $TiO_2/Ti_3C_2T_x$ composite | Hydrothermal | Carbamazepine | 98.67% in 240 min under UV light and 55.83% in 8 h under solar light | 210 |
| $BiOBr/TiO_2$ | Solvothermal | Rhodamine B | 99.9% in 10 min under visible light | 265 |
| $In_2S_3/TiO_2$ | Hydrothermal | Rhodamine B | 98% in 10 min under simulated solar light | 430 |
| $rGO/TiO_2$-$B/W_{18}O_{49}$ | Solvothermal | Rhodamine B | 100% in 15 min under full solar-spectrum | 264 |
| C-$MoS_2/TiO_2$ | Hydrothermal | Methylene blue | 99% in 60 min under simulated solar light | 266 |
| $CdO/TiO_2$ | Sol–gel | Imazapyr herbicide | 100% in 180 min under visible light | 272 |
| $Pt/Nb_2O_5/TiO_2$ | Photodeposition | (i) Diclofenac, (ii) Ketoprofen | (i) 100% in 20 min under UV light, (ii) 100% in 60 min under UV light | 431 |
| $Bi_2O_3/rGO/TiO_2$ | Hydrothermal | Tetracycline | 94.3% in 90 min under visible light | 278 |
| $Bi_2O_3/Ti^{3+}$–$TiO_2$ | Hydrothermal | Tetracycline | 100% in 200 min under visible light ($\lambda > 420$ nm) | 432 |
| $TiO_2$/g-$C_3N_4$ | Hydrothermal | Ciprofloxacin | 93.4% in 60 min under simulated solar light | 279 |
| g-$C_3N_4$@C-$TiO_2$ | Hydrothermal | (i) Rhodamine B, (ii) Phenol | (i) 97% in 90 min under visible light, (ii) 92% in 60 min under visible light | 433 |
| Cu–Ni/$TiO_2$ | Chemical method | Gaseous acetaldehyde | 88% in 180 min under UV light and 56% in 180 min under visible light | 282 |
| $TiO_2$-RGO/LDHs | Hydrothermal | Gaseous: (i) toluene, (ii) methanol, (iii) ethyl acetate | (i) 69.9%, (ii) 91.6%, (iii) 99.9% in 60 min under simulated sunlight ($\lambda \geq 350$ nm) | 283 |

reduction reactions including hydrogen generation through water splitting (Table 6), carbon dioxide reduction (Table 7), nitrogen fixation (Table 8), hydrogen peroxide generation (Table 9), alcohol oxidation (Table 10) and even in photochromic applications. These advancements in $TiO_2$ photocatalysis aim to unlock the full potential of $TiO_2$ in addressing environmental challenges in water and air pollution as well as advancing sustainable energy solutions.

### 7.1 Photodegradation for environmental remediation

The rapid growing global populations, urbanization and industrialization have caused severe environmental impact such as global warming, climate change, and pollution. Water pollution is a major global environmental issue with detrimental effects on human health and the ecosystem, resulting from discharge of industrial effluent wastes, pharmaceutical wastes and leaching high content of organic substances such as chemical fertilizers and pesticides in aqueous environments.[244–246] According to World Health Organization, an estimated 3.4 million deaths annually are attributable to water-related diseases. Moving forward, half of the world's population will be living in water-stressed areas by 2025. Therefore, re-use of wastewater and to recover water is becoming an important strategy, particularly the world's supply of fresh water is scarce. Over the last decades, Advanced Oxidation Processes (AOPs) have been regarded as effective methods in water purification and wastewater treatment. These processes are light-induced (UV or near-UV) and based on the generation of hydroxyl radicals to oxidize the harmful organic pollutants.[247] Examples of the AOPs processes include ozonation, electrochemical processes, direct decomposition of water and photocatalysis (Fig. 5A).[248,249]

Photocatalysis stands out as one of the most successful and thoroughly investigated AOP. Its application offers a sustainable and environmentally friendly solution to address pollution challenges by utilizing light energy to initiate chemical reactions without producing additional pollutants. This technology finds widespread use in various photodegradation applications, encompassing the elimination of organic pollutants, dyes, and harmful chemicals from both air and water sources. Through photocatalysis, harmful contaminants can be efficiently degraded and transformed into harmless byproducts, contributing to cleaner and healthier environments. The photodegradation of various organic molecules/dyes and photocatalytic disinfection of microbial contaminants in the presence of $TiO_2$ photocatalyst were reviewed and summarized in Table 1.

**7.1.1 Photodegradation of organic dyes.** The development of $TiO_2$ photocatalysts with enhanced activity has been achieved through facet-engineering strategies. Specifically, (001)-exposed anatase $TiO_2$ nanosheets were prepared to optimize the photodegradation of Rhodamine B molecules.[250] Various anatase $TiO_2$ nanostructures with different sizes and morphologies were synthesized by tuning the hydrolysis rates of reaction precursors under solvothermal conditions. These nanostructures significantly enhanced the photocatalytic degradation of Rhodamine B, with the $TiO_2$ nanosheet photocatalyst achieving nearly complete degradation after 15 minutes of irradiation, approximately twice the efficiency of P-25 $TiO_2$. The enhancement is attributed to the nanosheets' larger specific surface areas and active surfaces, which enable greater dye molecule adsorption and light absorption. Moreover, the nanosized effect of the thin nanosheets contributes to reduced bulk electron–hole recombination, faster interfacial charge carrier transfer, and easier charge carrier trapping.

In recent studies on $TiO_2$ facet engineering, a series of anatase $TiO_2$ nanoparticles with varying percentages of (001) and (101) facets were synthesized *via* the hydrothermal method.[251] By adjusting the hydrofluoric acid concentration, the (001) facet percentage was increased to nearly 100%. However, excessive hydrofluoric acid dissolved small crystal

Table 6 Overview of $TiO_2$-based photocatalyst in photocatalytic water splitting for hydrogen production

| Photocatalysts | Synthesis methods | Light source | $H_2$ generation rate | Quantum efficiencies | Ref. |
|---|---|---|---|---|---|
| $TiO_2$ hollow spheres | Solvothermal/chemical reduction | 300 W Xe lamp | 0.182 mmol $g^{-1}$ $h^{-1}$ | — | 292 |
| $TiO_2$ hollow sphere | Al reduction | 300 W Xe lamp | 56.7 mmol $h^{-1}$ $g^{-1}$ | 90.6% (365 nm) | 194 |
| $TiO_2$ microspheres | Confinement reduction route | Visible light ($\lambda$ > 400 nm) | 42.6 μmol $h^{-1}$ | 12.7% (420 nm) and 2.8% (520 nm) | 189 |
| Sr-$TiO_{2-x}$ ($x$ = 0.3%) + Pt co-catalyst | Template assisted synthesis | 300 W Xe lamp | 19 442 μmol $g^{-1}$ $h^{-1}$ | — | 400 |
| Rh-loaded $TiO_2$ | Impregnation/calcination/hydrogenation | Solar simulator with AM 1.5G filter | 7.27 mmol $g^{-1}$ $h^{-1}$ | 0.0231% (420 nm) | 434 |
| Carbonate-doped phase-junction $TiO_2$ nanotubes | Emulsion electrospinning method | Solar simulator with AM 1.5G filter | 6108 μmol $h^{-1}$ $g^{-1}$ | 83% (365 nm) | 290 |
| Anatase/rutile $TiO_2$ with hydrogenated heterophase interface structures | Hydrothermal/hydrogenation | UV-vis light, 100 mW $cm^{-2}$ | 136.5 μmol $cm^{-2}$ $h^{-1}$ | — | 289 |
| Anatase/rutile $TiO_2$ | MOF-mediated synthesis | UV-vis light, 300 W Xe lamp | 1394 μmol $g^{-1}$ $h^{-1}$ | — | 294 |
| $Ti_3C_2$/$TiO_2$ nanoflowers | Oxidation and alkalization/ion exchange and calcination | 300 W Xe arc lamp | 526 μmol $g^{-1}$ $h^{-1}$ | 5.86% (350 nm) | 208 |
| $TiO_2$/Ti-MOF + Pt co-catalyst | Solvothermal | 300 W Xe lamp (420–760 nm) | 12.4 mmol $g^{-1}$ $h^{-1}$ | 19.17% (420 nm) | 295 |
| PdAu–$TiO_2$–aerogel | Wet chemistry synthesis/supercritical drying | Solar simulator, 100 mW $cm^{-2}$ | 22 μmol $g^{-1}$ $h^{-1}$ | — | 222 |
| Pd–$TiO_2$–aerogel | Microwave synthesis/supercritical drying | Visible light (400–800 nm) | 117.5 mmol $g^{-1}$ $h^{-1}$ | 30.9% (430 nm) | 302 |
| N–$TiO_2$–aerogel | Plasma-enhanced chemical vapor deposition | Visible-light irradiation | 3.1 mmol $g^{-1}$ $h^{-1}$ | 5.6% (450 nm) | 300 |
| $TiO_2$/g-$C_3N_4$ core–shell fibers | Electrospinning | 300 W Xe lamp ($\lambda \geq$ 420 nm) | 436 μmol $g^{-1}$ $h^{-1}$ | — | 435 |
| $TiO_2$ microflowers/g-$C_3N_4$ | Hydrothermal | 350 W Xe lamp | 4128 μmol $g^{-1}$ $h^{-1}$ | — | 436 |
| CdS/$TiO_2$ nanofibers | Electrospinning | 350 W Xe lamp | 2.32 mmol $g^{-1}$ $h^{-1}$ | 10.14% | 437 |
| $ZnIn_2S_4$/$TiO_2$ heterostructure | Hydrothermal | 300 W Xe arc lamp | 6.03 mmol $g^{-1}$ $h^{-1}$ | 10.49% (365 nm) | 438 |
| $TiO_2$/$NiCo_2S_4$ core–shell structure | Solvothermal | 300 W Xe lamp | 8.55 mmol $g^{-1}$ $h^{-1}$ | — | 439 |
| $Bi_2WO_6$/$TiO_2$ heterostructure | Solvothermal | 300W Xe lamp | 12.9 mmol $g^{-1}$ $h^{-1}$ | — | 440 |
| $TiO_2$/ZnTe/Au nanocorncob | Hydrothermal | 300W Xe lamp | 3344.0 μmol $g^{-1}$ $h^{-1}$ | — | 441 |
| Multi-edged $TiO_2$@Ru atoms | Chemical synthesis | 300W Xe lamp | 323.2 μmol $h^{-1}$ per 50 mg | — | 53 |
| Ru single atoms-$RuO_2$/$TiO_2$ | Solvothermal/impregnation-adsorption | 300 W Xe lamp, 200 mW $cm^{-2}$ | 2.91 mmol $g^{-1}$ $h^{-1}$ | 2.24% in benzyl-alcohol and 30.84% in methanol (365 nm) | 297 |

Table 7 Overview of $TiO_2$-based photocatalyst in $CO_2$ photoreduction

| Photocatalysts | Synthesis methods | Light source | Gas generation rate | Quantum efficiencies | Ref. |
|---|---|---|---|---|---|
| Eu–$TiO_2$ nanoparticles | Sol–gel | 300 W Xe arc lamp | 65.53 μmol $g^{-1}$ ($CH_4$) and 42.91 μmol $g^{-1}$ per 9 h (CO) | — | 442 |
| Ag/$TiO_2$ nanoparticles | Chemical synthesis | 300 W Xe lamp with AM 1.5G filter | 46 mmol $g^{-1}$ $h^{-1}$ ($CH_4$) | — | 308 |
| $Cu_{0.8}Au_{0.2}$/$TiO_2$ | Photodeposition | 300 W Xe lamp (500 mW $cm^{-2}$) with AM 1.5G filter | 3578.9 μmol $g^{-1}$ $h^{-1}$ ($CH_4$) and 369.8 μmol $g^{-1}$ $h^{-1}$ for $C_2H_4$ | — | 312 |
| N-doped carbon dots decorated $TiO_2$ hollow spheres | Chemical synthesis | 300 W Xe arc lamp | 26.8 μmol $h^{-1}$ $g^{-1}$ ($CH_4$) | 0.87% (365 nm) | 443 |
| $TiO_2$/$NH_2$-UiO-66 (MOF) | Hydrothermal/microwave | UV-vis light ($\lambda$ > 325 nm, 300 W) | 1.8 μmol $g^{-1}$ $h^{-1}$ (CO) | — | 309 |
| $TiO_2$/MIL-101-Cr-$NO_2$ (MOF) | Chemical synthesis | 300 W Xe lamp | 12 mmol $g^{-1}$ $h^{-1}$ (CO and $CH_4$) | 11.3% (350 nm) | 319 |
| Cu/$TiO_2$-aerogel | Hydrothermal/supercritical drying | UV-A/vis light (320–500 nm) | 28.2 μmol $g^{-1}$ $h^{-1}$ (CO) | — | 314 |
| Pd-porphyrin-based polymers coated hollow $TiO_2$ | Chemical synthesis | 300 W Xe lamp (325–780 nm) | 48 μmol $g^{-1}$ $h^{-1}$ ($CH_4$) and 34.0 μmol $g^{-1}$ $h^{-1}$ (CO) | — | 311 |
| $TiO_2$@polydopamine hollow spheres | Chemical synthesis | 350 W Xenon lamp | 1.50 μmol $g^{-1}$ $h^{-1}$ ($CH_4$) | — | 444 |
| (001)$TiO_2$-g-$C_3N_4$/$BiVO_4$ nanosheet | Solvothermal | 300 W Xe lamp with 420 nm cut-off filter | 65 μmol $g^{-1}$ per 4 h ($CH_4$) | — | 320 |
| $ZnIn_2S_4$ nanosheets/$TiO_2$ nanobelts | Solvothermal | 300W Xe lamp | 1.135 μmol $g^{-1}$ $h^{-1}$ ($CH_4$) | — | 239 |
| C-$TiO_2$/β-$Bi_2O_3$ | Chemical synthesis | 300DUV Xe lamp with AM 1.5G filter | 31.07 μmol $g^{-1}$ $h^{-1}$ (CO) | — | 445 |
| $TiO_2$/$CsPbBr_3$ nanofibers | Electrospinning/colloidal synthesis | 300 W Xe arc lamp | 9.02 μmol $g^{-1}$ $h^{-1}$ (CO) | — | 243 |

**Table 8** Overview of $TiO_2$-based photocatalyst in $N_2$ fixation

| Photocatalysts | Synthesis methods | Light source | $NH_3$ generation rate | Quantum efficiencies | Ref. |
|---|---|---|---|---|---|
| Defective $TiO_2$ nanoparticles | Sol–gel | 300 W Xe lamp (full spectrum) | 324.86 mmol $g^{-1}$ $h^{-1}$ | 1.1% (365 nm) | 325 |
| Defective $TiO_2$ particles | Hydrothermal | 300 W Xe lamp (full spectrum) | 64.82 μmol $g^{-1}$ $h^{-1}$ | — | 446 |
| Defective $TiO_2$ nanotubes | Hydrothermal | 300 W Xe lamp (full spectrum) | 1.2 mmol $L^{-1}$ $h^{-1}$ | — | 330 |
| Defective Cu–$TiO_2$ nanosheets | Hydrothermal | 300 W Xe lamp (full spectrum) | 78.9 μmol $g^{-1}$ $h^{-1}$ | 0.08% (600 nm) and 0.05% (700 nm) | 52 |
| Ru atom decorated $TiO_2$ nanosheets | Hydrothermal | 300 W Xe lamp | 56.3 μg $g^{-1}$ $h^{-1}$ | — | 328 |
| Defective C-$TiO_2$ | Calcination | 300 W Xe lamp (200–800 nm) | 84 μmol $g^{-1}$ $h^{-1}$ | 0.04% (400 nm) and 0.01% (420 nm) | 326 |
| $Mo_2C/TiO_2$ | Sintering | 300 W Xe lamp (UV) | 432 μg $g^{-1}$ $h^{-1}$ | 0.1% (365 nm) | 329 |
| $TiO_2$@C/g-$C_3N_4$ | Calcination | 300 W Xe lamp with 420 nm cutoff filter | 250.6 mmol $g^{-1}$ $h^{-1}$ | 0.14% (420 nm) | 327 |
| Ce/S co-doped $TiO_2$ | Chemical synthesis | 300 W Xe lamp with 420 nm cutoff filter | 382.4 mmol $g^{-1}$ $h^{-1}$ | 3.32% (420 nm) | 447 |
| N-$TiO_2$ hollow microspheres | Hydrothermal | 300 W Xe lamp ($\lambda > 400$ nm) | 80.09 μmol $g^{-1}$ $h^{-1}$ | 0.07% (375 nm) | 114 |
| N-$TiO_2/Ti_3C_2$ | Hydrothermal | 500 W Xe lamp (100 W $cm^{-2}$) | 415.6 μmol $g^{-1}$ $h^{-1}$ | — | 32 |

**Table 9** Overview of $TiO_2$-based photocatalyst in $H_2O_2$ generation

| Photocatalysts | Synthesis methods | Light source | $H_2O_2$ generation rate | Quantum efficiencies | Ref. |
|---|---|---|---|---|---|
| $TiO_{2-x}/C_3N_5$ | Hydrothermal/polymerization and solvent exfoliation | 300 W Xe lamp | 2.93 μmol $L^{-1}$ $min^{-1}$ | — | 339 |
| $Au/Bi_2O_3$–$TiO_2$ | Chemical synthesis/deposition | 300 W Xe lamp | 11.2 mM per 12 h | — | 448 |
| $TiO_2/ZnIn_2S_4$ | Chemical synthesis/solvothermal | Simulated natural light source (400 nm $\leq \lambda \leq$ 760 nm, 100 mW $cm^{-2}$) | 1530.59 μmol $g^{-1}$ $h^{-1}$ | 10.39% (400 nm) | 19 |
| $TiO_2$/Au/MXene | Hydrothermal, photodeposition | UV light (360 nm $< \lambda <$ 380 nm, 1 mW $cm^{-2}$) | 6.80 mg per L per 4 h | — | 341 |
| $TiO_2$@BTTA (COF) | Electrospinning/chemical synthesis | 300 W Xe lamp ($\lambda$ = 350–780 nm, 0.64W $cm^{-2}$) | 740 μmol $L^{-1}$ $h^{-1}$ | 5.48% (365 nm) | 342 |
| $TiO_2/Bi_2O_3$ on polystyrene spheres | Hydrothermal/photodeposition | 300 W Xenon arc lamp ($\lambda$ = 350–780 nm) | 1.15 mM $h^{-1}$ | 1.25% (365 nm) | 54 |
| S-doped g-$C_3N_4/TiO_2$ | Chemical synthesis/electrostatic self-assembly | 300 W Xe lamp | 2128 μmol $h^{-1}$ $g^{-1}$ | 0.61% (365 nm) | 340 |

**Table 10** Overview of $TiO_2$-based photocatalyst in selective oxidation of alcohol

| Photocatalysts | Synthesis methods | Light source | Alcohol | Product | Solvent | Conv. % | Sel. % | Ref. |
|---|---|---|---|---|---|---|---|---|
| Gd-$TiO_2$/poly(*o*-phenylenediamine) nanowires | Hydrothermal/photopolymerization | Simulated solar light | Benzyl alcohol | Benzaldehyde | Acetonitrile | 96.0 | 97.5 | 346 |
| $TiO_2/Ti_3C_2$ | Hydrothermal | 300 W Xe lamp (385–740 nm) | Furfuryl alcohol | Furfural | Acetonitrile | >99 | >99 | 22 |
| $TiO_2/Ti_3C_2$ | Chemical synthesis/calcination oxidation | 300 W Xe lamp | Benzyl alcohol | Benzaldehyde | *n*-Hexane | 97 | 98 | 343 |
| $TiO_2$@COF | Hydrothermal/chemical synthesis | White LED (5 W, $\lambda = 420–780$ nm, 150 mW $cm^{-2}$) | Benzyl alcohol | Benzaldehyde | Acetonitrile | 92.5 | 99.9 | 21 |
| COF@$TiO_2$ core–shell heterojunction | Chemical synthesis | 300 W Xe lamp ($\lambda \geq 420$ nm) | Benzyl alcohol | Benzaldehyde | Benzotrifluoride | 84 | 93 | 218 |

Conv. %: conversion % and Sel %: selectivity %.

seeds, disrupting crystal growth balance. Optimal photocatalytic efficiency for Rhodamine B decomposition was achieved with 73% exposed (001) facets. Additionally, nanoflower-like rutile $TiO_2$ was synthesized and immobilized on basil seeds for methylene blue photodegradation.[252] This structure, with small particle size and large surface area, enhanced adsorption and degradation, achieving a 98.95% removal efficiency under solar light within 180 minutes.

Metal ion doping in $TiO_2$ significantly enhances its photocatalytic properties, particularly for photodegradation applications.[66,253,254] Li-doped $TiO_2$ shows up to 2.2 times higher efficiency than undoped $TiO_2$ [67] and up to 5 times higher efficiency than commercial P25 under visible light.[255] Specifically, doping $TiO_2$ with 1.0 mol% $Li^+$ lowers the anatase-to-rutile transformation temperature and creates a mixed-phase composition of 27.1% rutile and 72.9% anatase at 550 °C, significantly improving the photocatalytic degradation rate of methyl orange.[67] In addition, transition metal ion doping with Al, Cu, Mo, and W also boosts photocatalytic performance for Rhodamine B dye degradation.[256] Al and Cu doping increased activity to 70%, while Mo and W doping achieved 96% under visible light irradiation for 60 minutes. Surface analysis shows that Mo and W doping introduces surface hydroxyl groups essential for photodegradation and increases surface acidity, particularly in W-doped $TiO_2$, which enhances its affinity for chemical particles with unpaired electrons.

The source of dopant and the doping process significantly influence nitrogen incorporation in N-doped $TiO_2$ nanoparticles. Acidic doping using $HNO_3$ incorporates nitrogen into substitutional positions, while doping with urea results in interstitial positions, both enhancing photocatalytic activity in the visible range.[257] N-doped $TiO_2$ from the acidic process demonstrates superior photodegradation of methyl orange due to better UV-visible light absorption. In P-doped $TiO_2$, phosphorus doping in the form of $P^{5+}$ inhibits crystalline growth, increases surface area, and narrows band gap energies, leading to effective methylene blue degradation.[258] Cationic S-doped $TiO_2$, with sulfur atoms as $S^{4+}$ substituting lattice Ti atoms, shifts the absorption edge to a lower energy level, enabling visible light photocatalytic degradation of methylene blue and 2-propanol at longer wavelengths.[259]

Incorporating Ag nanoparticles into $TiO_2$ enhances photocatalytic activity due to plasmonic effects.[260] Ag/$TiO_2$ composites with 50–100 nm Ag nanoparticles show improved degradation of methyl blue and phenol under simulated sunlight, due to better charge carrier separation and plasmon-enhanced light absorption. However, excessive Ag loading can reduce efficiency by covering active sites and promoting electron–hole recombination. Similarly, $TiO_2$/Au nanofiber composites achieve high photocatalytic performance, with 88% degradation of methylene blue and nearly complete degradation of Rhodamine B under solar light.[12] This is attributed to plasmonic hot electrons from Au nanoparticles and efficient charge separation at the Au–$TiO_2$ interface. Bimetallic Au–Ag/$TiO_2$ composites further enhance photocatalytic activity. The pres-

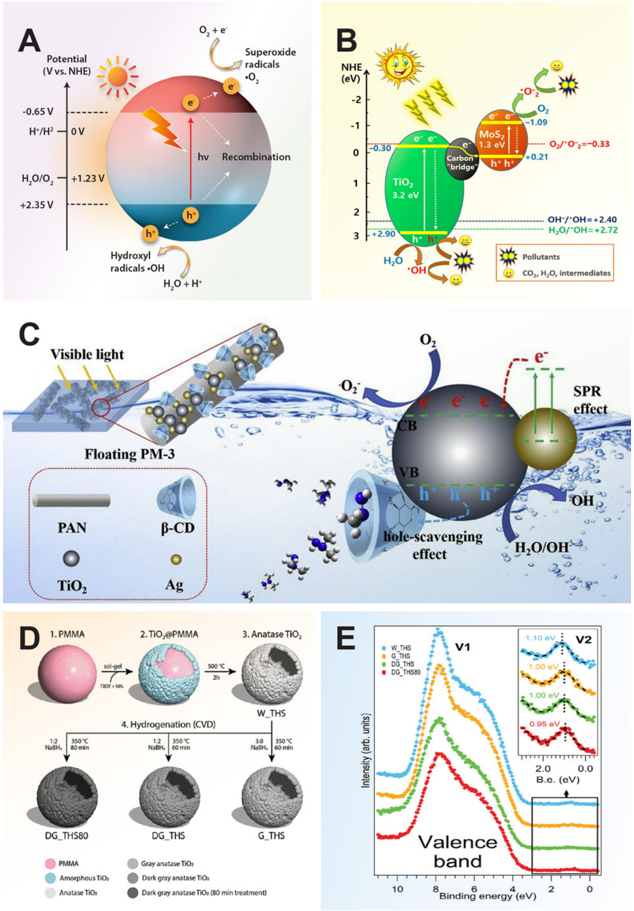

Fig. 5 (A) Schematic illustration of a general photodegradation mechanism of $TiO_2$ semiconductor. (B) Mechanism of Z-scheme heterojunction C-$MoS_2$/$TiO_2$ photocatalyst for organic pollutant degradation under solar light. Reproduced with permission from ref. 266. Copyright 2022, Elsevier. (C) Photodegradation with Ag/β-cyclodextrin co-doped $TiO_2$ floating photocatalytic membrane. Reproduced with permission from ref. 270. Copyright 2020, Elsevier. (D) Synthesis of $TiO_2$ hollow spheres by a hard template-based method, followed by chemical reduction under controlled conditions. (E) X-ray photoelectron spectroscopy characterization showing the valence band spectra and a zoom of the fundamental gap region of the colored $TiO_2$ hollow spheres, where defect states (V2) are detected. Reproduced with permission from ref. 55. Copyright 2023, Wiley-VCH.

ence of Au–Ag alloy nanoparticles shifts the light absorption from UV to visible spectrum and improves plasmonic effects, resulting in up to 99% degradation of methylene blue under visible light.[261]

Encapsulating $TiO_2$ within a polymer matrix and coating it with Pt nanoparticles enhances photocatalytic degradation of methylene blue.[262] The Pt/$TiO_2$ composite achieved 83% degradation under UV light in 130 minutes and 94% under direct sunlight in 400 minutes. Similarly, a Pd/$TiO_2$ photocatalyst degraded binary dyes, achieving 83.4% mineralization of methylene blue and 75.3% of methyl orange under UV light in 180 minutes, with methylene blue degrading faster due to its thiazine structure compared to the azo bond in methyl orange.[263] Au/Pt-modified $TiO_2$ nanopillar arrays further improved photocatalytic efficiency. Depositing ∼4 nm Au/Pt nanoparticles onto the arrays enhanced UV and visible light absorption, leading to 21- and 13-times higher photocatalytic efficiency under UV-vis and visible light, respectively.[184] This demonstrates the potential of combining noble metal nanoparticles with $TiO_2$ to harness the entire solar spectrum effectively through plasmonic and electron sink effects.

Constructing heterojunctions by coupling two semiconductors together is one of the most efficient ways for achieving high pollutant degradation efficiency. For example, a Z-scheme reduced graphene oxide (rGO)/$TiO_2$-bronze ($TiO_2$-B)/$W_{18}O_{49}$ photocatalyst, composed of rGO, ultra-thin $TiO_2$-B nanosheets, and $W_{18}O_{49}$ nanofibers, can absorb sunlight from ultraviolet to near-infrared regions.[264] This broad absorption spectrum enables the efficient photocatalytic degradation of Rhodamine B by making full use of available light.

A 1D BiOBr/$TiO_2$ nanorod heterojunction composite was designed through molecular and interface engineering for efficient removal of organic dye.[265] This composite enhances photocatalytic activity by promoting charge migration and separation of photogenerated electron–hole pairs. The heterojunction acts as a nanochannel, facilitating the rapid transfer of photogenerated holes from the VB of BiOBr to the VB of $TiO_2$ nanorods, leveraging BiOBr's higher VB (+3.04 eV) compared to $TiO_2$ nanorods (+2.6 eV). This results in superior photodegradation of Rhodamine B, with an apparent rate constant of 0.49 $min^{-1}$ and an 88.5% total organic carbon removal ratio. The efficient separation and extended lifetime of charge carriers allow the holes on the VB of $TiO_2$ nanorods to oxidize Rhodamine B into $CO_2$ and $H_2O$.

A Z-scheme photocatalyst was constructed using a hydrothermal method, combining carbon-modified $MoS_2$ (C-$MoS_2$) sheets with octahedral anatase $TiO_2$ nanocrystals, achieving 99% methylene blue degradation with a low catalyst loading (0.2 g $L^{-1}$) under simulated solar light in 60 minutes.[266] The C-$MoS_2$ acts as an electron mediator, facilitating efficient electron–hole separation. The electron-rich (101)-faceted $TiO_2$ supports the Z-scheme recombination of electrons from $TiO_2$'s CB and holes from $MoS_2$'s VB. The coupling of (101)-exposed $TiO_2$ and 2H-$MoS_2$, along with solid-state electron mediators 1T-$MoS_2$ and carbon, enhances light absorption and accelerates charge transfer at the interface, significantly boosting photocatalytic activity compared to P25, $MoS_2$/$TiO_2$, and C-$MoS_2$ alone (Fig. 5B). The effective separation of electron–hole pairs prolongs their lifetime, facilitating oxidation and reduction reactions in the degradation process.

**7.1.2 Photodegradation of organic pollutants.** Studies have shown that modifying $TiO_2$ nanorods enhances the photocatalytic activity compared to unmodified P-25 $TiO_2$.[267] These modifications, including increased surface area, anatase content, crystallite size, and decreased band gap energy, improve photodegradation efficiency of *p*-cresol by facilitating better light absorption, charge carrier generation, and interfacial interactions. In addition, highly crystalline, phase-pure brookite $TiO_2$ films with pyramidal features have been fabricated *via* chemical vapor deposition for degrading stearic acid.[268] These brookite films exhibit superior photocatalytic activity under UVA (365 nm) irradiation compared to anatase films. Despite having similar electron–hole recombination dynamics, the enhanced performance of brookite is attributed to its more structured morphology and higher surface area.

Non-metal ion doping with sulfur in $TiO_2$ photocatalysts enhances visible light absorption and reduces the band gap to 2.78 eV due to sulfur-induced structural defects.[137] The sulfur is primarily present as cationic $S^{6+}/S^{4+}$ species, which enhance photocatalytic oxidation of acetaldehyde by capturing electrons and improving electrical conductivity. Comparative studies reveal that cationic S-doping ($S^{6+}$ substituting $Ti^{4+}$) reduces $TiO_2$ grain size due to the smaller ionic radius of $S^{6+}$, while anionic S-doping ($S^{2-}$ substituting $O^{2-}$) increases grain size.[138,140] Cationic S-doping leads to enhanced visible light absorption and photocatalytic activity through chemisorbed hydroxyls and photoinduced holes, while anionic S-doping contributes equally through electrons and holes.

The presence of bimetallic alloy nanoparticles, such as Au–Pd, significantly influences the photocatalytic reaction of phenol decomposition.[269] These nanoparticles act as mediators in undesired redox reactions that would otherwise consume photogenerated radicals inefficiently. As a result, they enhance the photo-oxidation efficiency of toxic aromatic compounds like phenol. Furthermore, the $TiO_2$ photocatalyst supported by Au–Pd demonstrated superior long-term photoactivity, achieving approximately 90% phenol decomposition under UV irradiation.

A floating photocatalytic membrane composed of Ag and β-cyclodextrin co-doped $TiO_2$ has been developed for the dynamic adsorption and degradation of dimethylhydrazine under visible light.[270] This membrane combines the photocatalytic properties of $TiO_2$ with enhanced adsorption capabilities due to β-cyclodextrin, while Ag doping extends the light absorption into the visible spectrum, resulting in efficient degradation of the contaminant. When placed on the surface of shallow water, the membrane exhibits dual functionality through adsorption and photoactivity under visible light and oxygen. The unique cone-shaped structure of β-cyclodextrin, with its hydrophilic outer surface and lipophilic inner cavity, enhances the adsorptive capacity, making it effective in entrapping target pollutants like unsymmetrical dimethylhydrazine. Besides, Ag nanoparticles enhance light absorption *via* surface plasmon resonance, while $TiO_2$ nanoparticles improve photoresponse performance across UV and visible light regions. Upon excitation, β-cyclodextrin acts as a hole-scavenger, effectively suppressing electron–hole pair recombination (Fig. 5C).

**7.1.3 Photodegradation of herbicides and pesticides.** The photocatalytic investigation of B-doped $TiO_2$ indicates that a concentration range of 0.5–0.8 wt% of interstitial boron is more effective than pure $TiO_2$ for degrading four herbicides and pesticides: diuron, *o*-phenylphenol, 2-methyl-4-chlorophenoxy-acetic acid, and terbuthylazine under simulated solar irradiation.[271] The B-doped $TiO_2$ photocatalyst, synthesized *via* the sol–gel procedure, exhibits a reduction in the crystal size of $TiO_2$ particles, along with an increase in pore volume and specific surface area compared to pure $TiO_2$. Furthermore, the presence of boron in interstitial positions within the $TiO_2$ structure restrains the recombination process, thereby enhancing the photocatalytic activity of $TiO_2$.

To effectively degrade Imazapyr herbicide, mesoporous CdO–$TiO_2$ nanocomposites were synthesized using a sol–gel method. These nanocomposites demonstrated photodegradation rates that were 12.2 and 24.5 times higher than those of $TiO_2$ and P25, respectively.[272] To selectively degrade 2,4-dichlorophenoxyacetic acid herbicide and imidacloprid insecticide from water, the combination of molecular imprinting and photocatalysis was investigated. These common agricultural pesticides were used as templates during synthesis and removed through calcination. The synthesized imprinted $TiO_2$ material selectively interacted with the herbicide and insecticide, demonstrating significantly enhanced photocatalytic activity compared to bare $TiO_2$.[273,274]

**7.1.4 Photodegradation of pharmaceutical contaminants.** The superior photocatalytic activity of triphasic $TiO_2$ (76% anatase, 7% rutile, 17% brookite) for metformin degradation highlights the importance of polymorphic diversity in $TiO_2$-based materials.[61] The combination of multiple phases enhances performance by suppressing electron–hole recombination and improving charge carrier separation. Interestingly, specific surface area did not correlate with photocatalytic activity, as triphasic $TiO_2$ outperformed pure anatase and pure rutile despite their larger surface areas. This suggests a complex interplay between crystal structure, phase composition, and surface characteristics in determining $TiO_2$'s photocatalytic behavior.

Non-metal ion doping in $TiO_2$ has proven effective for degrading various pharmaceutical compounds in wastewater. A 8 wt% B-doped $TiO_2$ achieved over 75% degradation efficiency for compounds like 2,4-dichlorophenol, bisphenol-A, ibuprofen, and flurbiprofen under visible light.[275] A 5 wt% B-doped $TiO_2$ showed 70% removal efficiency of metoprolol under simulated sunlight, compared to 48% with pure $TiO_2$.[276] The improved performance is due to increased visible light absorption, smaller crystal and particle sizes, mesoporous anatase-rutile structures, and interstitial boron positions reducing electron–hole recombination. Likewise, P-doped $TiO_2$ with surface oxygen vacancies effectively degrades ciprofloxacin under visible light by narrowing the $TiO_2$ band gap and enhancing charge separation.[277] Surface oxygen vacancies act as charge traps and adsorption sites, facilitating efficient photogenerated charge transfer and additional reaction sites.

The effectiveness of nanostructured photocatalysts, particularly $TiO_2$ hollow spheres made of self-assembled nanoparticles, is driven by their tailored chemical structure and morphology. These hollow spheres leverage a combination of factors such as high surface area and strong light scattering, which concentrate light within a confined volume, increasing absorption probabilities. Hydrogenated or colored $TiO_2$ hollow spheres, consisting of hierarchically assembled nanoparticles (Fig. 5D), expand solar spectrum absorption up to 1200 nm.[55]

This engineered surface boosts charge photogeneration, leading to significant photocatalytic efficacy, achieving 82% degradation of ciprofloxacin after 6 hours under simulated sunlight. Valence band analysis shows prominent O 2p-related states between 3 and 10 eV (V1) and a less intense Ti 3d-derived state at around 1 eV (V2), as highlighted in the inset (Fig. 5E). The binding energy of V2 shifts from 1.10 to 0.95 eV as the $TiO_2$ hollow spheres transition from white to dark gray, moving closer to the conduction band minimum. The V2/V1 ratio, increasing from 1.7 to 3.0, indicates a higher concentration of oxygen vacancies in the dark gray samples. This analysis highlights the defect characteristics of $TiO_2$ hollow spheres and their implications for efficient photocatalysis.

The heterostructural $TiO_2/Ti_3C_2$ nanosheet-based composite have been studied for the photocatalytic degradation of pharmaceuticals compounds. The $TiO_2$ (0 0 1) facet-decorated $Ti_3C_2T_x$ MXene was synthesized by a hydrothermal process and demonstrated a photocatalytic degradation of 98.67% of the antiepileptic drug carbamazepine, under UV light irradiation.[210] The significant degradation enhancement from 60% for the pristine $Ti_3C_2$ MXene could be attributed to the extra holes and electrons generated by (001) facets of $TiO_2$ embedded in $Ti_3C_2$ sheets, together with Schottky junctions formed between $TiO_2$–MXene interfaces. Findings has revealed that pH was found to have a noteworthy effect on the carbamazepine degradation kinetics, with lower pH values of 3.0–5.0 are more favourable due to the nanocomposite surface being positively charged from $H^+$ ions. Combined with a strong oxidation ability of $TiO_2/Ti_3C_2$ photocatalyst, it would ultimately degrade the carbamazepine into $CO_2$ and $H_2O$ by the end of the reaction.

A ternary heterojunction composite of $Bi_2O_3$, $TiO_2$, and rGO was produced *via* a one-step hydrothermal process.[278] This $Bi_2O_3$/rGO/$TiO_2$ composite exhibited strong visible-light responsiveness and high separation efficiency of photogenerated carriers due to the Bi–Ti heterojunction, resulting in good photocatalytic activity towards tetracycline under visible-light irradiation. Besides, a Z-scheme nanocomposite of 1D/2D $TiO_2$ nanorods and g-$C_3N_4$ nanosheets was successfully fabricated, achieving 93.4% degradation of ciprofloxacin in 60 minutes.[279] Under simulated sunlight irradiation, the nanocomposite's photodegradation rate was 2.3 times higher than that of commercial $TiO_2$ powder and 7.5 times higher than that of g-$C_3N_4$ nanosheets alone.

Recently, photocatalytic foams are emerging as an effective alternative to traditional slurry and supported catalysts due to their unique structural advantages. Their hierarchical porosity, encompassing both macro and micro levels, provides expansive surface areas akin to slurries. This structure facilitates better interaction between pollutants and the photocatalyst surface, overcoming the diffusion limitations typically associated with supported photocatalysts. The development of photocatalytic foams has been significantly advanced by 3D printing technologies. These technologies offer precise control over the design and fabrication process, allowing for the creation of complex structures with tailored porosity and flow characteristics. By building objects layer by layer from digital designs, 3D printing can produce foams with optimized pore sizes and shapes, enhancing pollutant flow and contact with the photocatalyst surface. Mattia and co-workers introduced 3D printed $TiO_2$ foams that are nanoparticle-free, mechanically robust, and photoactive. These foams offer a promising alternative to slurry photocatalysts for the degradation of pharmaceuticals. In their study, the foams were tested using carbamazepine, a common pharmaceutical pollutant in waterways, within a recirculating flow reactor. The results revealed a quantum yield of $7.6 \times 10^{-3}$ and an electrical energy per order of 67.6 kW h $m^{-3}$. These figures indicate that the 3D printed $TiO_2$ foams outperformed traditional $TiO_2$ nanoparticle slurries in terms of efficiency and energy consumption.[57]

**7.1.5 Photocatalytic disinfection.** A recent study explored the use of floating $TiO_2$ photocatalysts to remove microbial contaminants from reclaimed water. Anatase phase $TiO_2$ films were deposited on polystyrene beads *via* magnetron sputtering. Tests on *Escherichia coli* (*E. coli*) showed that UVB irradiation alone only disrupted the outer membrane, insufficient for effective inactivation. However, combining $TiO_2$ with UVB light significantly improved the inactivation rate of *E. coli* to over 90% in 45 minutes, destroying both the outer membrane and the peptidoglycan layer.[280]

Transition metal ion doping in $TiO_2$, such as Fe-doped $TiO_2$, significantly enhances antibacterial properties. Under 365 nm UV light, Fe-doped $TiO_2$ samples (1% to 10%) demonstrated inhibition rates of 67.5% to 99.4% against bacterial growth.[87] This improvement is due to the formation of oxygen vacancies and a reduced optical gap in $TiO_2$, leading to better light absorption and reactive oxygen species generation, which damage bacterial cells. Fe doping proves effective even against antibiotic-resistant strains like *E. coli* by generating reactive oxygen species, causing DNA damage, and peroxidizing membrane phospholipids, thus inhibiting respiration. Co-doping with cerium (Ce) and erbium (Er) also enhances antibacterial efficacy.[281] Ce doping reduces the band gap, allowing absorption of both UV and visible light, while Er doping shifts NIR light into the visible range, increasing light absorption. The combination of Ce and Er co-doping inhibits the recombination of photogenerated charge carriers, resulting in antibacterial efficiencies of 91.23% against *Staphylococcus aureus* and 92.8% against *E. coli*.

**7.1.6 Photodegradation of air pollutants.** The photocatalytic degradation of hydrogen sulfide ($H_2S$) was investigated using a series of $TiO_2$ photocatalysts modified by trivalent metal ions such as Al, gallium (Ga), and indium (In).[85] The study revealed that 4% In doped $TiO_2$ exhibited the highest photocatalytic $H_2S$ removal efficiency of 100% over a duration of 120 minutes, nearly 3 times higher than that of commercial P25 $TiO_2$. The incorporation of Group-IIIA metal ions into $TiO_2$ resulted in the formation of a shallow acceptor level above the valence band in the energy band structure, leading to a slight redshift at the edge of the visible light absorption band and a decrease in the electron–hole recombination rate. Furthermore, $In^{3+}$ doping into $TiO_2$ promoted photothermal-catalytic oxidation reactions on the surfaces of In-$TiO_2$, thereby significantly enhancing the desulfurization efficiency of $H_2S$.

Acetaldehyde, a common volatile organic compound in the environment, was used to assess the photodegradation efficiency of various $TiO_2$ nanocomposites. In this study, Cu–Ni bimetallic nanowires were incorporated into a $TiO_2$ matrix *via* a one-step hydrolysis process to form a new heterostructured photocatalyst.[282] This composite achieved photodegradation efficiencies of 88% under UV light and 56% under visible light for flowing acetaldehyde gas. The enhanced performance is attributed to one-dimensional electron pathways, surface plasmon resonance effects, and an improved bimetallic Schottky barrier. This study provides insights into photon-generated carrier separation and transmission in metal–semiconductor networks and presents an effective method for developing bimetal-based heterostructured photocatalysts.

Combining rGO and layered double hydroxides (LDHs) with $TiO_2$ synthesizes highly efficient sunlight-driven photocatalysts for degrading volatile organic pollutants such as toluene, methanol, and ethyl acetate.[283] The $TiO_2$-rGO/LDHs nanocomposite demonstrates superior photodegradation activity compared to pure $TiO_2$ and $TiO_2$-rGO samples. The enhanced performance is due to graphene's expanded light response range and inhibition of electron–hole pair recombination, while LDHs provide more hydroxide ions to accelerate oxidation reactions, resulting in increased radicals and improved pollutant degradation.

### 7.2 Photocatalytic water splitting for hydrogen production

Fossil fuel combustion is a primary contributor to greenhouse gas emissions and climate pollutants, causing climate change. The urgent need to transition to zero-emission energy sources drives the quest for alternatives to fossil fuels. Hydrogen emerges as a promising candidate, serving as a versatile and clean energy carrier. Through photocatalytic water splitting, hydrogen production becomes feasible using only water and solar light. This process initiates through photoelectric conversion within a semiconducting material, analogous to photovoltaic power generation. Unlike photovoltaic cells requiring external electrocatalysts,[284] photocatalytic systems integrate both photoelectric conversion and catalytic functions within a single particle or composite. This integration allows for the direct conversion of solar energy into chemical energy, enabling the splitting of water molecules into hydrogen and oxygen without the need for additional components.[14,285]

Water splitting is an uphill reaction, requiring an external energy input of at least 1.23 V to overcome the thermodynamic barrier associated with breaking the O–H bonds in water molecules and generating hydrogen and oxygen. Photocatalytic process aiming at water splitting is required to provide this minimum energy input to drive the reaction forward. $TiO_2$ stands as the predominant semiconductor in photocatalytic water splitting. The combination of light absorption, charge separation, and surface redox reactions enables the photocatalytic generation of hydrogen from water using $TiO_2$ as the catalyst. When $TiO_2$ photocatalyst is exposed to light, at the catalyst surface, the photo-generated electrons react with water molecules, reducing them to hydrogen ions ($H^+$). Simultaneously, the holes react with water molecules, oxidizing them to oxygen gas ($O_2$) or hydroxyl radicals ($^{\bullet}OH$). The accumulated $H^+$ from the reduction reaction combine with the electrons at the catalyst surface, forming hydrogen gas ($H_2$). Finally, the products of the redox reactions are desorbed from the catalyst surface, completing the catalytic cycle (Fig. 6A). Backus *et al.* studied the photocatalytic water dissociation at the $TiO_2$–water interface with bulk water, revealing that the process begins with hole-assisted deprotonation of near-surface water molecules and the attachment of hydroxyl groups to the surface.[286] These interfacial processes follow a biexponential model with time constants of 3 and 16 picoseconds. Understanding these timescales is crucial for optimizing the photocatalytic system by enhancing the desired reaction pathway and mitigating competing processes.

All three polymorphs of $TiO_2$ (anatase, rutile, brookite) have been studied for their photocatalytic activity. Anatase and rutile are often considered for this application while brookite $TiO_2$ is less common in this context, with their photocatalytic potential less explored compared to other two. The photocatalytic performance of heterophase junction structures combining anatase and rutile $TiO_2$ has garnered attention due to the distinct band gaps and aligned band-edge positions of these two phases. This configuration facilitates improved separation of photogenerated electron–hole pairs when exposed to solar light irradiation. The differing band gaps and matched band-edge positions create favorable conditions for efficient charge transfer across the heterojunction interface, enhancing the overall photocatalytic activity. As a result, these heterophase junction structures hold significant promise for applications in solar-driven photocatalysis, offering enhanced efficiency and performance compared to individual phases of $TiO_2$.[287,288]

Combining a hydrogenation treatment with heterophase junctions further enhances their performance by introducing a disordered layer with oxygen vacancies and $Ti^{3+}$ ions. This augmentation improves optical absorption, electrical conductivity, carrier transport, and separation efficiency. For instance, Hu *et al.* engineered a $TiO_2$ photoelectrode composed of rutile $TiO_2$ nanorods and anatase $TiO_2$ branches with hydrogenated heterophase interfaces through hydrothermal synthesis, hydrogenation, and branching growth processes.[289] The resulting structure exhibited anatase crystallographic planes in the $TiO_2$ branches, along with a disordered layer within the heterophase interface. This optimized photoelectrode significantly enhanced the hydrogen evolution rate for photoelectrochemical water splitting, achieving a rate 20 times higher than that of unhydrogenated $TiO_2$ nanorod arrays. Particularly, the hydrogenated interfaces between anatase branches and rutile nanorods play a crucial role by introducing oxygen vacancies and $Ti^{3+}$ species. These modifications create new energy levels associated with oxygen vacancies and Ti–OH groups, situated below the band edge positions of the CB and VB of rutile $TiO_2$

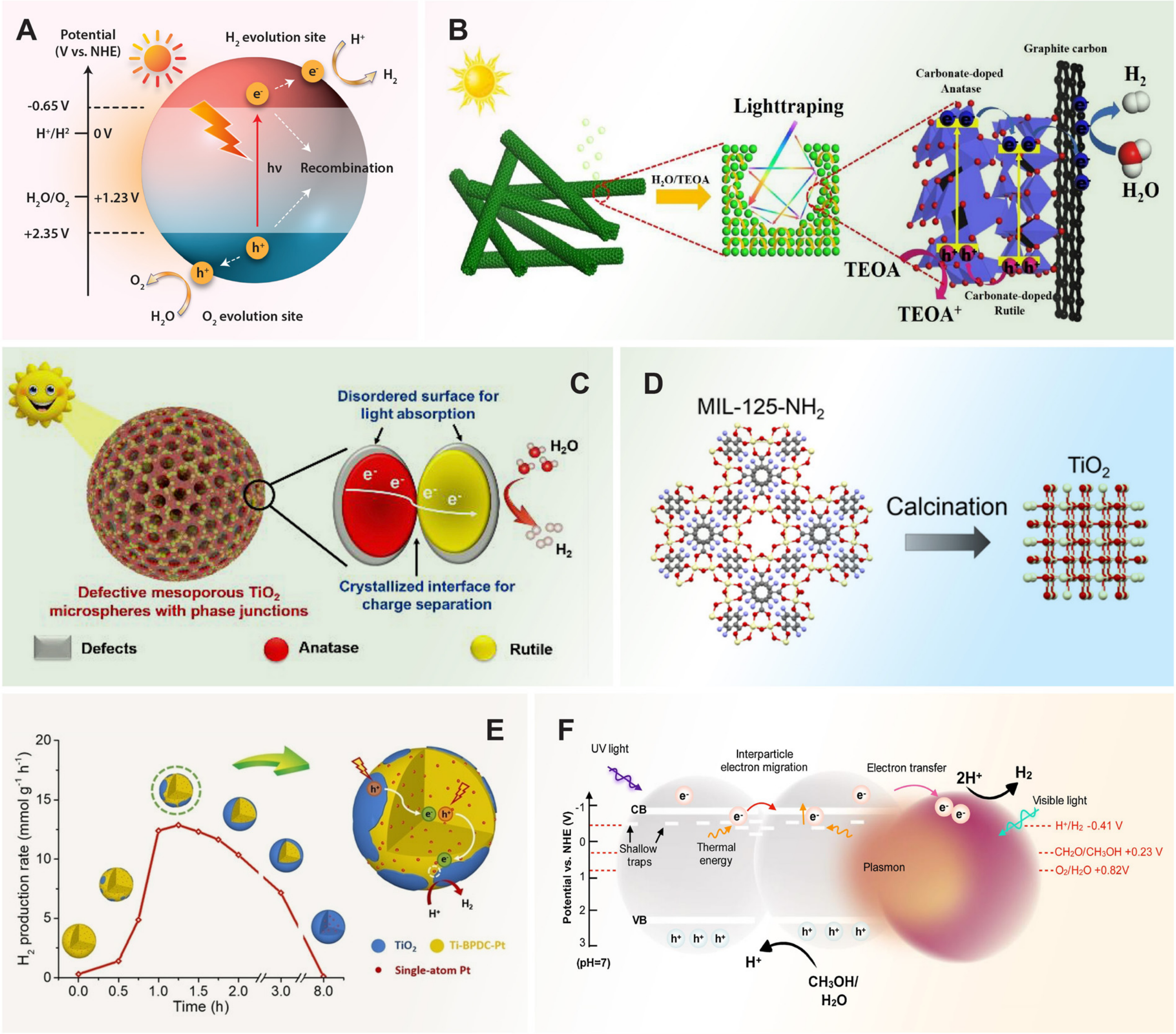

**Fig. 6** (A) Schematic illustration of the photocatalytic water splitting mechanism of $TiO_2$ semiconductor. (B) Photocatalytic hydrogen evolution mechanism of mesoporous carbonate-doped phase-junction $TiO_2$ nanotubes. Reproduced with permission from ref. 290. Copyright 2018, Elsevier. (C) Defective mesoporous $TiO_2$ microspheres with phase junctions for visible-light driven water splitting. Reproduced with permission from ref. 189. Copyright 2019, Elsevier. (D) Preparation of MIL-125-$NH_2$-derived $TiO_2$. Reproduced with permission from ref. 294. Copyright 2018, American Chemical Society. (E) The progress of hydrogen evolution reaction activities with phase composition of $TiO_2$/Ti-BPDC-Pt, finely tuned by varying pyrolysis duration. Reproduced with permission from ref. 295. Copyright 2023, Wiley-VCH. (F) Schematic illustration of the electron migration process in metal-containing $TiO_2$ aerogel monoliths for the photocatalytic hydrogen evolution reaction. Reproduced with permission from ref. 222. Copyright 2020, Elsevier.

nanorods, respectively. The alignment of these energy levels with those of anatase branches and hydrogenated rutile nanorods mitigates the recombination of photogenerated carriers, thereby enhancing the overall photoelectrochemical (PEC) performance. This improved carrier separation and reduced recombination contribute to the enhanced efficiency of the heterophase junction structure in facilitating photocatalytic water splitting.

By leveraging morphology, electronic, crystal, and textural structures, electrospun mesoporous carbonate-doped phase-junction $TiO_2$ nanotubes demonstrated exceptional photocatalytic hydrogen evolution activity, achieving 6108 μmol $h^{-1}$ $g^{-1}$, which is nearly 6 times higher than that of commercially available P25. The porous nanotube architecture extended the optical path through multiple reflections, enhancing light harvesting efficiency. Carbon doping reduced the bandgap of $TiO_2$, significantly enhancing visible light photocatalytic activity. Moreover, the phase junction interface improved charge separation and transfer, resulting in photocurrent densities 2 and 18 times higher than those of pristine anatase and rutile phase samples, respectively (Fig. 6B).[290] These synergistic effects led to the exceptional photocatalytic performance of the electrospun mesoporous carbonate-doped phase-junction $TiO_2$ nanotubes. Apart from 1D $TiO_2$ nanostructures with phase junctions and porous structures, $TiO_2$ hollow spheres have been widely investigated in the field of photocatalytic water splitting due to their unique structural characteristics and enhanced light harvesting capabilities.[291] The $TiO_2$ spheres composed of a crystalline core and an amorphous shell structured nanocrystallites, exhibited a hydrogen production rate of 0.182 mmol $g^{-1}$ $h^{-1}$, which was twice that of pristine $TiO_2$.[292]

Zhang *et al.* engineered defective mesoporous $TiO_2$ microspheres with phase junctions featuring controllable defect locations using a confinement reduction method.[189] This method exploits on the confinement decomposition effect, which allows for efficient defect production under mild conditions without compromising the mesostructures and phase junctions of the pristine mesoporous microspheres. Furthermore, by adjusting the reduction temperature, defects can be relocated from the nanocrystalline-exposed surfaces to the phase junction interfaces, enabling precise tuning of defect locations (Fig. 6C). The defect formation altered the energy band structure and mediated the visible light adsorption of the $TiO_2$ microspheres. The well-retained phase junction structure facilitated effective photo-induced charge separation. This engineered photocatalyst exhibited a hydrogen production rate of 42.6 μmol $h^{-1}$ (based on 50 mg of catalyst) under visible-light irradiation ($\lambda$ > 400 nm). Moreover, the apparent quantum efficiencies were measured at 12.7% and 2.8% at wavelengths of 420 nm and 520 nm, respectively.

In the realm of MOFs, several studies have explored the combination of $TiO_2$ with MOFs to enhance the efficiency of photocatalytic systems for hydrogen evolution reaction under visible light irradiation.[293] The 3D porous structure of $Ti^{IV}$-based MOFs provides a structured environment for the controlled growth and arrangement of $TiO_2$ crystals. Specifically, the templating effect of MIL-125-$NH_2$ enables the formation of well-defined $TiO_2$ nanoparticles with customized size, morphology, and crystallinity, leading to optimized photocatalytic performance. Studies have demonstrated that starting with MIL-125-$NH_2$ as a MOF precursor, $TiO_2$ particles can be synthesized at various temperatures while retaining the well-defined crystal shape of the parent MOF and controlled phase composition (Fig. 6D).[294] For instance, a mixed $TiO_2$ phase comprising 66% anatase and 34% rutile exhibited a remarkable hydrogen evolution rate of 1394 μmol $g^{-1}$ $h^{-1}$, surpassing both commercial Degussa P25 $TiO_2$ and conventionally synthesized $TiH_4O_4$- and MIL-167-derived $TiO_2$. This superior performance is credited to the unique templating effect of MIL-125-$NH_2$, which promotes the formation of nanosized anatase and rutile nanoparticles in effective contact, thereby enhancing electron–hole separation and overall photocatalytic efficiency.

A recently developed $TiO_2$/Ti-BPDC-Pt photocatalyst, featuring a $TiO_2$/Ti-MOF heterojunction with high-density Pt single-atomic co-catalysts, has shown promise for photocatalytic hydrogen evolution (Fig. 6E).[295] Single-atom co-catalysts have emerged as an efficient and cost-effective approach in heterogeneous photocatalysis due to their high atomic utilization efficiency and excellent catalytic activity. These isolated metal heteroatoms can enhance semiconductor band structures, improving light absorption and facilitating electron collection to boost surface charge separation and transfer.[296,297] In this study, a $TiO_2$/Ti-BPDC heterojunction is tailored through a surface pyrolytic reconstruction approach, resulting in an intimate interface between $TiO_2$ and the Ti-based MOF, which facilitates efficient charge separation and migration. The strategic placement of Pt within the electron-enriched domain of the heterojunction further enhances the utilization of separated electrons for the reduction of protons, thus promoting hydrogen production. This engineered $TiO_2$/Ti-BPDC-Pt catalyst exhibits superior activity, achieving a hydrogen evolution rate of 12.4 mmol $g^{-1}$ $h^{-1}$, surpassing other $TiO_2$- or MOF-based catalysts.

Among the Pt-group metals, Ru stands out as a competitive alternative to Pt due to its cost-effectiveness and comparable hydrogen evolution performance.[298] The coexistence of two forms of Ru species such as nanoparticles and single atoms, supported on MOF-derived N-doped $TiO_2$/C hybrids exhibits superior photocatalytic hydrogen evolution reaction.[299] This enhanced performance results from the synergistic coupling of Ru nanoparticles and Ru single atoms. Similarly, atomically dispersed Ru atoms on multi-edged $TiO_2$ spheres significantly enhance hydrogen evolution by effectively transferring photogenerated electrons to isolated Ru atoms and facilitating charge separation and transport through the multi-edged $TiO_2$ structure.[53] The *in situ* X-ray absorption fine structure technique was used to examine the dynamic changes of isolated sites during the catalytic process. Upon light irradiation, the Ru species experience gradual changes in valence and configuration, facilitating the photo-splitting of water into solar fuels.

When $Ti_3C_2$ MXene was converted into 3D porous frameworks of $Ti_3C_2$–$TiO_2$ nanoflowers, the *in situ* growth of $TiO_2$ on the surface of $Ti_3C_2$ offers intimate interaction between $TiO_2$ and $Ti_3C_2$ for photocatalytic overall water splitting.[208] The photogenerated electrons can transfer from the CB of $TiO_2$ to $Ti_3C_2$, where $Ti_3C_2$ serving as an electron sink. The formation of a possible Schottky junction at the interface between $Ti_3C_2$ and $TiO_2$ enhances the separation of photogenerated charge carriers, effectively suppressing recombination. As a result, more electrons participate in the photoreduction process for hydrogen evolution, while more holes engage in the photooxidation process for oxygen evolution. This mechanism contributes to the enhanced efficiency of photocatalytic water splitting facilitated by $Ti_3C_2$–$TiO_2$ nanoflowers.

$TiO_2$ aerogel monoliths hold significant promise as efficient and sustainable photocatalysts for hydrogen generation due to the synergetic effect between their building blocks and their 3D macroscopic structure. The porous structure of $TiO_2$ aerogels promotes light trapping and diffusion within the monolith. Upon light entering the aerogel, it undergoes multiple scattering events, resulting to prolonged interaction lengths and increased absorption probabilities. This improves the efficiency of light harvesting by ensuring that a larger fraction of incident photons is absorbed by the $TiO_2$ matrix. Likewise, the interconnected pores and tortuous pathways within the aerogel matrix enable light to travel over millimeter length scales through the monolith, hence increasing the probability of photon absorption by $TiO_2$ nanoparticles.[222] To preserve the fragile structure of the 3D $TiO_2$ network while enabling it sensitive to visible light, monolithic aerogels composed Pd modified $TiO_2$ nanoparticle was doped with nitrogen in a gas-phase nitridation process using plasma-enhanced chemical vapor deposition at low temperature.[300] The nitridation-induced nitrogen doping and defect engineering in $TiO_2$ aerogels, coupled with Pd nanoparticle loading achieved the desired enhancement in optical absorption and charge separation efficiency, and hence outperformed the undoped material in visible light-driven photocatalysis for hydrogen production.

Besides doping, the assembly of non-doped $TiO_2$ aerogel composite with noble metal nanoparticles (Au, Pd, PdAu) has been shown to exhibit superior visible light-induced photocatalytic hydrogen production compared to their corresponding powders.[222] By leveraging the plasmonic properties of noble metal nanoparticles and the catalytic activity of $TiO_2$, the formation of inter-particle contacts during nanoparticle assembly lead to the creation of shallow traps within the composite material, resulting to an absorption band around 400–500 nm in the visible range of the electromagnetic spectrum. The combination of shallow traps absorption in the visible range and the LSPR of the metal nanoparticles promoted the hydrogen evolution through the near-field electromagnetic mechanism. Further, thermal energy generated by the LSPR of the plasmonic particles promotes the shallow-trap electron migration process (Fig. 6F). Overall, the observed 3.5 times increase in hydrogen generation underlines the importance of the both the aerogel 3D structure and the type of metal nanoparticle on the photocatalytic activity of the aerogels in enabling light-harvesting and efficient mass transport of reactants to the surface-active sites.

Among the noble metal nanoparticles, Pd has been recognized as a particularly effective photocatalyst under visible light irradiation. One of the key reasons for the high photocatalytic activity of Pd is attributed to the generation of hot electrons from its 4d orbital under visible light irradiation.[301] By using a microwave-assisted non-aqueous sol–gel method, Pd-modified $TiO_2$ nanoparticles can be synthesized with simultaneous incorporation of Pd ions in the $TiO_2$ lattice and formation of Pd metal nanoparticles on the surface of the $TiO_2$ nanoparticles.[302] The subsequent assembly of Pd-modified $TiO_2$ nanoparticles into macroscopic aerogels results in photocatalyst with a narrow band gap, primarily due to the formation of Pd 4d energy levels, oxygen vacancies, and $Ti^{3+}$ centers within the $TiO_2$ lattice. While Pd doping and Pd nanoparticle loading can enhance visible-light absorption in $TiO_2$ aerogels, excessive Pd accumulation may hinder charge generation and separation due to shadowing effects and high Schottky barriers.

### 7.3 Chemical transformations of $CO_2$ for sustainable future

Carbon dioxide ($CO_2$) emissions are the primary driver of global warming and climate change. Limiting global warming to 1.5 °C requires rapid and sustained reductions in $CO_2$ emissions and reaching net-zero emissions in the energy sector by 2050.[303] To mitigate this crisis, turning $CO_2$ into valuable chemicals or fuels has the potential to mitigate global warming by treating hundreds of millions of tons of $CO_2$ annually. Among various $CO_2$ conversion approaches, photocatalytic $CO_2$ reductions is regarded as one of the most ideal approaches by mimicking natural photosynthesis. Generally, $CO_2$ can be photocatalytically reduced into several carbonaceous molecules including CO, HCOOH, HCHO, $CH_3OH$, and $CH_4$ (Fig. 7A). In this regard, numerous visible-light-driven photocatalysts for the $CO_2$ conversion have been developed, particularly to optimize the structure and composition of semiconductor photocatalysts to improve their visible light absorption and charge separation efficiency, *e.g.*, creating heterojunctions, forming surface defects, incorporating metal co-catalysts, and engineering exposed crystal facets *etc*.[16,48,216,304–307]

Recently, a $TiO_2$ catalyst was engineered by anchoring single Ag atoms onto the surface of the anatase $TiO_2$ nanoparticles for photocatalytic $CO_2$ to $CH_4$ conversion. The Ag/$TiO_2$ catalyst exhibited photochromism which was attributed to the trapping of photogenerated electrons.[308] The resulting active state of the photochromic catalyst effectively facilitates the separation and migration of photogenerated charge carriers. In addition, the isolated Ag atoms and adjacent Ti sites play complementary roles in catalyzing the conversion of $CO_2$ to $CH_4$. The isolated Ag atoms serve to stabilize two key intermediates (*CO and *CHO) formed during the reaction process, while the adjacent Ti sites are responsible for activating water molecules to generate more protons, hence both simultaneously affording active sites to increase the production of $CH_4$ rather than CO (Fig. 7B). Ultimately, the Ag/$TiO_2$ catalyst achieved high activity and selectivity of 46.0 mmol $g^{-1}$ $h^{-1}$ and 91% respectively, for photocatalytic $CO_2$ methanation.

Besides Ag atoms, Cu single atoms and Au–Cu alloy nanoparticles were co-loaded on $TiO_2$ by photodeposition for the photocatalytic production of solar fuels from $CO_2$ and $H_2O$.[312] The optimized photocatalyst achieved high formation rates of 3578.9 μmol $g^{-1}$ $h^{-1}$ for $CH_4$ and 369.8 μmol $g^{-1}$ $h^{-1}$ for $C_2H_4$. The synergy between Cu single atoms and Au–Cu alloy nanoparticles enhanced the adsorption and activation of $CO_2$ and $H_2O$ and lowered the activation energy barrier for $CH_4$ and $C_2H_4$ formation, enabling highly efficient and stable production of these solar fuels.

Typically, the scope of $CO_2$ conversion work is often limited to the low adsorption of $CO_2$ on the surface of photocatalysts owing to the low specific surface area and the lack of matched pores. The efficiency of $CO_2$ conversion heavily relies on the availability of $CO_2$ molecules near the active sites of the photocatalyst, where they can interact with photoexcited electrons and participate in catalytic reactions. Facing this challenge, combining a $CO_2$ capture material with semiconductor photo-

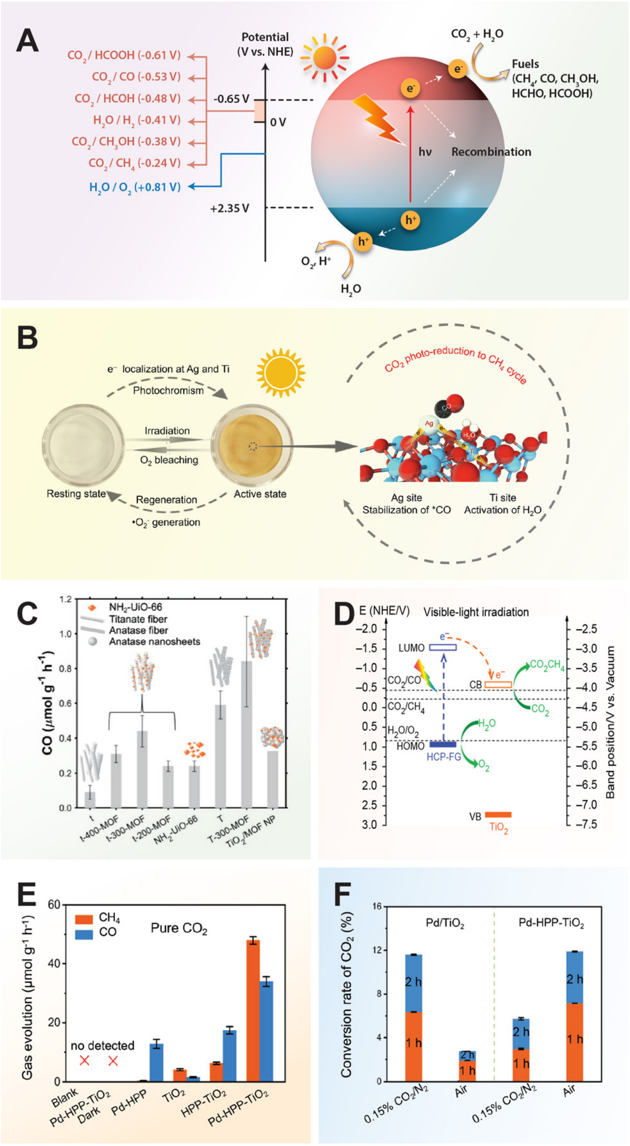

Fig. 7 (A) Schematic illustration of the $CO_2$ photoreduction mechanism of $TiO_2$ semiconductor. (B) Photochromic cycle of Ag/$TiO_2$ (left) and the photocatalytic $CO_2$ to $CH_4$ conversion cycle over the Ag–Ti active site on Ag/$TiO_2$ (right). Reproduced with permission from ref. 308. Copyright 2024, Royal Society of Chemistry. (C) Photocatalytic CO evolution rates of $TiO_2$/$NH_2$-UiO-66 nanocomposite compared to titanate fiber. Reproduced with permission from ref. 309. Copyright 2019, Wiley-VCH. (D) Proposed mechanism of charge separation and transfer within the $TiO_2$/graphene composite under visible-light ($\lambda \geq 420$ nm) irradiation. Reproduced with permission from ref. 310. Copyright 2019, Springer Nature Group. (E) The evolution rates of $CH_4$ and CO in photocatalytic $CO_2$ reduction and (F) comparison of the conversion yield of $CO_2$ in Pd/$TiO_2$ and Pd-HPP-$TiO_2$. Reproduced with permission from ref. 311. Copyright 2022, Springer Nature Group.

catalysts has been proposed to provide an attractive means for increasing $CO_2$ conversion efficiency. Xu *et al.* designed photocathode comprised of a layered hybrid heterojunction of $TiO_2$ on 2D $Ti_3C_2$ MXene nanosheets, functionalized with imine ligands and Pd nanoparticles (Pd/N-$TiO_2$/$Ti_3C_2$) for $CO_2$ conversion.[313] The photocathode of Pd/N-$TiO_2$/$Ti_3C_2$ exhibited an evolution rate of total hydrocarbon (formate, methanol, ethanol) 5-fold higher than that of Pd-$Ti_3C_2$ photocathode. The electrode was stable for 16 hours without a change in its efficiency. The high efficiency of Pd/N-$TiO_2$/$Ti_3C_2$ is ascribed to the high surface area and narrow band gap (2.1 eV) $TiO_2$/$Ti_3C_2$ heterojunction materials which provide abundant active sites in favor of the adsorption of $CO_2$ molecules and promote strong visible light absorption, respectively as well as the plasmonic resonance effect of Pd nanoparticles. Kreft *et al.* synthesized Cu/$TiO_2$-aerogel composite featuring Cu(II)-nanoparticles on the surface of a highly porous $TiO_2$ aerogel for aqueous $CO_2$ reduction to CO without the need for external sacrificial reagents.[314] Notably, the presence of $O_2$ in the reaction environment enhances CO productivity while suppressing $H_2$ generation.

Combining $TiO_2$ photocatalyst with MOFs allows for the synergy between the light-absorption and electron-generation capabilities of $TiO_2$ with a high concentration of open active sites in the framework of MOFs for $CO_2$ capture and conversion processes.[315,316] In addition, optimizing the morphology of the heterojunction components and engineering the interface between the two materials are critical for achieving a close interaction and maximizing photocatalytic performance. This can involve controlling the size, shape, and distribution of $TiO_2$ nanoparticles on the MOF surface. Studies have shown that improved $CO_2$ photoreduction was achieved through synthesizing $TiO_2$ nanoparticles onto various preformed MOFs, producing $TiO_2$/HKUST-1,[317] $TiO_2$/Co-ZIF-9,[318] and $TiO_2$/$NH_2$-UiO-66 composites.[211] The superior photocatalytic activity is ascribed to the development of an intimate interaction between $TiO_2$ and MOFs forming a heterojunction, while retaining the high $CO_2$ uptake and porosity of MOFs. The $TiO_2$/MOF composites exhibited better durability and significantly more efficient in reducing $CO_2$ to CO compared to their individual components. Crake *et al.* synthesized $TiO_2$/$NH_2$-UiO-66 nanocomposites with superior photocatalytic activity in $CO_2$ photoreduction, specifically focusing on the role of heterojunctions, highlights the importance of both crystalline phase and morphology control in enhancing charge transfer and overall photocatalytic performance.[309] Forming anatase phase nanofibers and growing MOF particles on their surface allows for precise control of composite morphology, which in turn maximizes charge transfer efficiency. Accordingly, the electrons transfer from $TiO_2$ into the MOF and holes from the MOF into $TiO_2$, accompanied by strong band bending in $TiO_2$ induced by the MOF, leading to an improved charge separation and facilitating efficient charge transfer in the heterojunction structure. Therefore, the $TiO_2$/$NH_2$-UiO-66 nanocomposite produced 9 times more CO when compared to titanate under UV-vis light irradiation, confirming the synergistic effect of forming a composite (Fig. 7C).

Wang *et al.* incorporated $TiO_2$ units within the pores of a chromium terephthalate-based MOF (MIL-101) and its derivatives, forming “molecular compartments” where photocatalytic reactions can occur in a confined environment.[319] These compartments facilitate the close proximity of $TiO_2$ units and catalytic metal clusters, promoting efficient charge transfer and catalytic activity for $CO_2$ reduction. The observed apparent quantum efficiency for $CO_2$ photoreduction of 11.3% at 350 nm in the composite consisting of 42% $TiO_2$ in a MIL-101 derivative (42%-$TiO_2$-in-MIL-101-Cr-$NO_2$) demonstrates the effectiveness of this composite for photocatalytic $CO_2$ conversion. Furthermore, $TiO_2$ units in one type of compartment in this composite are 44-fold more active than those in the other type, emphasizing the importance of precise positioning of $TiO_2$ within the composite. Simultaneously, the photocatalytic process generates molecular oxygen as a byproduct, contributing to the overall sustainability of the $CO_2$ conversion process.

Wang *et al.* developed a porous composite structure by integrating anatase $TiO_2$ crystals with reactive (001) facets on graphene surface and subsequently encapsulated in hypercrosslinked polymer layers by *in situ* knitting strategy.[310] Given abundant adsorptive sites of the porous capture materials for efficient $CO_2$ uptake, the photoreduction of $CO_2$ of modified $TiO_2$ photocatalyst proceeded under modest conditions without sacrificial reagents and co-catalysts, yielding 27.62 $\mu mol\ g^{-1}\ h^{-1}$ for $CH_4$ production under visible-light irradiation. In comparison, the $CO_2$ conversion products were hardly identified over commercial $TiO_2$ (P25), and pristine $TiO_2$ with reactive (001) facets because of their weak visible light-responsive ability.

With the highest occupied molecular orbital (HOMO) and lowest unoccupied molecular orbital (LUMO) energy levels lying more negative than the VB and CB levels of $TiO_2$, respectively, the hypercrosslinked polymer-graphene can act both as $CO_2$ adsorbent and photosensitizer, in which their photo-induced electron–hole pairs are migrated and separated at the interface with $TiO_2$ *via* their interfacial interaction. Therefore, the $CO_2$ reduction is prone to happen at the catalytic sites on $TiO_2$ instead on hypercrosslinked polymer-graphene, giving rise to better $CO_2$ conversion efficiency (Fig. 7D). Moreover, a selectivity of 83.7% for $CH_4$ production is achieved during the photocatalytic reaction, suggesting negligible side reaction of hydrogen evolution under visible-light irradiation.

Recently, Ma *et al.* reported a novel approach for the preparation of a composite photocatalyst by hyper-crosslinking porphyrin-based polymers (HPP) on the surface of hollow $TiO_2$, followed by coordination with Pd(II).[311] In a pure $CO_2$ environment, this composite photocatalyst, Pd-HPP $TiO_2$ exhibited remarkable $CO_2$ reduction efficiency, achieving high evolution rates of 48.0 and 34.0 $\mu mol\ g^{-1}\ h^{-1}$ for $CH_4$ and CO, respectively (Fig. 7E). In the presence of 5 vol% $O_2$, the $CO_2$ reduction over a catalyst without hyper-crosslinked porphyrin-based polymer (Pd/$TiO_2$) drastically decreases to only 6% of that observed in pure $CO_2$. On the other hand, the inhibition from $O_2$ is significantly mitigated over composite photocatalyst (Pd-HPP $TiO_2$), which maintains 46% of the $CH_4$ evolution rate observed in pure $CO_2$ conditions. The composite photocatalyst, Pd-HPP-$TiO_2$ demonstrated notable photocatalytic activity even in the presence of air, with a $CO_2$ conversion yield of 12% and $CH_4$ production of 24.3 $\mu mol\ g^{-1}$ after 2 hours of UV-visible light irradiation (Fig. 6F). This performance is 4.5 times higher than that observed over Pd/$TiO_2$. The hyper-crosslinked porphyrin-based polymer layer effectively enriches $CO_2$ at Pd(II) sites, thereby mitigating the reduction of $O_2$. Moreover, water adsorbed on $TiO_2$ undergoes oxidation by the holes present in the valence band of $TiO_2$. This process serves to reduce charge recombination, thereby enhancing $CO_2$ conversion efficiency.

Bian *et al.* developed a cascade Z-Scheme photocatalytic system using 2D g-$C_3N_4$ for the reduction half-reaction and 2D $BiVO_4$ nanosheets for the oxidation half-reaction, combined with an energy platform of (001)$TiO_2$.[320] This (001)$TiO_2$-*g*-$C_3N_4$/$BiVO_4$ nanosheet heterojunction exhibited exceptional photocatalytic activity for $CO_2$ photoreduction and water splitting without cocatalysts, achieving a 19-fold improvement in photoactivity for $CO_2$ reduction to CO under visible-light irradiation compared to $BiVO_4$. This performance surpasses other reported Z-Scheme systems, even those using noble metals as mediators.

### 7.4. Nitrogen fixation for ammonia production

Since the initial discovery in 1977 that nitrogen ($N_2$) could be reduced to ammonia ($NH_3$) on the surface of $TiO_2$,[321] the pursuit of achieving $N_2$ fixation using sunlight has become a significant research focus. $N_2$ fixation is the conversion of atmospheric $N_2$ into $NH_3$ or other $N_2$-containing compounds, which is an essential process for the production of fertilizers and various industrial applications.[322] As is known, $N_2$ is a highly stable compound with a bond dissociation energy of $N\equiv N$ of approximately 941 $kJ\ mol^{-1}$, making it thermodynamically challenging to convert it into $NH_3$ or other N-containing compounds. The Haber–Bosch process, which is the most widely used method for industrial $NH_3$ production, achieves the industrial-scale $NH_3$ synthesis through high temperatures (300–500 °C) and pressures (200–300 atm), which leads to huge energy consumption and high $CO_2$ emission.[323] Therefore, a less energy consuming alternative would be highly desirable.

Photocatalytic conversion of $N_2$ to $NH_3$ is a green alternative for the Haber–Bosch process. It typically involves using light energy to generate electrons and holes within a semiconductor and combine with water protons to reduce $N_2$ to $NH_3$ (Fig. 8A).[17,324] The current strategies for developing efficient $TiO_2$ photocatalysts for $N_2$ fixation prioritize the creation of active sites through the introduction of defects in $TiO_2$. These defects, such as oxygen vacancies, aim to weaken the $N\equiv N$ triple bond of adsorbed $N_2$ molecules by facilitating the transfer of electrons into the antibonding orbital of $N_2$. This activation process enables their subsequent reaction with photogenerated electrons for $N_2$ reduction reactions. In addition, defects in the $TiO_2$ structure enable efficient charge separation and accelerate charge carrier transfer from photocatalysts to the adsorbed reactants.[18] It was demonstrated that by fine-tuning the concentration of oxygen vacancies, $TiO_2$ can achieve a 3-fold increase in charge separation efficiency compared to pristine $TiO_2$.[325] The oxygen vacancy defect structures coordinate both the charge separation efficiency and the disso-

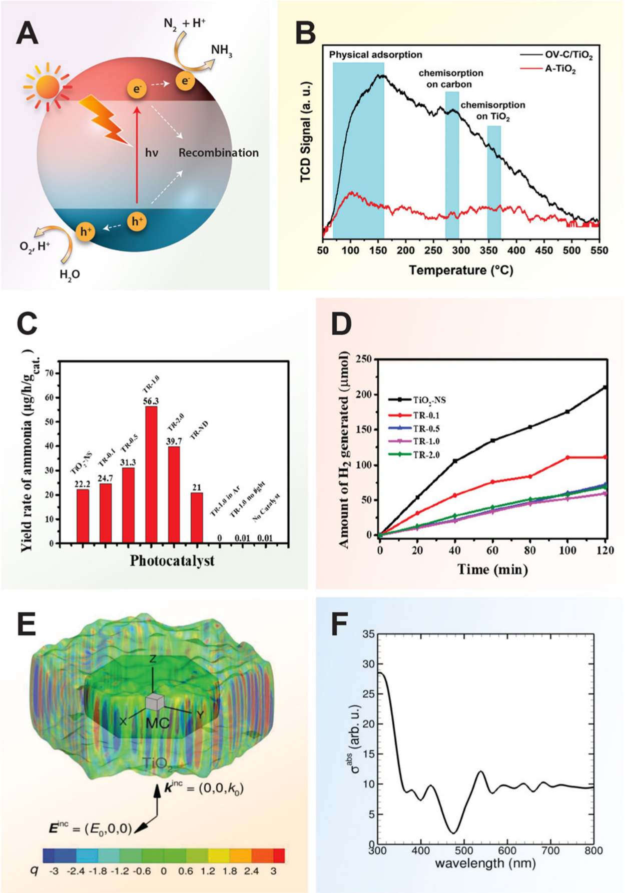

**Fig. 8** (A) Schematic illustration of the $N_2$ photoreduction mechanism of $TiO_2$ semiconductor. (B) $N_2$-temperature programmed desorption profiles of the commercial anatase $TiO_2$ and oxygen vacancy-rich C-$TiO_2$. Reproduced with permission from ref. 326. Copyright 2022, Wiley-VCH. (C) The yield rate of photocatalytic fixation of $N_2$ to $NH_3$ and (D) the quantity of $H_2$ generated in water by single Ru atom decorated $TiO_2$ nanosheet photocatalysts. Reproduced with permission from ref. 328. Copyright 2019, American Chemical Society. (E) Surface charge distribution of a carbon coated hexagonal $Mo_2C$ and $TiO_2$ particle with core–shell structure under the illumination of sunlight and (F) corresponding absorption cross sections across the spectrum of sunlight. Reproduced with permission from ref. 329. Copyright 2023, Elsevier.

ciative adsorption capacity of $N_2$, leading to a normalized $N_2$ photofixation rates of 324.86 mmol $g^{-1}$ $h^{-1}$ (under full spectrum illumination), with corresponding apparent quantum yields of 1.1% under 365 nm illumination.

The oxygen-rich $TiO_2$, prepared by calcination of $Ti_3C_2$ MXene, exhibited superior photocatalytic $N_2$ fixation performance compared to both P25 and commercial anatase $TiO_2$.[326] Specifically, it achieved a $N_2$ fixation rate of 84 μmol $g^{-1}$ $h^{-1}$, utilizing $CH_3OH$ as the proton source. Typically, chemisorption of $N_2$ on carbon occurs at around 280 °C, while on $TiO_2$, it occurs at approximately 360 °C. In contrast, physical adsorption of $N_2$ takes place at a lower temperature of about 120 °C.[327] The significantly higher temperature programmed desorption signal observed for oxygen vacancy-rich C-$TiO_2$ compared to commercial anatase $TiO_2$ indicates stronger chemisorption of $N_2$ on the former (Fig. 8B). This enhanced chemisorption capability of oxygen vacancy-rich C-$TiO_2$ is crucial for the activation of $N_2$, highlighting its potential for efficient $N_2$ reduction in photocatalytic processes.

Controlling defects in $TiO_2$ nanotubes can be achieved through an amine-assisted remedying strategy using urea, dicyandiamide, and cyanamide as precursors.[330] This approach involves the preparation of hydrogen-treated $TiO_2$ nanotubes, which are engineered to possess oxygen vacancies. By using urea, dicyandiamide, or cyanamide as precursors, the process can be optimized to introduce and regulate the concentration of oxygen vacancies in the $TiO_2$ nanotubes. The resulting defect-rich nanotubes extended the visible light absorption and suppressed the recombination of photogenerated electron–hole pairs, which led to improved photocatalytic performance in $N_2$ fixation reactions. The $NH_3$ production rate, reaching 1.2 mmol $L^{-1}$ $h^{-1}$ under full spectrum light irradiation, represents a significant enhancement compared to pristine $TiO_2$, with an approximate 8.6-fold increase in efficiency.

While another effective way of increasing $NH_3$ production yield in photocatalytic $N_2$ fixation is through doping $TiO_2$ with metal heteroatoms.[52] Copper, as a dopant, can effectively regulate the concentration of oxygen vacancies and introduce substantial compressive strain in ultrathin $TiO_2$ nanosheets. Particularly, defect-rich $TiO_2$ nanosheets containing 6 mol% copper demonstrated stable performance for the photocatalytic reduction of $N_2$ to $NH_3$ in water, showcasing superior photoactivity even up to 700 nm. Modifications with oxygen vacancies and strain effects in $TiO_2$ nanosheets enable strong chemisorption and activation of molecular $N_2$ and water, leading to high rates of $NH_3$ evolution under visible-light irradiation. Analysis using diffuse reflectance infrared Fourier transformation spectroscopy provides compelling evidence that $N{\equiv}N$ triple bonds can be activated on the defect-rich $TiO_2$ nanosheets containing 6 mol% copper, forming $NH^{4+}$ species under light irradiation. The observed rates of $O_2$ (59.1 μmol $g^{-1}$ $h^{-1}$) and $NH_3$ (78.9 μmol $g^{-1}$ $h^{-1}$) evolution during the tests closely match the theoretical ratio of 3 : 4 for the reaction $N_2 + 3H_2O \rightarrow 2NH_3 + 1.5\ O_2$, with no detectable $N_2H_4$ byproduct observed. This suggests high selectivity and efficiency of the photocatalytic $N_2$ fixation process on the defect-rich $TiO_2$ nanosheets.

The recent development of single atom decorated $TiO_2$ semiconductor with engineered oxygen vacancies has demonstrated remarkable catalytic activity in photocatalytic $N_2$ fixation. Single atom metals dispersed on supports offer homogeneous catalytically active sites, a low-coordination environment for metal atoms, and maximum metal utilization efficiency, resulting in enhanced catalytic activity, stability, and selectivity across various processes.[53,328,331] The composite catalyst containing 1 wt% of Ru exhibited a significantly improved ammonia generation rate of 56.3 μg $g^{-1}$ $h^{-1}$, more than doubling that of pure $TiO_2$ nanosheets (Fig. 8C).[328] Upon decoration with Ru, the photocatalytic activity of $TiO_2$

nanosheets for the competing reaction, such as the hydrogen evolution reaction decreased. The hydrogen evolution activity was suppressed, reaching an almost saturated value of 30 μmol $h^{-1}$ at 0.5 wt% Ru, compared to 105.3 μmol $h^{-1}$ in pure $TiO_2$ nanosheets (Fig. 8D). This decrease in hydrogen evolution reaction activity with the introduction of Ru species is attributed to the interference with the transportation of photoelectrons from $TiO_2$ to $H^+$ by combining with the oxygen vacancies, thus inhibiting hydrogen evolution reaction.

In addition to metal doping, non-metal introduction into the $TiO_2$ lattice has been investigated as a strategy in modifying the electronic structure of $TiO_2$ and facilitating the separation of photogenerated charge carriers. Specifically, N-doping in $Ti_3C_2$–$TiO_2$ was found to enhance the carrier separation and improve the ammonia production yield to 415.6 μmol $g^{-1}$ $h^{-1}$, which represents an 8-fold increase compared to pure $TiO_2$.[32] Likewise, N-doping $TiO_2$ hollow microspheres along with the creation of oxygen vacancies displayed an ammonia yield of 80.09 μmol $g^{-1}$ $h^{-1}$.[114] This enhancement is associated with the synergistic effect between the N-doping, oxygen vacancies, and hollow microsphere structure that collectively contributes to the boosted efficiency of photocatalytic $N_2$ fixation. Firstly, the incorporation of nitrogen dopants narrows the bandgap of $TiO_2$ from 3.18 eV to 2.83 eV, leading to improved absorption of visible light. Further, the creation of oxygen vacancies assists to impede the recombination of photo-generated carriers, hence increasing the efficiency of charge separation. Besides, the hollow microspheres structure of the catalysts provides a large surface area and promotes light absorption and utilization. These findings highlight the potential of tailored nanostructures and dopants for enhancing the performance of photocatalysts in nitrogen fixation applications.

Recently, a composite material consisting of carbon coated hexagonal $Mo_2C$ and $TiO_2$ was developed for photocatalytic $N_2$ fixation.[329] In contrast to pure $TiO_2$, this composite photocatalyst effectively separates the photogenerated electrons and holes, facilitating the efficient conversion of atmospheric $N_2$ into $NH_3$ directly from air. The carbon-coated hexagonal photocatalyst demonstrated a remarkable enhancement in photocatalytic $N_2$ fixation performance, achieving a 16-fold increase compared to pure $TiO_2$ under room temperature and ambient pressure conditions. In the proposed heterojunction formed by $TiO_2$ and $Mo_2C$, an important aspect is the alignment of their conduction band potentials. Specifically, the conduction band potential of $Mo_2C$ is strategically positioned to facilitate the conversion of $N_2$ to $NH_3$. Relative to $TiO_2$, the conduction band potential of $Mo_2C$ is lower, thereby creating a favorable energy gradient that facilitates the transfer of photoelectrons from $TiO_2$ to $Mo_2C$. Moreover, the graphitized carbon layer structure enhances the concentration of photoelectrons on $Mo_2C$, owing to the highly conductive carbon layer. $N_2$ molecules readily adsorb onto the carbon vacancies of the molybdenum atoms, where they receive photoelectrons. Subsequently, the activated nitrogen species combine with protons in water, ultimately undergoing reduction to form ammonia. The hydroxyl radicals generated by photocatalytic water splitting of the catalyst, undergo oxidation by $TiO_2$ holes, leading to the formation of $O_2$. The validation from numerical simulations further supports the consistency between the trend of absorption cross-sections of the core–shell structured carbon-coated hexagonal $Mo_2C/TiO_2$ across the sunlight spectrum in simulations and the absorption measured in experiments (Fig. 8E and F). This agreement between simulation and experimental results provides confidence in the accuracy of the proposed model and supports further exploration of the material's photocatalytic properties and potential applications.[332]

### 7.5. Photocatalytic hydrogen peroxide production

Hydrogen peroxide ($H_2O_2$) is a potent oxidising agent that decomposes into water and oxygen. It is widely used in chemical manufacturing, paper making, textile bleaching and water treatment industries. Currently, $H_2O_2$ is primarily produced industrially through the anthraquinone oxidation, which is energy intensive process that generates large amounts of hazardous by-products.[333,334] One alternative method is *via* the direct synthesis from hydrogen gas and oxygen gas in the presence of noble metal or alloy catalysts but the inherent risk of explosions from the combustible hydrogen-oxygen mixture severely limits its use on a larger industrial scale.[335–337] A safer and greener method of $H_2O_2$ production is to utilise $TiO_2$ as a photocatalyst for reducing water and oxygen into $H_2O_2$. However, pristine $TiO_2$ has significant limitations, such as poor light absorption and low $H_2O_2$ yield, due to the combination of synthesized $H_2O_2$ with hydroxyl groups forming peroxide complexes that decompose $H_2O_2$.[337,338] To address these issues, various modification strategies have been employed in $TiO_2$-based photocatalytic systems to enhance $H_2O_2$ production.

For example, Gan *et al.* synthesized ultrathin $C_3N_5$ nanosheets and assembled them on oxygen-deficient $TiO_2$ arrays.[339] This coupling created a type-II heterojunction with an internal electric field to drive carrier separation and charge transfer, leading to efficient photocatalytic $H_2O_2$ production. The optimal heterojunction achieved the highest $H_2O_2$ formation rate of 2.93 μmol $L^{-1}$ $min^{-1}$ in a 90% water/10% ethanol mixture, which is about 4.1 times higher than that of the $TiO_{2-x}$ arrays. Similarly, a S-scheme heterojunction photocatalyst was created by coupling $TiO_2$ with three-dimensionally ordered macroporous sulfur-doped graphitic carbon nitride using electrostatic self-assembly.[340] This photocatalyst achieved high photocatalytic $H_2O_2$ production activity, yielding 2128 μmol $h^{-1}$ $g^{-1}$ without the need for hole scavengers.

Another composite material uses Au and MXene as co-catalysts to explore the relationship between the photocatalytic activity of the brookite $TiO_2$/Au/MXene composite under UV light for the formation of hydrogen peroxide.[341] This combination effectively improved the electron–hole pair separation and charge transfer rate of brookite $TiO_2$. Under UV light exposure, brookite $TiO_2$ forms electron–hole pairs, with electrons transferring to the conduction bands of Au and MXene. Concurrently, holes oxidize 2-propanol to create protons, while electrons react with $O_2$ to form superoxide anion radicals, ultimately producing $H_2O_2$. The composite with 0.4% gold and

15% MXene content was optimal, generating 6.80 mg $L^{-1}$ $H_2O_2$ at pH 3 after 4 hours of UV photo-irradiation. This $H_2O_2$ production was 10 times greater than that of brookite $TiO_2$ alone.

Hu *et al.* synthesized a 2D/1D hierarchical layered $ZnIn_2S_4$ modified $TiO_2$ photocatalyst for $H_2O_2$ production, which was rapidly activated into hydroxyl radicals for wastewater purification in a Fenton-like cascade reaction.[19] This process is driven by a Z-scheme heterojunction mechanism, where photoexcited electrons from $TiO_2$ recombine with holes from $ZnIn_2S_4$, leading to the reduction of $O_2$ to $H_2O_2$. The $ZnIn_2S_4/TiO_2$ catalyst achieved an $H_2O_2$ evolution rate of 1530.59 μmol $g^{-1}$ $h^{-1}$ with a 10.39% external quantum efficiency under 400 nm irradiation. The produced $H_2O_2$ was activated by unsaturated sulfur atoms in $ZnIn_2S_4$, degrading 90% of tetracycline antibiotics (50 ppm) in wastewater within 1 hour (Fig. 9A).

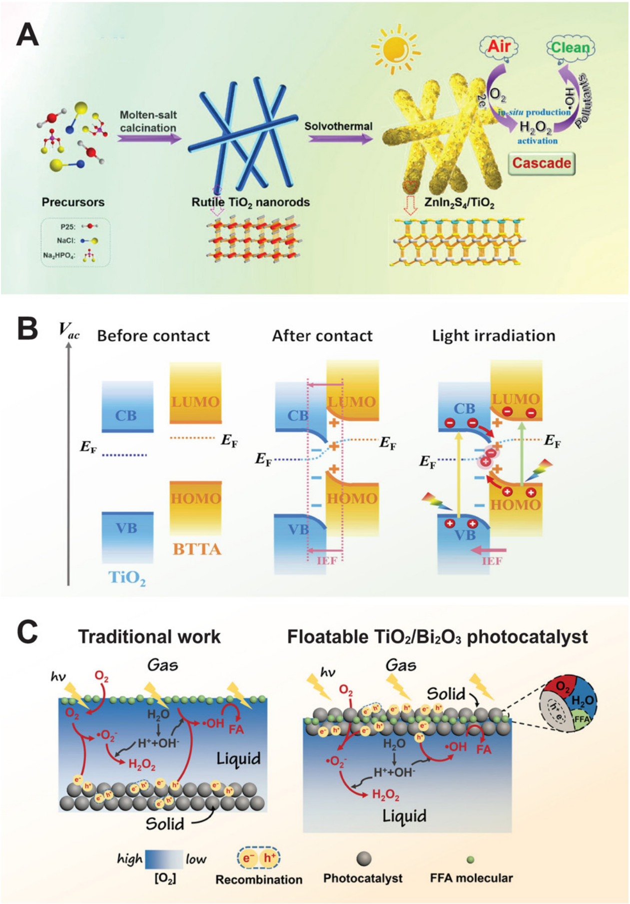

**Fig. 9** (A) Schematic illustration of the preparation of the $ZnIn_2S_4/TiO_2$ heterojunction for *in situ* $H_2O_2$ production and its activation for water remediation under visible light irradiation. Reproduced with permission from ref. 19. Copyright 2022, Elsevier. (B) Charge carrier transfer mechanism of S-scheme $TiO_2$@BTTA photocatalysts. Reproduced with permission from ref. 342. Copyright 2023, Elsevier. (C) Schematic illustration comparing traditional solid photocatalyst with floatable $TiO_2/Bi_2O_3$ photocatalyst, highlighting redox reactions occur at the distinct gas-liquid-solid tri-phase interface. Reproduced with permission from ref. 54. Copyright 2022, Wiley-VCH.

Yang *et al.* developed a composite system comprising $TiO_2$ nanofibers hybridized with porous 4,4,4-(benzene-1,3,5-triyl-tris(ethyne-2,1-diyl))tribenzaldehyde (BTTA) COF, serving as a dual-function photocatalyst for simultaneous hydrogen peroxide production and selective furfuryl alcohol oxidation. This composite system offers several advantages, including a large surface area, superior light absorption, efficient carrier separation, and enhanced redox power through the S-scheme heterojunction (Fig. 9B). Specifically, the $TiO_2$-BTTA composite with a 6 : 1 weight ratio exhibited the highest $H_2O_2$ production activity at 740 μmol $L^{-1}$ $h^{-1}$ and achieved approximately 92% oxidation of furfuryl alcohol.

Going beyond traditional powder photocatalysts, which suffer from severe agglomeration, limited light absorption, poor gas reactant accessibility, and difficulties in reuse, the development of floatable composite photocatalysts presents a promising alternative. These novel floatable composite photocatalysts were synthesized by immobilizing hydrophobic $TiO_2$ and $Bi_2O_3$ on lightweight polystyrene spheres using hydrothermal and photodeposition methods.[54] The photocatalysts are solar transparent and improve contact between reactants and the photocatalyst. Floatable photocatalysts offer significant advantages, such as the rapid diffusion of oxygen to the solid-water interface, which enhances $H_2O_2$ evolution (Fig. 9C). This rapid oxygen delivery facilitates electron consumption, thereby minimizing electron–hole recombination. By combining the benefits of floatable and S-scheme photocatalysts, the $TiO_2/Bi_2O_3$ composite achieves a significantly enhanced $H_2O_2$ yield of 1.15 mM $h^{-1}$ and an furoic acid formation rate of 0.45 mM $h^{-1}$. The innovative design maximizes photocatalytic reaction kinetics and provides a new route for efficient heterogeneous catalysis.

### 7.6. Photocatalytic selective oxidation of alcohol

The selective oxidation of alcohols to produce aldehydes, carboxylic acids, or ketones is an important chemical process in industry.[218,343,344] However, the industrial alcohol oxidation processes use strong oxidants which are toxic with hazardous by-products and require energy intensive conditions such as high temperature and pressure. Hence, there is a pressing need to develop environmentally friendly and sustainable processes for alcohol oxidation under ambient conditions. One promising strategy for oxidation of alcohols is through photocatalysis which can be performed under room temperature and atmospheric pressure and taps on renewable solar energy. $TiO_2$ has garnered significant attention as a photocatalyst for alcohol oxidation due to its abundance, low cost, and non-toxicity. However, its large bandgap limits its activity to the UV region, resulting in lower solar energy utilization.

Courtois *et al.* investigated the photoreforming of tertiary alcohols on Pt-loaded rutile $TiO_2$(110).[345] The process involves hole-mediated disproportionation, which results in the formation of an alkane and the corresponding ketone. Wolde and co-workers synthesized gadolinium-doped $TiO_2$ nanorods decorated with poly(*o*-phenylenediamine) nanowires to enhance photocatalytic performance.[346] Gadolinium doping increases adsorption capacity, introduces half-filled f-orbitals, and causes an optical redshift. Poly(*o*-phenylenediamine), a conducting polymer, improves photocatalytic activity in the visible region by acting as an electron donor and hole transporter. The composite was tested for photocatalytic benzyl alcohol oxidation coupled with p-dinitrobenzene reduction under simulated solar light. The best performance was achieved with 10% gadolinium doping, resulting in a 90.6% yield of benzaldehyde from benzyl alcohol and an 89.1% yield of *p*-nitroaniline from *p*-dinitrobenzene in acetonitrile, while in water, the yields were 70.5% for benzaldehyde and 85.0% for *p*-phenylenediamine.

When $Ti_3C_2$ MXene is combined with $TiO_2$, it significantly enhances the photocatalytic selective oxidation of alcohols, such as benzyl alcohol. Accordingly, the selective oxidation of benzyl alcohol to benzaldehyde over $TiO_2$ relies on the synergy between electrons and holes. $Ti^{3+}$ species in $TiO_2$ are crucial for generating alcohol cation radicals and activating molecular $O_2$, which enhances the conversion efficiency of benzyl alcohol.[347,348] However, the VB potential of $TiO_2$ (2.9 V *vs.* RHE) is more positive than the benzaldehyde/oxidized benzaldehyde redox potential (2.5 V *vs.* RHE), leading to further oxidation of benzaldehyde to byproducts like benzoic acid and $CO_2$, reducing selectivity. Therefore, creating $TiO_2$ with a high concentration of $Ti^{3+}$ species and a less positive VB could improve both conversion efficiency and selectivity for benzaldehyde during the photocatalytic oxidation of benzyl alcohol. The $TiO_2/Ti_3C_2$ composite enhances the photocatalytic selective oxidation of alcohols by stabilizing oxygen vacancies and $Ti^{3+}$ species. This stabilization boosts the production of active intermediates for the conversion of benzyl alcohol to benzaldehyde. The up-shifted valence band of $TiO_2$ in the composite prevents further oxidation of benzaldehyde, increasing selectivity and efficiency.[343]

Recently, $Ti_3C_2/TiO_2$ nanocomposite was used for photocatalytic oxidation of biomass-derived alcohols, and other aromatic alcohols to corresponding aldehydes.[22] The enhanced photocatalytic activity is attributed to the abundant functional groups on the $Ti_3C_2$ MXene and the *in situ* formation of $TiO_2$ nanoparticles on the MXene sheets. The proposed reaction mechanism involves $TiO_2$ nanoparticles forming a close interface with MXene nanosheets. Under full-spectrum illumination, electrons are excited from the valence band to the conduction band of $TiO_2$, then quickly transferred to the $Ti_3C_2$ nanosheets, aiding the separation and prolonging the lifespan of photogenerated carriers. The system facilitates oxidation through photogenerated holes and *tert*-butoxy radicals, driven by the reduction of adsorbed oxygen. The $Ti_3C_2/TiO_2$ composite shows higher photocatalytic conversion efficiency and selectivity for furfuryl alcohol oxidation than pristine $TiO_2$, with the optimized photocatalyst achieving a 99% yield of furfural.

Besides MXene, Lu *et al.* developed core–shell composites composed of $TiO_2$ nanobelts as the core and COFs of varying thicknesses as the shell, which enhanced the reactivity, selectivity, and stability for benzyl alcohol oxidation.[21] The COFs, with their narrow bandgap, absorbed visible light and generated electrons and holes in their conduction and valence bands, respectively. Electrons migrated from the COF's conduction band to $TiO_2$'s conduction band, while holes facilitated the oxidation of benzyl alcohol to form carbon-centered radicals. These radicals reacted with superoxide radicals, produced by the accumulated electrons activating $O_2$, to form benzaldehyde. The $TiO_2$@COF composite with a 15 nm COF shell demonstrated the highest benzyl alcohol conversion (92.5%) with a maximum rate constant of $6.73 \times 10^{-2}$ $h^{-1}$ under visible light (>420 nm), performing 10.1 times better than $TiO_2$ alone and 12.9 times better than COF alone.

### 7.7. Photochromic systems for electronic devices

A $TiO_2$-based color switching system typically involves the reversible color displaying capability of $TiO_2$, which allow the material to change its color in response to an external stimulus, such as an applied voltage or light irradiation.[349–351] A 2D $TiO_2$ layer has been used as the electrochromic layer combining with a MXene layer (*e.g.*, $Ti_3C_2T_x$) for flexible transparent electrodes in electrochromic devices.[352] To attain the desired $TiO_2$ phase, the anatase $TiO_2$ phase was derived from $Ti_3C_2T_x$ through annealing in air, which demonstrated with good electrochromic properties. The $Ti_3C_2Tx$ and $TiO_2$ 2D nanosheets were self-assemble into $Ti_3C_2T_x$ and $TiO_2$ films through liquid/liquid interfacial self-assembly to give a uniform and high coverage layer and transferred consecutively onto a polyethylene terephthalate substrate to form $TiO_2/Ti_3C_2T_x$ heterostructures. The heterostructures demonstrated outstanding electrochromic performance (*e.g.*, fast coloration speed and high coloration efficiency) because of the 2D nature of the $TiO_2$ flakes as well as the well-balanced porosity and loosely networked structures that promote efficient ion diffusion and electron transport. In addition, the 2D network structure also assists in redistributing the induced strain uniformly, enhancing both the mechanical strength and the flexibility of the film, which is important for the application in flexible electrochromic devices.

Several reports have demonstrated the photoreversible color-switching systems based on photocatalytic $TiO_2$ nanocrystals to induce a reversible redox reaction of chromic dyes, resulting in changes in color.[353,354] Later developments in $TiO_2$-based photoreversible color switching systems focused on improving cyclability and coloring duration through doping and surface engineering.[355–357] For instance, binding organic sacrificial electron donors to the surface of $TiO_2$ is beneficial for the stabilization of nanocrystals and removal of photogenerated holes, thereby enabling cycling of the color-switching system until the surface-bound sacrificial donors are exhausted or depleted. On the other hand, the doping-induced lattice distortion in anatase $TiO_2$ nanocrystals promotes efficient charge separation and migration, altering the kinetics of redox reactions, and tuning the material's optical properties. These enhancements enable $TiO_2$ nanocrystals to undergo rapid and reversible changes in color upon exposure to light.[355,358]

By leveraging on the photocatalytic property and color changing capability of $TiO_2$ nanocrystals under redox reaction ($Ti^{3+}$ and $Ti^{4+}$), a photoreversible color-switching paper based on these $TiO_2$ nanocrystals can repeatedly write and erase content in response to UV irradiation and oxygen exposure (Fig. 10A).[359] To promote good coloration response in atmospheric conditions, N-doping was introduced in creating large quantity of defects (oxygen vacancies) on the $TiO_2$ surface to improve the chemisorption of polyol groups for scavenging photo-generated holes. In addition, N-doping also induces substantial physisorption of polyol molecules that acts as a protective layer on the surface of $TiO_2$ nanocrystals by limiting the diffusion of ambient oxygen molecules, thereby reducing the rate of oxidation of $Ti^{3+}$ species back to $Ti^{4+}$ (Fig. 10B). When exposed to UV irradiation, the $TiO_2$ nanocrystals undergo photoexcitation, generating electrons that induce reduction of $Ti^{4+}$ to $Ti^{3+}$ ions in the nanocrystal lattice. This led to a color change from white to black or dark blue at the irradiated regions, allowing for visible writing or marking on the paper surface (Fig. 10C). To erase the writing or markings, the rewritable paper is exposed to oxygen or air, which serves as an oxidizing agent. Oxygen molecules react with the reduced $Ti^{3+}$ ions in the $TiO_2$ nanocrystals, oxidizing them back to $Ti^{4+}$ ions and restoring the original white color of the paper. This color-switching systems process is typically rapid, enabling multiple cycles of writing and erasing without degradation of the paper substrate.

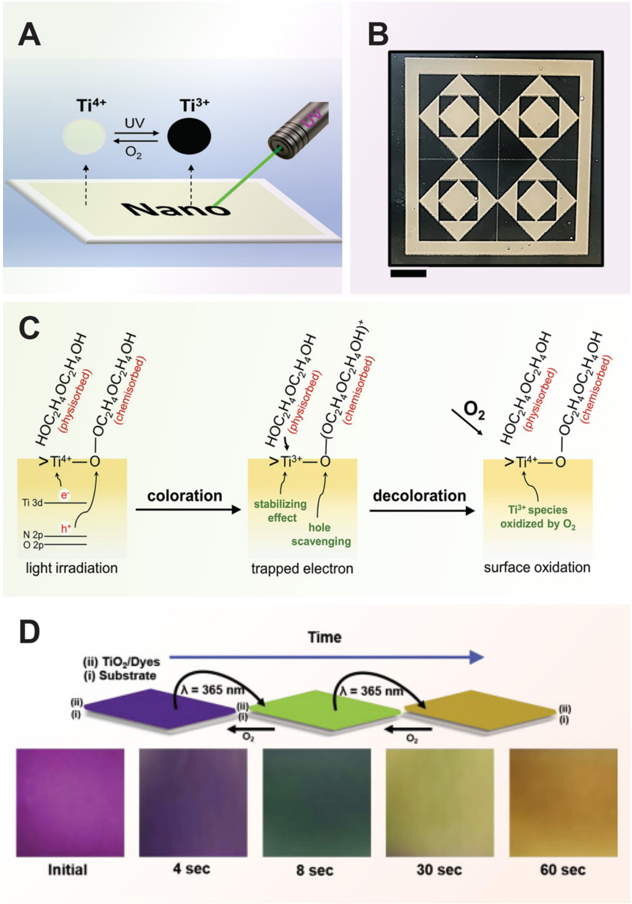

**Fig. 10** Photochromic function of $TiO_2$ semiconductor. (A) Schematic illustration of the writing process on the rewritable paper using a laser pen and (B) light-printed pattern on rewritable film using a UV lamp. (C) Photoreversible color-switching mechanism of N-doped $TiO_2$ nanocrystals. Reproduced with permission from ref. 359. Copyright 2022, Wiley-VCH. (D) Color-switching process and the corresponding color change of the film under continuous UV irradiation. Reproduced with permission from ref. 356. Copyright 2019, Elsevier.

Combining oxygen vacant $TiO_2$ and reduced graphene oxide enables the realization of four distinct types of photochromic devices, each exhibiting unique properties and functionalities (*i.e.*, multi-wavelength photochromism, intensity-dependent photochromism, time-dependent photochromism, dual-response hydro-/photochromism).[356] All of the mentioned photochromic devices can exhibit rapid and reversible color changes through precise control of applied stimuli and demonstrate distinct multi-color states. By carefully engineering the composition and structure of the composite material, the multi-wavelength photochromic device can selectively respond to specific regions of the electromagnetic spectrum. The intensity-dependent photochromic device responds sensitively to variations in the intensity of incident light. In the time-dependent photochromic device, color changes evolve gradually over time in response to continuous light illumination (Fig. 10D). The dual-response hydro-/photochromic device exhibits reversible color changes in response to both light irradiation and variations in humidity. The success of these designs hinge on the development of a highly reductive catalyst as well as the manipulation of the film structure and the dye reduction kinetics to exhibit distinctive and customizable responses to various stimuli, such as light, humidity, or temperature changes. This approach enables the development of versatile and functional photochromic materials with applications across diverse fields, including optoelectronics, advanced sensors, displays, and rewritable media.

### 7.8. Photocatalytic reactions for plastics: polymerization, degradation and conversion

The ability of semiconductors to generate free radicals upon photoexcitation, allows them to be employed for initiating heterogenous free radical polymerization, which is a commonly used method for synthesizing polymers from vinyl monomers. The radicals are generated *via* the photodegradation of surrounding organic compounds[360] or water when they react with the holes in the VB of $TiO_2$ (refer to section 1). These compounds containing radicals would then serve as the initiators for free radical polymerization to take place. The first photocatalytic surface-Initiated polymerization $TiO_2$ photoinitiated polymerization were reported by Kraeutler *et al.*, for the bulk polymerization methyl methacrylate (MMA).[361] Other semiconductors, such as ZnO and CdS, shows similar photoinitiation ability for free radical polymerization.[362–364] Apart from PMMA,[365–368] polymerization of other vinyl monomers have also been reported including homopolymers such as poly (styrene),[362,364] and co-polymers consisting of different repeat units.[369] Interestingly, such heterogeneous surface-initiated polymerization technique opens the pathway to fabricate core–shell structures that have a polymer shell encapsulating the inorganic semiconducting particles. For instance, Kong *et al.* synthesized $TiO_2$ particles embedded within antibacterial poly[2-(*tert*-butylamino)ethyl methacrylateco-ethylene glycol dimethacrylate] shell.[369] Wang *et al.* synthesized core–shell nanospheres with $TiO_2$ core embedded within PMMA, poly(styrene) or Poly(*N*-isopropylacrylamide) (PNIPAM) shell, along with tunable spherical structures that can be manipulated through the compatibility between the polymers and $TiO_2$ particles.[370] For other non-photoactive particles (*e.g.*, $SiO_2$), a thin layer of $TiO_2$ coating would allow them to achieve similar photocatalytic polymerization ability.[370,371]

On the other hand, the generation of radical by $TiO_2$ can also lead to depolymerization, which reduces the molecular weight of polymers, and hence, resulting in degradation to the physical properties of plastic materials. Polyolefins, the largest class of polymers produced, can be subjected to accelerated degradation by radicals generated by $TiO_2$, despite being amongst the most chemically resistant among plastics.[372,373] For instance, the hydroxyl radicals generated by $TiO_2$ can lead to hydrogen abstraction of polyolefins, forming alkyl radicals that causes a series of reaction including chain scissions. Zapata *et al.* reported about 57–60% reduction in molecular weight of polypropylene with $TiO_2$ nanotubes embedded within as compared to 37% reduction for pure polypropylene, after subjecting to 0.55 W $m^{-2}$ of 340 nm irradiation for 10 days.[374] Similarly, Day reported significant reduction in embrittlement times (defined as 50% reduction in elongation as break) of 100 μm thick polyethylene films embedded with different forms (*e.g.* polymorphs, coated/uncoated) of $TiO_2$.[375] Uncoated anatase appears to the most active, with 20 000 mg $kg^{-1}$ incorporated embedded in polyethylene, a ten times reduction in embrittlement time is observed as compared to the pristine polyethylene. Zhao *et al.* also reported on enhanced photocatalytic degradation of polyethylene using copper phthalocyanine modified $TiO_2$, leading to faster photodegradation rates.[449] On the other hand, $TiO_2$ particles have commonly been incorporated into polyvinyl chloride to prevent UV degradation.[16] Their ability for UV absorption can compete with direct UV-induced degradation associated with vinyl polymers, given the bonds energy of C–C (375 kJ $mol^{-1}$) and C–H (420 kJ $mol^{-1}$) falls within the range of UV light energies.[372] However, they will also induce photocatalytic oxidative degradation with radical generation, leading to the loss of gloss on the polyvinyl chloride surface and the degradation of mechanical properties. Nevertheless, it has been reported that the penetration of UV light reduces by 90% at a depth of 20 μm,[376,377] thereby limiting the degradation to a shallow surface, while the bulk of polyvinyl chloride remains largely protected.

Photocatalytic depolymerization also opens up a pathway for plastic recycling, as monomeric building blocks can be recovered for re-polymerization. Such chemical recycling techniques are often less energy-intensive than conventional mechanical method.[378–380] In comparison, mechanical recycling methods causes material degradation leading to lower quality and reduced properties of the recycled materials, thereby often being labelled as a "downcycling" process. This is unlike chemical recycling that deconstructs the material at a molecular level, allowing a renewed production of the pristine material. For example, Daraboina and Madras employed $TiO_2$ synthesized by combustion synthesis to perform photocatalytic degradation of PMMA, poly(butyl methacrylate) (PBMA) and their co-polymers, yielding their respective monomers.[381] These recovered monomers can serve as the feedstock for the repolymerization of these poly (alkyl methacrylates).[382]

Similarly, photocatalysis can also be an effective tool to convert plastic materials to other chemical species beyond their monomeric/oligomeric form, allowing them to be repurposed upon reaching their end of life.[383–386] Recently, Nguyen and Edalati employed $TiO_2$ for the photoconversion of poly(ethylene terephthalate) (PET) to terephthalate and acetic acid, and the latter is widely used in chemical, plastic and food production.[387] They also found brookite polymorph of $TiO_2$ to be most active in this photocoversion process, followed by rutile, and finally anatase. Other than such direct photoconversion of plastics, the polymers also can undergo an initial step of degradation/depolymerization to smaller chemical compound prior to photocatalytic conversion into other useful molecules. For example, Han *et al.* reported photocatalytic conversion of ethylene glycol derived from alkaline hydrolyzed PET, into glycolic acid, glycolaldehyde, and ethanol, using photocatalytic carbonized polymer dots graphitic carbon nitride.[388] Similarly, for $TiO_2$, Bhattacharjee *et al.* performed enzymatic pretreatments on polyesters plastic prior to photo conversion of PET and polycaprolactone using Pt-loaded $TiO_2$, resulting in the formation of pentanal and formic acid products.[56] In cases where the chemical products obtained are of higher value than the initial plastic, such processes would be referred to as an "upcycling" process. For example, using $TiO_2$ modified with potassium stearate or *N*,*N*-diethyl-3-(trimethoxysilyl)propan-1-amine, Peng *et al.* reported the successful photoconversion of poly(styrene) wastes into benzoic acid with 18–44.2 mol% yields under mild conditions.[389] Such aromatic compounds would find applications food, cosmetic and pharmaceutical products.

In addition, many of the photoconversion process of plastic materials described above can be conducted with a simultaneous production of hydrogen fuel. This process commonly known as photoreforming first described by Kawai and Sakata in 1981, using Xe-lamp irradiation on platinized $TiO_2$ photocatalyst in the presence of water and chlorine or nitrogen containing organic molecules.[37] The difference between photoforming and typical photocatalytic water splitting is the participation of the organics (*i.e.*, polymer or plastic-derived chemicals) as a feedstock for hydrogen production. In photoreforming, the oxidation of the organic compound replaces oxygen evolution reaction for hole consumption, thereby acting as a hole scavenger that supresses the electron–hole recombination, resulting in the increase rate of $H^+/H_2O$ reduction boosting $H_2O$ production as compared to typical photocatalytic water splitting.[384,390,391] More importantly, the additional production of clean $H_2$ fuel further adds value to the photocatalytic conversion of plastic materials.

## 8. Conclusions and perspectives

Photocatalysis is recognized as a promising sustainable technology for solving environmental and energy problems by harnessing solar light. Numerous research attempts in the field of photocatalysis have clearly shown that $TiO_2$ is one of the most extensively studied photocatalysts due to its excellent photocatalytic properties. The continuous progress in $TiO_2$ photocatalyst research is driven by the material's inherent advantages such as chemical stability, non-toxicity, cost-effectiveness, and strong oxidative power under UV light. However, the challenges of narrow light absorption and fast charge recombination have prompted extensive research into $TiO_2$ material engineering. In view of these developments, the emergence of $TiO_2$ photocatalysis and the modification methods of $TiO_2$-based photocatalysts were comprehensively reviewed in this paper.

Advancements in engineering $TiO_2$ through doping have extended its activity into the visible light range. However, metal doping faces challenges such as thermal instability, high fabrication costs, and increased charge-carrier recombination, which reduce efficiency. Conversely, non-metal doping is generally more cost-effective and stable but requires careful control to avoid disrupting the lattice structure. By integrating techniques like morphological control, crystal phase manipulation, doping, and hybridization, researchers have improved charge carrier separation and extended the applicability of $TiO_2$ in a wide range of photooxidation and photoreduction reactions. These applications include organic pollutant degradation, photocatalytic disinfection, hydrogen generation, $CO_2$ reduction, nitrogen fixation, hydrogen peroxide generation, alcohol oxidation, plastic polymerization and degradation, and photochromic applications.

Future research in $TiO_2$ photocatalysis is poised to focus on several key areas, particularly the modification of $TiO_2$ materials to enhance their performance. Advances in 3D printing technologies have significantly impacted the development of these materials. 3D printing allows for precise control over the design and fabrication process, enabling the creation of complex structures with tailored porosity and flow characteristics. By building objects layer by layer from digital designs, 3D printing can produce photocatalytic materials with optimized pore sizes and shapes, enhancing the flow of pollutants and improving contact with the photocatalyst surface. This precision in design is expected to lead to significant improvements in the efficiency and effectiveness of photocatalytic materials.

Another promising area of future research is the development of single-atom catalysts. These catalysts represent the ultimate small-size limit for metal particles, containing isolated metal atoms singly dispersed on supports. Single-atom catalysts maximize the efficiency of metal atom use, which is particularly important for supported noble metal catalysts. The well-defined and uniform dispersion of single atoms offers great potential for achieving high catalytic activity and selectivity. By utilizing each metal atom to its fullest potential, single-atom catalysts can provide exceptional performance in various catalytic applications, including photocatalysis.

Photocatalytic upcycling and depolymerization of polymers have emerged as promising strategies to address plastic pollution and advance a circular economy. Recycling polymers with backbone structures primarily composed of C–C bonds is particularly challenging due to the lack of functional groups, making these materials difficult to break down and reuse. Consequently, the valorization of common commodity plastics such as polyethylene (PE) and polypropylene (PP), which are major contributors to the plastic pollution problem, is a crucial next step.

Traditional studies of $TiO_2$ photocatalysis have used static ensemble-averaged methods, providing valuable but limited insights into fundamental processes. Future research will utilize advanced *in situ* and time-resolved techniques to capture real-time dynamic processes, such as ultrafast electron dynamics and charge carrier lifetimes, revealing key mechanisms like charge separation and transfer. For example, *in situ* extended X-ray absorption fine structure has been used to study the dynamic changes in chemical valence and coordination environment of isolated metal centers in a multi-edged $TiO_2$-supported single-atom Ru photocatalyst. Additionally, femtosecond time-resolved, surface-specific vibrational sum frequency generation spectroscopy has investigated the photoinduced reaction at the $TiO_2$–water interface, observing the interfacial water molecule reactions with high temporal precision. *In situ* mass spectrometry will further aid in analyzing gaseous products and intermediates, elucidating reaction pathways and mechanisms.

Future research in $TiO_2$ photocatalysis will increasingly rely on theoretical calculations, such as density functional theory, molecular dynamics simulations, and kinetic modeling, to complement experimental techniques. These computational methods will model electronic structures, predict reactivity, and develop comprehensive reaction models, providing a holistic understanding of photocatalytic mechanisms. This integration will enable the optimization and development of more efficient and tailored photocatalysts for various applications. Currently, research on $TiO_2$ photocatalysts largely depends on experimental work, which can be complex and costly. Moving forward, the incorporation of machine learning, big data, and artificial intelligence holds significant potential to generate high-performance models that predict material properties and elucidate property–structure relationships. These advanced computational tools can streamline the research process through high-throughput screening, reduce experimental complexity, and lower costs. This approach will not only enhance our understanding of $TiO_2$-based photocatalysts but also drive the development of more effective and efficient materials, advancing their practical applications on an industrial scale.

## Author contributions

Conceptualization and writing – original draft: S. Y. Tee, J. Kong, J. J. Koh, C. P. Teng, X. Wang, X. Wang, S. L. Teo. Conceptualization, supervision and writing – review & editing: W. Thitsartarn, M-Y Han, and Z. W. Seh. All authors have read and agreed to the published version of the manuscript.

## Data availability

No primary research results, software or code have been included and no new data were generated or analysed as part of this review.

## Conflicts of interest

There are no conflicts to declare.

## Acknowledgements

This research is supported by the National Research Foundation, Singapore, and Agency for Science, Technology and Research (A*STAR), under its low carbon energy research (LCER) phase 2 HETFI Directed Hydrogen programme (Grant No.: U2307D4001), the A*STAR SERC MTC YIRG (Grant No.: M21K3c0125), and the A*STAR IMRE–SCG Chemicals Advanced Composite Joint Lab (IAF-ICP Project No.: I1801E0024).

## References

1 P. Riente and T. Noël, *Catal. Sci. Technol.*, 2019, **9**, 5186–5232.
2 C. Larquet and S. Carenco, *Front. Chem.*, 2020, **8**, 179.
3 H. Hao and X. Lang, *ChemCatChem*, 2019, **11**, 1378–1393.
4 M. Ahmed and G. Xinxin, *Inorg. Chem. Front.*, 2016, **3**, 578–590.
5 D. Sudha and P. Sivakumar, *Chem. Eng. Process.: Process Intensif.*, 2015, **97**, 112–133.
6 A. Fujishima and K. Honda, *Nature*, 1972, **238**, 37–38.
7 Y. Tanaka, S. L. Lim, W. P. Goh, C. Jiang, S. Y. Tee, T. Ye, X. Li, K. H. Nguyen, C. J. J. Lee, N. Ding, Z. Liu, J. Wu, J. Zhang and M. Y. Han, *ChemNanoMat*, 2018, **4**, 394–400.
8 C. P. Teng, M. Y. Tan, J. P. W. Toh, Q. F. Lim, X. Wang, D. Ponsford, E. M. J. Lin, W. Thitsartarn and S. Y. Tee, *Materials*, 2023, **16**, 3856.
9 S. Banerjee, D. D. Dionysiou and S. C. Pillai, *Appl. Catal., B*, 2015, **176–177**, 396–428.
10 P. V. Laxma Reddy, B. Kavitha, P. A. Kumar Reddy and K. H. Kim, *Environ. Res.*, 2017, **154**, 296–303.
11 S. Zhang, J. Zhang, J. Sun and Z. Tang, *Chem. Eng. Process.: Process Intensif.*, 2020, **147**, 107746.
12 K. Y. Tang, J. X. Chen, E. D. R. Legaspi, C. Owh, M. Lin, I. S. Y. Tee, D. Kai, X. J. Loh, Z. Li, M. D. Regulacio and E. Ye, *Chemosphere*, 2021, **265**, 129114.
13 Z. W. Seh, S. Liu, M. Low, S. Y. Zhang, Z. Liu, A. Mlayah and M. Y. Han, *Adv. Mater.*, 2012, **24**, 2310–2314.
14 S. Y. Tee, K. Y. Win, W. S. Teo, L. D. Koh, S. Liu, C. P. Teng and M. Y. Han, *Adv. Sci.*, 2017, **4**, 1600337.
15 S. Jiang, K. Zhao, M. Al-Mamun, Y. L. Zhong, P. Liu, H. Yin, L. Jiang, S. Lowe, J. Qi, R. Yu, D. Wang and H. Zhao, *Inorg. Chem. Front.*, 2019, **6**, 1667–1674.
16 J. Wang, R. T. Guo, Z. X. Bi, X. Chen, X. Hu and W. G. Pan, *Nanoscale*, 2022, **14**, 11512–11528.
17 X. Chen, N. Li, Z. Kong, W.-J. Ong and X. Zhao, *Mater. Horiz.*, 2018, **5**, 9–27.
18 M. Cheng, C. Xiao and Y. Xie, *J. Mater. Chem. A*, 2019, **7**, 19616–19633.
19 J. Hu, T. Yang, J. Chen, X. Yang, J. Qu and Y. Cai, *J. Chem. Eng.*, 2022, **430**, 133039.
20 Z. Chen, D. Yao, C. Chu and S. Mao, *Chem. Eng. J.*, 2023, **451**, 138489.
21 G. Lu, X. Huang, Z. Wu, Y. Li, L. Xing, H. Gao, W. Dong and G. Wang, *Appl. Surf. Sci.*, 2019, **493**, 551–560.
22 I. R. Warkad, R. Paul, S. Parthiban and M. B. Gawande, *J. Environ. Chem. Eng.*, 2024, **12**, 113128.
23 W. J. Ong, L. L. Tan, S. P. Chai, S. T. Yong and A. R. Mohamed, *Nanoscale*, 2014, **6**, 1946–2008.
24 A. Bumajdad and M. Madkour, *Phys. Chem. Chem. Phys.*, 2014, **16**, 7146–7158.
25 X. Chen, L. Liu, P. Y. Yu and S. S. Mao, *Science*, 2011, **331**, 746–750.
26 E. Roduner, *Chem. Soc. Rev.*, 2006, **35**, 583–592.
27 M. Valden, *Science*, 1998, **281**, 1647–1650.
28 X. Wang, Z. Li, J. Shi and Y. Yu, *Chem. Rev.*, 2014, **114**, 9346–9384.
29 S. Y. Tee and E. Ye, *Mater. Adv.*, 2021, **2**, 1507–1529.
30 J. Wang, Z. Wang, W. Wang, Y. Wang, X. Hu, J. Liu, X. Gong, W. Miao, L. Ding, X. Li and J. Tang, *Nanoscale*, 2022, **14**, 6709–6734.
31 X.-X. Fang, L.-B. Ma, K. Liang, S.-J. Zhao, Y.-F. Jiang, C. Ling, T. Zhao, T.-Y. Cheang and A.-W. Xu, *J. Mater. Chem. A*, 2019, **7**, 11506–11512.
32 Z. Ding, M. Sun, W. Liu, W. Sun, X. Meng and Y. Zheng, *Sep. Purif. Technol.*, 2021, **276**, 119287.
33 D. Yu, Q. Shao, Q. Song, J. Cui, Y. Zhang, B. Wu, L. Ge, Y. Wang, Y. Zhang, Y. Qin, R. Vajtai, P. M. Ajayan, H. Wang, T. Xu and Y. Wu, *Nat. Commun.*, 2020, **11**, 927.
34 E. Abraham, V. Cherpak, B. Senyuk, J. B. ten Hove, T. Lee, Q. Liu and I. I. Smalyukh, *Nat. Energy*, 2023, **8**, 381–396.
35 A. Fujishima and K. Honda, *Nature*, 1972, **238**, 37–38.
36 A. J. Bard, *J. Photochem.*, 1979, **10**, 59–75.
37 T. Kawai and T. Sakata, *Chem. Lett.*, 1981, **10**, 81–84.

38 N. Serpone, E. Borgarello and M. Grätzel, *J. Chem. Soc., Chem. Commun.*, 1984, 342–344.

39 C. Kormann, D. W. Bahnemann and M. R. Hoffmann, *Environ. Sci. Technol.*, 1988, **22**, 798–806.

40 J. C. D'Oliveira, G. Al-Sayyed and P. Pichat, *Environ. Sci. Technol.*, 2002, **24**, 990–996.

41 N. N. Rao, S. Dube, Manjubala and P. Natarajan, *Appl. Catal., B*, 1994, **5**, 33–42.

42 K. Naoi, Y. Ohko and T. Tatsuma, *J. Am. Chem. Soc.*, 2004, **126**, 3664–3668.

43 H. Tada, T. Mitsui, T. Kiyonaga, T. Akita and K. Tanaka, *Nat. Mater.*, 2006, **5**, 782–786.

44 W. Ren, Z. Ai, F. Jia, L. Zhang, X. Fan and Z. Zou, *Appl. Catal., B*, 2007, **69**, 138–144.

45 M. Zhang, C. Chen, W. Ma and J. Zhao, *Angew. Chem., Int. Ed.*, 2008, **47**, 9730–9733.

46 D. Zhang, G. Li, X. Yang and J. C. Yu, *Chem. Commun.*, 2009, 4381–4383.

47 J. Yu, S. Wang, J. Low and W. Xiao, *Phys. Chem. Chem. Phys.*, 2013, **15**, 16883–16890.

48 S. Zhou, Y. Liu, J. Li, Y. Wang, G. Jiang, Z. Zhao, D. Wang, A. Duan, J. Liu and Y. Wei, *Appl. Catal., B*, 2014, **158–159**, 20–29.

49 Q. Liu, Q. Cao, H. Bi, C. Liang, K. Yuan, W. She, Y. Yang and R. Che, *Adv. Mater.*, 2016, **28**, 486–490.

50 J. Wan, W. Chen, C. Jia, L. Zheng, J. Dong, X. Zheng, Y. Wang, W. Yan, C. Chen, Q. Peng, D. Wang and Y. Li, *Adv. Mater.*, 2018, **30**, 1705369.

51 J. Fu, Q. Xu, J. Low, C. Jiang and J. Yu, *Appl. Catal., B*, 2019, **243**, 556–565.

52 Y. Zhao, Y. Zhao, R. Shi, B. Wang, G. I. N. Waterhouse, L. Z. Wu, C. H. Tung and T. Zhang, *Adv. Mater.*, 2019, **31**, e1806482.

53 H. Zhang, S. Zuo, M. Qiu, S. Wang, Y. Zhang, J. Zhang and X. W. D. Lou, *Sci. Adv.*, 2020, **6**, eabb9823.

54 B. He, Z. Wang, P. Xiao, T. Chen, J. Yu and L. Zhang, *Adv. Mater.*, 2022, **34**, e2203225.

55 L. Liccardo, M. Bordin, P. M. Sheverdyaeva, M. Belli, P. Moras, A. Vomiero and E. Moretti, *Adv. Funct. Mater.*, 2023, **33**, 2212486.

56 S. Bhattacharjee, C. Guo, E. Lam, J. M. Holstein, M. Rangel Pereira, C. M. Pichler, C. Pornrungroj, M. Rahaman, T. Uekert, F. Hollfelder and E. Reisner, *J. Am. Chem. Soc.*, 2023, **145**, 20355–20364.

57 Z. Warren, T. T. Guaraldo, I. Barisic, G. A. Zoumpouli, J. Wenk and D. Mattia, *J. Mater. Chem. A*, 2024, **12**, 10913–10922.

58 X. Qin, M. Xu, J. Guan, L. Feng, Y. Xu, L. Zheng, M. Wang, J.-W. Zhao, J.-L. Chen, J. Zhang, J. Xie, Z. Yu, R. Zhang, X. Li, X. Liu, J.-X. Liu, J. Zheng and D. Ma, *Nat. Energy*, 2024, **9**, 154–162.

59 Z. Wei, L. Wu, X. Yue, H. Mu, Z. Li, Y. Chang, M. Janczarek, S. Juodkazis and E. Kowalska, *Appl. Catal., B*, 2024, **345**, 123654.

60 D. A. H. Hanaor and C. C. Sorrell, *J. Mater. Sci.*, 2010, **46**, 855–874.

61 D. R. Eddy, G. A. Nur Sheha, M. D. Permana, N. Saito, T. Takei, N. Kumada, Irkham, I. Rahayu, I. Abe, Y. Sekine, T. Oyumi and Y. Izumi, *Chemosphere*, 2024, **351**, 141206.

62 C. Chen, W. Ma and J. Zhao, *Chem. Soc. Rev.*, 2010, **39**, 4206–4219.

63 W. Wang, J. C. Yu, D. Xia, P. K. Wong and Y. Li, *Environ. Sci. Technol.*, 2013, **47**, 8724–8732.

64 J. Ran, M. Jaroniec and S. Z. Qiao, *Adv. Mater.*, 2018, **30**, 1704649.

65 P. S. Basavarajappa, S. B. Patil, N. Ganganagappa, K. R. Reddy, A. V. Raghu and C. V. Reddy, *Int. J. Hydrogen Energy*, 2020, **45**, 7764–7778.

66 M. Sultana, A. Mondal, S. Islam, M. A. Khatun, M. H. Rahaman, A. K. Chakraborty, M. S. Rahman, M. M. Rahman and A. S. M. Nur, *Curr. Res. Green Sustainable Chem.*, 2023, **7**, 100383.

67 F. Zou, J. Hu, W. Miao, Y. Shen, J. Ding and X. Jing, *ACS Omega*, 2020, **5**, 28510–28516.

68 M. E. Kurtoglu, T. Longenbach and Y. Gogotsi, *Int. J. Appl. Glass Sci.*, 2011, **2**, 108–116.

69 E. Aubry, M. N. Ghazzal, V. Demange, N. Chaoui, D. Robert and A. Billard, *Surf. Coat. Technol.*, 2007, **201**, 7706–7712.

70 Y. Bessekhouad, D. Robert, J. V. Weber and N. Chaoui, *J. Photochem. Photobiol., A*, 2004, **167**, 49–57.

71 G. Yang, Z. Yan, T. Xiao and B. Yang, *J. Alloys Compd.*, 2013, **580**, 15–22.

72 I. Singh and B. Birajdar, *RSC Adv.*, 2017, **7**, 54053–54062.

73 H. Rahman, A. Norbert, P. S. Nair, J. A. Joseph, S. Shaji, U. Deshpande, J. Naduvath, A. Shanu and R. R. Philip, *Opt. Mater.*, 2022, **134**, 113172.

74 E. Shin, S. Jin, J. Kim, S.-J. Chang, B.-H. Jun, K.-W. Park and J. Hong, *Appl. Surf. Sci.*, 2016, **379**, 33–38.

75 Z. N. Kayani, A. Iqbal, Z. Bashir, S. Riaz and S. Naseem, *Inorg. Chem. Commun.*, 2023, **151**, 110560.

76 Z. Ma, X. Ma, L. Yang, X. Liu, Z. Zhong and B. Hou, *Appl. Surf. Sci.*, 2022, **580**, 152274.

77 L. Jia, L.-M. Yang, W. Wang, S.-T. Huang and Z. Xu, *Rare Met.*, 2019, **43**, 555–561.

78 B. Roose, S. Pathak and U. Steiner, *Chem. Soc. Rev.*, 2015, **44**, 8326–8349.

79 D. Fang, F. He and J. Xie, *J. Energy Inst.*, 2019, **92**, 319–331.

80 K. Athira, K. T. Merin, T. Raguram and K. S. Rajni, *Mater. Today: Proc.*, 2020, **33**, 2321–2327.

81 M. Ikram, M. A. Ul Haq, A. Haider, J. Haider, A. Ul-Hamid, I. Shahzadi, M. A. Bari, S. Ali, S. Goumri-Said and M. B. Kanoun, *Nanoscale Adv.*, 2022, **4**, 3996–4008.

82 S. P. Keerthana, R. Yuvakkumar, G. Ravi, M. Thambidurai, H. D. Nguyen and D. Velauthapillai, *RSC Adv.*, 2023, **13**, 18779–18787.

83 E. Santos, A. C. Catto, A. F. Peterline and W. Avansi Jr, *Appl. Surf. Sci.*, 2022, **579**, 152146.

84 D. Zhang, J. Chen, Q. Xiang, Y. Li, M. Liu and Y. Liao, *Inorg. Chem.*, 2019, **58**, 12511–12515.

85 L. Huang, G. He, Y. Yuan, T. C. Zhang, Y. Wang and S. Yuan, *Ind. Eng. Chem. Res.*, 2024, **63**, 7154–7165.

86 S.-m. Chang and W.-s. Liu, *Appl. Catal., B*, 2014, **156–157**, 466–475.

87 J. Poostforooshan, S. Belbekhouche, V. Olszok, M. F. B. Stodt, M. Simmler, M. Bierwirth, H. Nirschl, J. Kiefer, U. Fritsching and A. P. Weber, *ACS Appl. Nano Mater.*, 2023, **6**, 22660–22672.

88 V. Moradi, M. B. G. Jun, A. Blackburn and R. A. Herring, *Appl. Surf. Sci.*, 2018, **427**, 791–799.

89 L. Song, X. Zhao, L. Cao, J. W. Moon, B. Gu and W. Wang, *Nanoscale*, 2015, **7**, 16695–16703.

90 R. Zhu, H. Jiang, Y. Xie, D. Xu, Y. Duo, Y. Zhu, Y. Mei and D. Xie, *Prog. Org. Coat.*, 2024, **189**, 108272.

91 J. Liang, J. Wang, K. Song, X. Wang, K. Yu and C. Liang, *J. Rare Earths*, 2020, **38**, 148–156.

92 S. Stojadinović, N. Tadić, N. Radić, B. Grbić and R. Vasilić, *Surf. Coat. Technol.*, 2018, **337**, 279–289.

93 J. Reszczyńska, T. Grzyb, J. W. Sobczak, W. Lisowski, M. Gazda, B. Ohtani and A. Zaleska, *Appl. Surf. Sci.*, 2014, **307**, 333–345.

94 J. Reszczyńska, T. Grzyb, J. W. Sobczak, W. Lisowski, M. Gazda, B. Ohtani and A. Zaleska, *Appl. Catal., B*, 2015, **163**, 40–49.

95 J. Reszczyńska, T. Grzyb, Z. Wei, M. Klein, E. Kowalska, B. Ohtani and A. Zaleska-Medynska, *Appl. Catal., B*, 2016, **181**, 825–837.

96 V. Đorđević, B. Milićević and M. D. Dramićanin, *Rare Earth-Doped Anatase $TiO_2$ Nanoparticles*, IntechOpen Inc., 2017.

97 H. Dong, G. Zeng, L. Tang, C. Fan, C. Zhang, X. He and Y. He, *Water Res.*, 2015, **79**, 128–146.

98 J. P. Jeon, D. H. Kweon, B. J. Jang, M. J. Ju and J. B. Baek, *Adv. Sustainable Syst.*, 2020, **4**, 2000197.

99 P. Niu, G. Wu, P. Chen, H. Zheng, Q. Cao and H. Jiang, *Front. Chem.*, 2020, **8**, 172.

100 A. Zaleska, E. Grabowska, J. W. Sobczak, M. Gazda and J. Hupka, *Appl. Catal., B*, 2009, **89**, 469–475.

101 M. Quesada-Gonzalez, N. D. Boscher, C. J. Carmalt and I. P. Parkin, *ACS Appl. Mater. Interfaces*, 2016, **8**, 25024–25029.

102 Y. Cong, X. Li, Y. Qin, Z. Dong, G. Yuan, Z. Cui and X. Lai, *Appl. Catal., B*, 2011, **107**, 128–134.

103 C. Liu, H. Chen, K. Dai, A. Xue, H. Chen and Q. Huang, *Mater. Res. Bull.*, 2013, **48**, 1499–1505.

104 J. Zhang, M. Vasei, Y. Sang, H. Liu and J. P. Claverie, *ACS Appl. Mater. Interfaces*, 2016, **8**, 1903–1912.

105 A. Trapalis, N. Todorova, T. Giannakopoulou, N. Boukos, T. Speliotis, D. Dimotikali and J. Yu, *Appl. Catal., B*, 2016, **180**, 637–647.

106 D. He, Y. Li, I. Wang, J. Wu, Y. Yang and Q. An, *Appl. Surf. Sci.*, 2017, **391**, 318–325.

107 M. A. Mohamed, W. N. Wan Salleh, J. Jaafar, M. S. Rosmi, Z. A. Mohd Hir, M. Abd Mutalib, A. F. Ismail and M. Tanemura, *Appl. Surf. Sci.*, 2017, **393**, 46–59.

108 B. Tang, H. Chen, H. Peng, Z. Wang and W. Huang, *Nanomaterials*, 2018, **8**, 105.

109 Y. Duan, X. Chen, X. Zhang, W. Xiang and C. Wu, *Solid State Sci.*, 2018, **86**, 12–18.

110 Y.-T. Lin, C.-H. Weng, Y.-H. Lin, C.-C. Shiesh and F.-Y. Chen, *Sep. Purif. Technol.*, 2013, **116**, 114–123.

111 S. Yu, H. J. Yun, Y. H. Kim and J. Yi, *Appl. Catal., B*, 2014, **144**, 893–899.

112 R. Asahi, T. Morikawa, T. Ohwaki, K. Aoki and Y. Taga, *Science*, 2001, **293**, 269–271.

113 S. A. Ansari, M. M. Khan, M. O. Ansari and M. H. Cho, *New J. Chem.*, 2016, **40**, 3000–3009.

114 C. Li, M. Gu, M. Gao, K. Liu, X. Zhao, N. Cao, J. Feng, Y. Ren, T. Wei and M. Zhang, *J. Colloid Interface Sci.*, 2022, **609**, 341–352.

115 L. Hu, J. Wang, J. Zhang, Q. Zhang and Z. Liu, *RSC Adv.*, 2014, **4**, 420–427.

116 L. Huang, W. Fu, X. Fu, B. Zong, H. Liu, H. Bala, X. Wang, G. Sun, J. Cao and Z. Zhang, *Mater. Lett.*, 2017, **209**, 585–588.

117 P. H. Le, L. T. Hieu, T. N. Lam, N. T. N. Hang, N. V. Truong, L. T. C. Tuyen, P. T. Phong and J. Leu, *Micromachines*, 2018, **9**, 618.

118 J. Wang, C. Fan, Z. Ren, X. Fu, G. Qian and Z. Wang, *Dalton Trans.*, 2014, **43**, 13783–13791.

119 S. Samangsri, S. Chiarakorn and T. Areerob, *IOP Conf. Ser.: Mater. Sci. Eng.*, 2019, **576**, 012033.

120 H. Wu, D. Yang, X. Zhu, P. Gu, H. Sun, P. Wangyang, J. Li, X. He and L. Fan, *CrystEngComm*, 2018, **20**, 4133–4140.

121 Y.-C. Tang, X.-H. Huang, H.-Q. Yu and L.-H. Tang, *Int. J. Photoenergy*, 2012, **2012**, 1–10.

122 R. Quesada-Cabrera, C. Sotelo-Vázquez, M. Quesada-González, E. P. Melián, N. Chadwick and I. P. Parkin, *J. Photochem. Photobiol., A*, 2017, **333**, 49–55.

123 C. W. Dunnill and I. P. Parkin, *Dalton Trans.*, 2011, **40**, 1635–1640.

124 F. Xiao, W. Zhou, B. Sun, H. Li, P. Qiao, L. Ren, X. Zhao and H. Fu, *Sci. China Mater.*, 2018, **61**, 822–830.

125 C. Foo, Y. Li, K. Lebedev, T. Chen, S. Day, C. Tang and S. C. E. Tsang, *Nat. Commun.*, 2021, **12**, 661.

126 K. Wang, J. Yu, L. Liu, L. Hou and F. Jin, *Ceram. Int.*, 2016, **42**, 16405–16411.

127 L. Körösi, S. Papp, I. Bertóti and I. Dékány, *Chem. Mater.*, 2007, **19**, 4811–4819.

128 X. Fan, T. Yu, Y. Wang, J. Zheng, L. Gao, Z. Li, J. Ye and Z. Zou, *Appl. Surf. Sci.*, 2008, **254**, 5191–5198.

129 A. V. Akimov, A. J. Neukirch and O. V. Prezhdo, *Chem. Rev.*, 2013, **113**, 4496–4565.

130 N. O. Gopal, H.-H. Lo, T.-F. Ke, C.-H. Lee, C.-C. Chou, J.-D. Wu, S.-C. Sheu and S.-C. Ke, *J. Phys. Chem. C*, 2012, **116**, 16191–16197.

131 S. A. Ansari and M. H. Cho, *Sci. Rep.*, 2016, **6**, 25405.

132 T. Ohno, M. Akiyoshi, T. Umebayashi, K. Asai, T. Mitsui and M. Matsumura, *Appl. Catal., A*, 2004, **265**, 115–121.

133 T. Umebayashi, T. Yamaki, H. Itoh and K. Asai, *Appl. Phys. Lett.*, 2002, **81**, 454–456.

134 F. Wang, F. Li, L. Zhang, H. Zeng, Y. Sun, S. Zhang and X. Xu, *Mater. Res. Bull.*, 2017, **87**, 20–26.

135 V. V. Pillai, S. P. Lonkar and S. M. Alhassan, *ACS Omega*, 2020, **5**, 7969–7978.

136 C. Yi, Q. Liao, W. Deng, Y. Huang, J. Mao, B. Zhang and G. Wu, *Sci. Total Environ.*, 2019, **684**, 527–536.

137 T. Boningari, S. N. R. Inturi, M. Suidan and P. G. Smirniotis, *J. Chem. Eng.*, 2018, **339**, 249–258.

138 S. A. Bakar and C. Ribeiro, *J. Mol. Catal. A: Chem.*, 2016, **421**, 1–15.

139 Y. Niu, M. Xing, B. Tian and J. Zhang, *Appl. Catal., B*, 2012, **115–116**, 253–260.

140 D. Ma, Y. Xin, M. Gao and J. Wu, *Appl. Catal., B*, 2014, **147**, 49–57.

141 W. Q. Fang, X. L. Wang, H. Zhang, Y. Jia, Z. Huo, Z. Li, H. Zhao, H. G. Yang and X. Yao, *J. Mater. Chem. A*, 2014, **2**, 3513.

142 M. Bellardita, C. Garlisi, A. M. Venezia, G. Palmisano and L. Palmisano, *Catal. Sci. Technol.*, 2018, **8**, 1606–1620.

143 X. Kang, X. Z. Song, Y. Han, J. Cao and Z. Tan, *Sci. Rep.*, 2018, **8**, 5904.

144 Q. Wang, B. Rhimi, H. Wang and C. Wang, *Appl. Surf. Sci.*, 2020, **530**, 147286.

145 F. Zuo, L. Wang, T. Wu, Z. Zhang, D. Borchardt and P. Feng, *J. Am. Chem. Soc.*, 2010, **132**, 11856–11857.

146 H. G. Yang, C. H. Sun, S. Z. Qiao, J. Zou, G. Liu, S. C. Smith, H. M. Cheng and G. Q. Lu, *Nature*, 2008, **453**, 638–641.

147 A. S. Ichimura, B. Mack, S. M. Usmani and D. Mars, *Chem. Mater.*, 2012, **24**, 2324–2329.

148 X. Liu, G. Du and M. Li, *ACS Omega*, 2019, **4**, 14902–14912.

149 G. Liu, H. G. Yang, J. Pan, Y. Q. Yang, G. Q. Lu and H. M. Cheng, *Chem. Rev.*, 2014, **114**, 9559–9612.

150 Y. Cao, Q. Li, C. Li, J. Li and J. Yang, *Appl. Catal., B*, 2016, **198**, 378–388.

151 Y. Dong, M. Kapilashrami, Y. Zhang and J. Guo, *CrystEngComm*, 2013, **15**, 10657.

152 S. Sarina, E. R. Waclawik and H. Zhu, *Green Chem.*, 2013, **15**, 1814.

153 X. C. Ma, Y. Dai, L. Yu and B. B. Huang, *Light: Sci. Appl.*, 2016, **5**, e16017.

154 X. Zhang, Y. L. Chen, R. S. Liu and D. P. Tsai, *Rep. Prog. Phys.*, 2013, **76**, 046401.

155 S. T. Kochuveedu, Y. H. Jang and D. H. Kim, *Chem. Soc. Rev.*, 2013, **42**, 8467–8493.

156 K. Awazu, M. Fujimaki, C. Rockstuhl, J. Tominaga, H. Murakami, Y. Ohki, N. Yoshida and T. Watanabe, *J. Am. Chem. Soc.*, 2008, **130**, 1676–1680.

157 R. Asapu, N. Claes, S. Bals, S. Denys, C. Detavernier, S. Lenaerts and S. W. Verbruggen, *Appl. Catal., B*, 2017, **200**, 31–38.

158 H. Chakhtouna, H. Benzeid, N. Zari, A. E. K. Qaiss and R. Bouhfid, *Environ. Sci. Pollut. Res. Int.*, 2021, **28**, 44638–44666.

159 Z. Wei, L. Rosa, K. Wang, M. Endo, S. Juodkazis, B. Ohtani and E. Kowalska, *Appl. Catal., B*, 2017, **206**, 393–405.

160 R. Asapu, N. Claes, R.-G. Ciocarlan, M. Minjauw, C. Detavernier, P. Cool, S. Bals and S. W. Verbruggen, *ACS Appl. Nano Mater.*, 2019, **2**, 4067–4074.

161 S. Liu, M. D. Regulacio, S. Y. Tee, Y. W. Khin, C. P. Teng, L. D. Koh, G. Guan and M. Y. Han, *Chem. Rec.*, 2016, **16**, 1965–1990.

162 R. Kaur and B. Pal, *J. Mol. Catal. A: Chem.*, 2012, **355**, 39–43.

163 D. Tsukamoto, Y. Shiraishi, Y. Sugano, S. Ichikawa, S. Tanaka and T. Hirai, *J. Am. Chem. Soc.*, 2012, **134**, 6309–6315.

164 Š. Slapničar, G. Žerjav, J. Zavašnik, M. Finšgar and A. Pintar, *J. Environ. Chem. Eng.*, 2023, **11**, 109835.

165 Z. Guo, G. Yu, Z. Zhang, Y. Han, G. Guan, W. Yang and M. Y. Han, *Adv. Mater.*, 2023, **35**, e2206700.

166 T. Akiyama, H. Nagakawa and T. Tatsuma, *Phys. Chem. Chem. Phys.*, 2023, **25**, 9031–9035.

167 M. Gao, L. Zhu, W. L. Ong, J. Wang and G. W. Ho, *Catal. Sci. Technol.*, 2015, **5**, 4703–4726.

168 N. Celebi, M. Y. Aydin, F. Soysal, Y. O. Ciftci and K. Salimi, *J. Alloys Compd.*, 2021, **860**, 157908.

169 J. Li, L. Zu, Y. Li, C. Jin, Y. Qin, D. Shi and J. Yang, *J. Colloid Interface Sci.*, 2014, **426**, 90–98.

170 S. Zhao, H.-X. Liu, Y. Qiu, S.-Q. Liu, J.-X. Diao, C.-R. Chang, R. Si and X.-H. Guo, *J. Mater. Chem. A*, 2020, **8**, 6586–6596.

171 Z. W. Seh, S. Liu, S. Y. Zhang, M. S. Bharathi, H. Ramanarayan, M. Low, K. W. Shah, Y. W. Zhang and M. Y. Han, *Angew. Chem., Int. Ed.*, 2011, **50**, 10140–10143.

172 A. Zada, P. Muhammad, W. Ahmad, Z. Hussain, S. Ali, M. Khan, Q. Khan and M. Maqbool, *Adv. Funct. Mater.*, 2019, **30**, 1906744.

173 J. Yang, X. Chen, X. Yang and J. Y. Ying, *Energy Environ. Sci.*, 2012, **5**, 8976.

174 G. Guisbiers, S. Mejia-Rosales, S. Khanal, F. Ruiz-Zepeda, R. L. Whetten and M. Jose-Yacaman, *Nano Lett.*, 2014, **14**, 6718–6726.

175 G. Darabdhara, B. Sharma, M. R. Das, R. Boukherroub and S. Szunerits, *Sens. Actuators, B*, 2017, **238**, 842–851.

176 S. Kunwar, P. Pandey and J. Lee, *ACS Omega*, 2019, **4**, 17340–17351.

177 M. Sui, S. Kunwar, P. Pandey and J. Lee, *Sci. Rep.*, 2019, **9**, 16582.

178 H. Yu, Y. Peng, Y. Yang and Z.-Y. Li, *npj Comput. Mater.*, 2019, **5**, 45.

179 S. W. Verbruggen, M. Keulemans, M. Filippousi, D. Flahaut, G. Van Tendeloo, S. Lacombe, J. A. Martens and S. Lenaerts, *Appl. Catal., B*, 2014, **156–157**, 116–121.

180 M. Zhu, Y. Wang, Y. H. Deng, X. Peng, X. Wang, H. Yuan, Z. J. Yang, Y. Wang and H. Wang, *Nanoscale*, 2020, **12**, 7035–7044.

181 P. Reñones, L. Collado, A. Iglesias-Juez, F. E. Oropeza, F. Fresno and V. A. de la Peña O'Shea, *Ind. Eng. Chem. Res.*, 2020, **59**, 9440–9450.

182 D. Tsukamoto, A. Shiro, Y. Shiraishi, Y. Sugano, S. Ichikawa, S. Tanaka and T. Hirai, *ACS Catal.*, 2012, **2**, 599–603.

183 R. Su, L. Kesavan, M. M. Jensen, R. Tiruvalam, Q. He, N. Dimitratos, S. Wendt, M. Glasius, C. J. Kiely, G. J. Hutchings and F. Besenbacher, *Chem. Commun.*, 2014, **50**, 12612–12614.

184 S. Shuang, R. Lv, Z. Xie and Z. Zhang, *Sci. Rep.*, 2016, **6**, 26670.

185 W. Guo, Y. Liu, Y. Sun, Y. Wang, W. Qin, B. Zhao, Z. Liang and L. Jiang, *Adv. Funct. Mater.*, 2021, **31**, 2100768.

186 H. Nishi, T. Torimoto and T. Tatsuma, *Phys. Chem. Chem. Phys.*, 2015, **17**, 4042–4046.

187 S. Wang, L. Pan, J. J. Song, W. Mi, J. J. Zou, L. Wang and X. Zhang, *J. Am. Chem. Soc.*, 2015, **137**, 2975–2983.

188 X. Liu, G. Zhu, X. Wang, X. Yuan, T. Lin and F. Huang, *Adv. Energy Mater.*, 2016, **6**, 1600452.

189 W. Zhang, H. He, Y. Tian, H. Li, K. Lan, L. Zu, Y. Xia, L. Duan, W. Li and D. Zhao, *Nano Energy*, 2019, **66**, 104113.

190 R. Fernández-Climent, S. Giménez and M. García-Tecedor, *Sustainable Energy Fuels*, 2020, **4**, 5916–5926.

191 F. Yu, C. Wang, Y. Li, H. Ma, R. Wang, Y. Liu, N. Suzuki, C. Terashima, B. Ohtani, T. Ochiai, A. Fujishima and X. Zhang, *Adv. Sci.*, 2020, **7**, 2000204.

192 W. Hu, W. Zhou, K. Zhang, X. Zhang, L. Wang, B. Jiang, G. Tian, D. Zhao and H. Fu, *J. Mater. Chem. A*, 2016, **4**, 7495–7502.

193 T. S. Rajaraman, S. P. Parikh and V. G. Gandhi, *J. Chem. Eng.*, 2020, **389**, 123918.

194 H. Song, C. Li, Z. Lou, Z. Ye and L. Zhu, *ACS Sustainable Chem. Eng.*, 2017, **5**, 8982–8987.

195 L. Andronic and A. Enesca, *Front. Chem.*, 2020, **8**, 565489.

196 X. Chen, L. Liu and F. Huang, *Chem. Soc. Rev.*, 2015, **44**, 1861–1885.

197 L. Gu, J. Wang, H. Cheng, Y. Zhao, L. Liu and X. Han, *ACS Appl. Mater. Interfaces*, 2013, **5**, 3085–3093.

198 C. Peng, X. Yang, Y. Li, H. Yu, H. Wang and F. Peng, *ACS Appl. Mater. Interfaces*, 2016, **8**, 6051–6060.

199 L. L. Tan, W. J. Ong, S. P. Chai and A. R. Mohamed, *Nanoscale Res. Lett.*, 2013, **8**, 465.

200 I.-A. Baragau, J. Buckeridge, K. G. Nguyen, T. Heil, M. T. Sajjad, S. A. J. Thomson, A. Rennie, D. J. Morgan, N. P. Power, S. A. Nicolae, M.-M. Titirici, S. Dunn and S. Kellici, *J. Mater. Chem. A*, 2023, **11**, 9791–9806.

201 X. Zhou, Y. Fang, X. Cai, S. Zhang, S. Yang, H. Wang, X. Zhong and Y. Fang, *ACS Appl. Mater. Interfaces*, 2020, **12**, 20579–20588.

202 W. J. Ong, L. L. Tan, Y. H. Ng, S. T. Yong and S. P. Chai, *Chem. Rev.*, 2016, **116**, 7159–7329.

203 X. Wang, K. Maeda, A. Thomas, K. Takanabe, G. Xin, J. M. Carlsson, K. Domen and M. Antonietti, *Nat. Mater.*, 2009, **8**, 76–80.

204 D. Zeng, W.-J. Ong, H. Zheng, M. Wu, Y. Chen, D.-L. Peng and M.-Y. Han, *J. Mater. Chem. A*, 2017, **5**, 16171–16178.

205 D. Zeng, W. J. Ong, Y. Chen, S. Y. Tee, C. S. Chua, D. L. Peng and M. Y. Han, *Part. Syst. Charact.*, 2017, **35**, 1700251.

206 T. Hong, S. Anwer, J. Wu, C. Deng and H. Qian, *Front. Chem.*, 2022, **10**, 1050046.

207 M. Ghidiu, M. R. Lukatskaya, M. Q. Zhao, Y. Gogotsi and M. W. Barsoum, *Nature*, 2014, **516**, 78–81.

208 Y. Li, X. Deng, J. Tian, Z. Liang and H. Cui, *Appl. Mater. Today*, 2018, **13**, 217–227.

209 C. J. Zhang, S. Pinilla, N. McEvoy, C. P. Cullen, B. Anasori, E. Long, S.-H. Park, A. Seral-Ascaso, A. Shmeliov, D. Krishnan, C. Morant, X. Liu, G. S. Duesberg, Y. Gogotsi and V. Nicolosi, *Chem. Mater.*, 2017, **29**, 4848–4856.

210 A. Shahzad, K. Rasool, M. Nawaz, W. Miran, J. Jang, M. Moztahida, K. A. Mahmoud and D. S. Lee, *Chem. Eng. J.*, 2018, **349**, 748–755.

211 A. Crake, K. C. Christoforidis, A. Kafizas, S. Zafeiratos and C. Petit, *Appl. Catal., B*, 2017, **210**, 131–140.

212 A. P. Cote, A. I. Benin, N. W. Ockwig, M. O'Keeffe, A. J. Matzger and O. M. Yaghi, *Science*, 2005, **310**, 1166–1170.

213 T. Banerjee, K. Gottschling, G. Savasci, C. Ochsenfeld and B. V. Lotsch, *ACS Energy Lett.*, 2018, **3**, 400–409.

214 Y. Cai, Y. Yu, J. Wu, J. Qu, J. Hu, D. Tian and J. Li, *Nanoscale*, 2024, **16**, 961–977.

215 S. Y. Ding and W. Wang, *Chem. Soc. Rev.*, 2013, **42**, 548–568.

216 J. Qu, T. Yang, P. Zhang, F. Yang, Y. Cai, X. Yang, C. M. Li and J. Hu, *Appl. Catal., B*, 2024, **348**, 123827.

217 J. Hao, Y. Tang, J. Qu, Y. Cai, X. Yang and J. Hu, *Small*, 2024, 2404139.

218 H. Li, H. Liu, C. Li, J. Liu, J. Liu and Q. Yang, *J. Mater. Chem. A*, 2020, **8**, 18745–18754.

219 X. Han, W. Dong, L. Li and X. Zhou, *Chem. Commun.*, 2023, **59**, 11863–11866.

220 A. Putta Rangappa, D. Praveen Kumar, K. H. Do, J. Wang, Y. Zhang and T. K. Kim, *Adv. Sci.*, 2023, **10**, e2300073.

221 P. Sarkar, I. H. Chowdhury, A. Chakraborty, M. Goswami, M. K. Naskar, A. Khan and S. M. Islam, *Ind. Eng. Chem. Res.*, 2024, **63**, 5591–5607.

222 A. L. Luna, F. Matter, M. Schreck, J. Wohlwend, E. Tervoort, C. Colbeau-Justin and M. Niederberger, *Appl. Catal., B*, 2020, **267**, 118660.

223 Y. Si, J. Yu, X. Tang, J. Ge and B. Ding, *Nat. Commun.*, 2014, **5**, 5802.

224 W. Liu, A. K. Herrmann, N. C. Bigall, P. Rodriguez, D. Wen, M. Oezaslan, T. J. Schmidt, N. Gaponik and A. Eychmuller, *Acc. Chem. Res.*, 2015, **48**, 154–162.

225 P. Rusch, D. Zambo and N. C. Bigall, *Acc. Chem. Res.*, 2020, **53**, 2414–2424.

226 A. Rose, A. Hofmann, P. Voepel, B. Milow and R. Marschall, *ACS Appl. Energy Mater.*, 2022, **5**, 14966–14978.

227 Y. Nosaka and A. Y. Nosaka, *Chem. Rev.*, 2017, **117**, 11302–11336.

228 Z. Liu, S. Y. Tee, G. Guan and M. Y. Han, *Nanomicro Lett.*, 2024, **16**, 95.

229 J. Hu, D. Chen, Z. Mo, N. Li, Q. Xu, H. Li, J. He, H. Xu and J. Lu, *Angew. Chem., Int. Ed.*, 2019, **58**, 2073–2077.

230 N. Serpone, P. Maruthamuthu, P. Pichat, E. Pelizzetti and H. Hidaka, *J. Photochem. Photobiol., A*, 1995, **85**, 247–255.

231 I. Bedja and P. V. Kamat, *J. Phys. Chem.*, 2002, **99**, 9182–9188.

232 H. Li, W. Tu, Y. Zhou and Z. Zou, *Adv. Sci.*, 2016, **3**, 1500389.

233 K. Maeda, *ACS Catal.*, 2013, **3**, 1486–1503.

234 Q. Xu, L. Zhang, B. Cheng, J. Fan and J. Yu, *Chem*, 2020, **6**, 1543–1559.

235 P. Zhou, J. Yu and M. Jaroniec, *Adv. Mater.*, 2014, **26**, 4920–4935.

236 W. Yu, S. Zhang, J. Chen, P. Xia, M. H. Richter, L. Chen, W. Xu, J. Jin, S. Chen and T. Peng, *J. Mater. Chem. A*, 2018, **6**, 15668–15674.

237 J. Low, B. Dai, T. Tong, C. Jiang and J. Yu, *Adv. Mater.*, 2019, **31**, e1802981.

238 Q. Xu, L. Zhang, J. Yu, S. Wageh, A. A. Al-Ghamdi and M. Jaroniec, *Mater. Today*, 2018, **21**, 1042–1063.

239 G. Yang, D. Chen, H. Ding, J. Feng, J. Z. Zhang, Y. Zhu, S. Hamid and D. W. Bahnemann, *Appl. Catal., B*, 2017, **219**, 611–618.

240 U. S. Meda, K. Vora, Y. Athreya and U. A. Mandi, *Process Saf. Environ. Prot.*, 2022, **161**, 771–787.

241 M. E. Aguirre, R. Zhou, A. J. Eugene, M. I. Guzman and M. A. Grela, *Appl. Catal., B*, 2017, **217**, 485–493.

242 Y. Li, Z. Xia, Q. Yang, L. Wang and Y. Xing, *J. Mater. Sci. Technol.*, 2022, **125**, 128–144.

243 F. Xu, K. Meng, B. Cheng, S. Wang, J. Xu and J. Yu, *Nat. Commun.*, 2020, **11**, 4613.

244 R. P. Schwarzenbach, T. Egli, T. B. Hofstetter, U. von Gunten and B. Wehrli, *Annu. Rev. Environ. Resour.*, 2010, **35**, 109–136.

245 D. Antonio da Silva, R. P. Cavalcante, R. F. Cunha, A. J. Machulek and S. Cesar de Oliveira, *Chemosphere*, 2018, **207**, 457–468.

246 M. Ahmed, M. O. Mavukkandy, A. Giwa, M. Elektorowicz, E. Katsou, O. Khelifi, V. Naddeo and S. W. Hasan, *npj Clean Water*, 2022, **5**, 12.

247 J. Giménez, B. Bayarri, Ó. González, S. Malato, J. Peral and S. Esplugas, *ACS Sustainable Chem. Eng.*, 2015, **3**, 3188–3196.

248 A. R. Khataee and M. Fathinia, *Recent Advances in Photocatalytic Processes by Nanomaterials*, 2013.

249 S. Foteinis and E. Chatzisymeon, *Nanostruct. Photocatal.*, 2020, 75–97.

250 C. Hu, X. Zhang, W. Li, Y. Yan, G. Xi, H. Yang, J. Li and H. Bai, *J. Mater. Chem. A*, 2014, **2**, 2040.

251 W. Wang, J. Fang, Y. Zhou, W. Zhang and C. Lu, *RSC Adv.*, 2016, **6**, 67556–67564.

252 S. S. Alias, Z. Harun, F. H. Azhar, S. A. Ibrahim and B. Johar, *J. Cleaner Prod.*, 2020, **251**, 119448.

253 T. Rajaramanan, S. Shanmugaratnam, V. Gurunanthanan, S. Yohi, D. Velauthapillai, P. Ravirajan and M. Senthilnanthanan, *Catalysts*, 2021, **11**, 690.

254 M. K. Hossain, M. M. Hossain and S. Akhtar, *ACS Omega*, 2023, **8**, 1979–1988.

255 L. Elsellami, H. Lachheb and A. Houas, *Mater. Sci. Semicond. Process.*, 2015, **36**, 103–114.

256 A. Khlyustova, N. Sirotkin, T. Kusova, A. Kraev, V. Titov and A. Agafonov, *Mater. Adv.*, 2020, **1**, 1193–1201.

257 L. Bergamonti, G. Predieri, Y. Paz, L. Fornasini, P. P. Lottici and F. Bondioli, *Microchem. J.*, 2017, **133**, 1–12.

258 J. Niu, P. Lu, M. Kang, K. Deng, B. Yao, X. Yu and Q. Zhang, *Appl. Surf. Sci.*, 2014, **319**, 99–106.

259 T. Ohno, M. Akiyoshi, T. Umebayashi, K. Asai, T. Mitsui and M. Matsumura, *Appl. Catal., A*, 2004, **265**, 115–121.

260 T. Liu, B. Li, Y. Hao, F. Han, L. Zhang and L. Hu, *Appl. Catal., B*, 2015, **165**, 378–388.

261 X. Yang, Y. Wang, L. Zhang, H. Fu, P. He, D. Han, T. Lawson and X. An, *Catalysts*, 2020, **10**, 139.

262 E. D. Sultanova, I. R. Nizameev, K. V. Kholin, M. K. Kadirov, A. S. Ovsyannikov, V. A. Burilov, A. Y. Ziganshina and I. S. Antipin, *New J. Chem.*, 2020, **44**, 7169–7174.

263 C. H. Nguyen, C.-C. Fu and R.-S. Juang, *J. Cleaner Prod.*, 2018, **202**, 413–427.

264 C. Jia, X. Zhang, K. Matras-Postolek, B. Huang and P. Yang, *Carbon*, 2018, **139**, 415–426.

265 C. Xue, T. Zhang, S. Ding, J. Wei and G. Yang, *ACS Appl. Mater. Interfaces*, 2017, **9**, 16091–16102.

266 V. Q. Nguyen, A. H. Mady, M. A. Mahadadalkar, M. L. Baynosa, D. R. Kumar, A. M. Rabie, J. Lee, W. K. Kim and J. J. Shim, *J. Colloid Interface Sci.*, 2022, **606**, 337–352.

267 R. Khunphonoi and N. Grisdanurak, *Chem. Eng. J.*, 2016, **296**, 420–427.

268 A. M. Alotaibi, S. Sathasivam, B. A. D. Williamson, A. Kafizas, C. Sotelo-Vazquez, A. Taylor, D. O. Scanlon and I. P. Parkin, *Chem. Mater.*, 2018, **30**, 1353–1361.

269 R. Su, R. Tiruvalam, Q. He, N. Dimitratos, L. Kesavan, C. Hammond, J. A. Lopez-Sanchez, R. Bechstein, C. J. Kiely, G. J. Hutchings and F. Besenbacher, *ACS Nano*, 2012, **6**, 6284–6292.

270 Y. Zhang, Q. Li, Q. Gao, S. Wan, P. Yao and X. Zhu, *Appl. Catal., B*, 2020, **267**, 118715.

271 D. H. Quiñones, A. Rey, P. M. Álvarez, F. J. Beltrán and G. Li Puma, *Appl. Catal., B*, 2015, **178**, 74–81.

272 R. M. Mohamed and Z. I. Zaki, *J. Environ. Chem. Eng.*, 2021, **9**, 104732.

273 R. Fiorenza, A. Di Mauro, M. Cantarella, V. Privitera and G. Impellizzeri, *J. Photochem. Photobiol., A*, 2019, **380**, 111872.

274 R. Fiorenza, A. Di Mauro, M. Cantarella, C. Iaria, E. M. Scalisi, M. V. Brundo, A. Gulino, L. Spitaleri,

G. Nicotra, S. Dattilo, S. C. Carroccio, V. Privitera and G. Impellizzeri, *J. Chem. Eng.*, 2020, **379**, 122309.

275 E. Bilgin Simsek, *Appl. Catal., B*, 2017, **200**, 309–322.

276 R. P. Cavalcante, R. F. Dantas, B. Bayarri, O. González, J. Giménez, S. Esplugas and A. Machulek, *Catal. Today*, 2015, **252**, 27–34.

277 X. Feng, P. Wang, J. Hou, J. Qian, Y. Ao and C. Wang, *J. Hazard. Mater.*, 2018, **351**, 196–205.

278 R. Yu, Y. Yang, Z. Zhou, X. Li, J. Gao, N. Wang, J. Li and Y. Liu, *Sep. Purif. Technol.*, 2022, **299**, 121712.

279 K. Hu, R. Li, C. Ye, A. Wang, W. Wei, D. Hu, R. Qiu and K. Yan, *J. Cleaner Prod.*, 2020, **253**, 120055.

280 S. Varnagiris, M. Urbonavicius, S. Sakalauskaite, R. Daugelavicius, L. Pranevicius, M. Lelis and D. Milcius, *Sci. Total Environ.*, 2020, **720**, 137600.

281 Y. Ren, Y. Han, Z. Li, X. Liu, S. Zhu, Y. Liang, K. W. K. Yeung and S. Wu, *Bioact. Mater.*, 2020, **5**, 201–209.

282 S. Zhu, X. Xie, S.-C. Chen, S. Tong, G. Lu, D. Y. H. Pui and J. Sun, *Appl. Surf. Sci.*, 2017, **408**, 117–124.

283 X. Gao, K. Zheng, Q. Zhang, X. Cao, S. Wu and J. Su, *Appl. Surf. Sci.*, 2022, **586**, 152882.

284 S. Y. Tee, C. J. Lee, S. S. Dinachali, S. C. Lai, E. L. Williams, H. K. Luo, D. Chi, T. S. Andy Hor and M. Y. Han, *Nanotechnology*, 2015, **26**, 415401.

285 F. Yang, P. Wang, J. Hao, J. Qu, Y. Cai, X. Yang, C. M. Li and J. Hu, *Nano Energy*, 2023, **118**, 108993.

286 E. H. G. Backus, S. Hosseinpour, C. Ramanan, S. Sun, S. J. Schlegel, M. Zelenka, X. Jia, M. Gebhard, A. Devi, H. I. Wang and M. Bonn, *Angew. Chem., Int. Ed.*, 2024, **63**, e202312123.

287 J. Low, J. Yu, M. Jaroniec, S. Wageh and A. A. Al-Ghamdi, *Adv. Mater.*, 2017, **29**, 1601694.

288 M. Ge, Q. Li, C. Cao, J. Huang, S. Li, S. Zhang, Z. Chen, K. Zhang, S. S. Al-Deyab and Y. Lai, *Adv. Sci.*, 2017, **4**, 1600152.

289 J. Hu, S. Zhang, Y. Cao, H. Wang, H. Yu and F. Peng, *ACS Sustainable Chem. Eng.*, 2018, **6**, 10823–10832.

290 P. Wang, Q. Zhou, Y. Xia, S. Zhan and Y. Li, *Appl. Catal., B*, 2018, **225**, 433–444.

291 H. Li, Z. Bian, J. Zhu, D. Zhang, G. Li, Y. Huo, H. Li and Y. Lu, *J. Am. Chem. Soc.*, 2007, **129**, 8406–8407.

292 W. Cao, B. Wei, X. Fu, N. Ma, H. Gao and L. Xu, *RSC Adv.*, 2016, **6**, 108969–108973.

293 S. Navalon, A. Dhakshinamoorthy, M. Alvaro, B. Ferrer and H. Garcia, *Chem. Rev.*, 2023, **123**, 445–490.

294 S. Kampouri, C. P. Ireland, B. Valizadeh, E. Oveisi, P. A. Schouwink, M. Mensi and K. C. Stylianou, *ACS Appl. Energy Mater.*, 2018, **1**, 6541–6548.

295 X. He, Y. Ding, Z. Huang, M. Liu, M. Chi, Z. Wu, C. U. Segre, C. Song, X. Wang and X. Guo, *Angew. Chem., Int. Ed.*, 2023, **62**, e202217439.

296 Z.-H. Xue, D. Luan, H. Zhang and X. W. Lou, *Joule*, 2022, **6**, 92–133.

297 B. Xing, T. Wang, Z. Zheng, S. Liu, J. Mao, C. Li and B. Li, *Chem. Eng. J.*, 2023, **461**, 141871.

298 B. Lu, L. Guo, F. Wu, Y. Peng, J. E. Lu, T. J. Smart, N. Wang, Y. Z. Finfrock, D. Morris, P. Zhang, N. Li, P. Gao, Y. Ping and S. Chen, *Nat. Commun.*, 2019, **10**, 631.

299 B. Yan, D. Liu, X. Feng, M. Shao and Y. Zhang, *Adv. Funct. Mater.*, 2020, **30**, 2003007.

300 J. Kwon, K. Choi, M. Schreck, T. Liu, E. Tervoort and M. Niederberger, *ACS Appl. Mater. Interfaces*, 2021, **13**, 53691–53701.

301 Z. Li and X. Meng, *J. Alloys Compd.*, 2020, **830**, 154669.

302 J. Kwon, K. Choi, E. Tervoort and M. Niederberger, *J. Mater. Chem. A*, 2022, **10**, 18383–18395.

303 G. Bersalli, T. Trondle and J. Lilliestam, *Commun. Earth Environ.*, 2023, **4**, 44.

304 V. Kumaravel, J. Bartlett and S. C. Pillai, *ACS Energy Lett.*, 2020, **5**, 486–519.

305 S. A. Rawool, K. K. Yadav and V. Polshettiwar, *Chem. Sci.*, 2021, **12**, 4267–4299.

306 Y. Wei, F. You, D. Zhao, J. Wan, L. Gu and D. Wang, *Angew. Chem., Int. Ed.*, 2022, **61**, e202212049.

307 W. Jiang, H. Loh, B. Q. L. Low, H. Zhu, J. Low, J. Z. X. Heng, K. Y. Tang, Z. Li, X. J. Loh, E. Ye and Y. Xiong, *Appl. Catal., B*, 2023, **321**, 122079.

308 C. Ban, Y. Wang, Y. Feng, Z. Zhu, Y. Duan, J. Ma, X. Zhang, X. Liu, K. Zhou, H. Zou, D. Yu, X. Tao, L. Gan, G. Han and X. Zhou, *Energy Environ. Sci.*, 2024, **17**, 518–530.

309 A. Crake, K. C. Christoforidis, A. Gregg, B. Moss, A. Kafizas and C. Petit, *Small*, 2019, **15**, e1805473.

310 S. Wang, M. Xu, T. Peng, C. Zhang, T. Li, I. Hussain, J. Wang and B. Tan, *Nat. Commun.*, 2019, **10**, 676.

311 Y. Ma, X. Yi, S. Wang, T. Li, B. Tan, C. Chen, T. Majima, E. R. Waclawik, H. Zhu and J. Wang, *Nat. Commun.*, 2022, **13**, 1400.

312 Y. Yu, X. Dong, P. Chen, Q. Geng, H. Wang, J. Li, Y. Zhou and F. Dong, *ACS Nano*, 2021, **15**, 14453–14464.

313 Y. Xu, S. Wang, J. Yang, B. Han, R. Nie, J. Wang, J. Wang and H. Jing, *Nano Energy*, 2018, **51**, 442–450.

314 S. Kreft, R. Schoch, J. Schneidewind, J. Rabeah, E. V. Kondratenko, V. A. Kondratenko, H. Junge, M. Bauer, S. Wohlrab and M. Beller, *Chem*, 2019, **5**, 1818–1833.

315 L. Liang, C. Liu, F. Jiang, Q. Chen, L. Zhang, H. Xue, H. L. Jiang, J. Qian, D. Yuan and M. Hong, *Nat. Commun.*, 2017, **8**, 1233.

316 L. Liang, C. Liu, F. Jiang, Q. Chen, L. Zhang, H. Xue, H. L. Jiang, J. Qian, D. Yuan and M. Hong, *Nat. Commun.*, 2017, **8**, 1233.

317 R. Li, J. Hu, M. Deng, H. Wang, X. Wang, Y. Hu, H. L. Jiang, J. Jiang, Q. Zhang, Y. Xie and Y. Xiong, *Adv. Mater.*, 2014, **26**, 4783–4788.

318 S. Yan, S. Ouyang, H. Xu, M. Zhao, X. Zhang and J. Ye, *J. Mater. Chem. A*, 2016, **4**, 15126–15133.

319 Z. Jiang, X. Xu, Y. Ma, H. S. Cho, D. Ding, C. Wang, J. Wu, P. Oleynikov, M. Jia, J. Cheng, Y. Zhou, O. Terasaki, T. Peng, L. Zan and H. Deng, *Nature*, 2020, **586**, 549–554.

320 J. Bian, Z. Zhang, J. Feng, M. Thangamuthu, F. Yang, L. Sun, Z. Li, Y. Qu, D. Tang, Z. Lin, F. Bai, J. Tang and L. Jing, *Angew. Chem., Int. Ed.*, 2021, **60**, 20906–20914.
321 G. N. Schrauzer and T. D. Guth, *J. Am. Chem. Soc.*, 1977, **99**, 7189–7193.
322 P. W. Huang and M. C. Hatzell, *Nat. Commun.*, 2022, **13**, 7908.
323 C. J. van der Ham, M. T. Koper and D. G. Hetterscheid, *Chem. Soc. Rev.*, 2014, **43**, 5183–5191.
324 S. Chen, D. Liu and T. Peng, *Sol. RRL*, 2020, **5**, 2000487.
325 G. Zhang, X. Yang, C. He, P. Zhang and H. Mi, *J. Mater. Chem. A*, 2020, **8**, 334–341.
326 J. Qian, S. Zhao, W. Dang, Y. Liao, W. Zhang, H. Wang, L. Lv, L. Luo, H. Y. Jiang and J. Tang, *Adv. Sustainable Syst.*, 2021, **5**, 2000282.
327 Q. Liu, L. Ai and J. Jiang, *J. Mater. Chem. A*, 2018, **6**, 4102–4110.
328 S. Liu, Y. Wang, S. Wang, M. You, S. Hong, T.-S. Wu, Y.-L. Soo, Z. Zhao, G. Jiang, Q. Jieshan, B. Wang and Z. Sun, *ACS Sustainable Chem. Eng.*, 2019, **7**, 6813–6820.
329 L. Chen, J. Shou, Y. Chen, W. Han, X. Tu, L. Zhang, Q. Sun, J. Cao, Y. Chang and H. Zheng, *Chem. Eng. J.*, 2023, **451**, 138592.
330 J. Wang, W. Lin, Y. Ran, J. Cui, L. Wang, X. Yu and Y. Zhang, *J. Phys. Chem. C*, 2019, **124**, 1253–1259.
331 Y. Tang, C. Asokan, M. Xu, G. W. Graham, X. Pan, P. Christopher, J. Li and P. Sautet, *Nat. Commun.*, 2019, **10**, 4488.
332 W. Li, A. Elzatahry, D. Aldhayan and D. Zhao, *Chem. Soc. Rev.*, 2018, **47**, 8203–8237.
333 C. Samanta, *Appl. Catal., A*, 2008, **350**, 133–149.
334 G. Gao, Y. Tian, X. Gong, Z. Pan, K. Yang and B. Zong, *Chin. J. Catal.*, 2020, **41**, 1039–1047.
335 J. Liu, Y. Zou, B. Jin, K. Zhang and J. H. Park, *ACS Energy Lett.*, 2019, **4**, 3018–3027.
336 J. S. J. Hargreaves, Y.-M. Chung, W.-S. Ahn, T. Hisatomi, K. Domen, M. C. Kung and H. H. Kung, *Appl. Catal., A*, 2020, **594**, 117419.
337 H. Hou, X. Zeng and X. Zhang, *Angew. Chem., Int. Ed.*, 2020, **59**, 17356–17376.
338 Y. Zhao, Y. Kondo, Y. Kuwahara, K. Mori and H. Yamashita, *Catal. Today*, 2024, **425**, 114350.
339 W. Gan, X. Fu, J. Jin, J. Guo, M. Zhang, R. Chen, C. Ding, Y. Lu, J. Li and Z. Sun, *J. Colloid Interface Sci.*, 2024, **653**, 1028–1039.
340 Z. Jiang, Q. Long, B. Cheng, R. He and L. Wang, *J. Mater. Process. Technol.*, 2023, **162**, 1–10.
341 X. Sun, T. Wang, C. Wang and T. Ohno, *Catal. Sci. Technol.*, 2023, **13**, 6799–6811.
342 Y. Yang, J. Liu, M. Gu, B. Cheng, L. Wang and J. Yu, *Appl. Catal., B*, 2023, **333**, 122780.
343 X. Bao, H. Li, Z. Wang, F. Tong, M. Liu, Z. Zheng, P. Wang, H. Cheng, Y. Liu, Y. Dai, Y. Fan, Z. Li and B. Huang, *Appl. Catal., B*, 2021, **286**, 119885.
344 Z. Shen, Y. Hu, B. Li, Y. Zou, S. Li, G. Wilma Busser, X. Wang, G. Zhao and M. Muhler, *J. Energy Chem.*, 2021, **62**, 338–350.
345 C. Courtois, M. Eder, K. Schnabl, C. A. Walenta, M. Tschurl and U. Heiz, *Angew. Chem., Int. Ed.*, 2019, **58**, 14255–14259.
346 G. S. Wolde, D.-H. Kuo, M. H. Urgesa and T. N. Gemeda, *Chem. Eng. J.*, 2023, **469**, 143916.
347 X. Lang, W. Ma, C. Chen, H. Ji and J. Zhao, *Acc. Chem. Res.*, 2014, **47**, 355–363.
348 Q. Wang, M. Zhang, C. Chen, W. Ma and J. Zhao, *Angew. Chem., Int. Ed.*, 2010, **49**, 7976–7979.
349 Y. Ohko, T. Tatsuma, T. Fujii, K. Naoi, C. Niwa, Y. Kubota and A. Fujishima, *Nat. Mater.*, 2003, **2**, 29–31.
350 M. Barawi, L. De Trizio, R. Giannuzzi, G. Veramonti, L. Manna and M. Manca, *ACS Nano*, 2017, **11**, 3576–3584.
351 W. Wang, L. Liu, J. Feng and Y. Yin, *Small Methods*, 2017, **2**, 1700273.
352 R. Li, X. Ma, J. Li, J. Cao, H. Gao, T. Li, X. Zhang, L. Wang, Q. Zhang, G. Wang, C. Hou, Y. Li, T. Palacios, Y. Lin, H. Wang and X. Ling, *Nat. Commun.*, 2021, **12**, 1587.
353 W. Wang, M. Ye, L. He and Y. Yin, *Nano Lett.*, 2014, **14**, 1681–1686.
354 W. Wang, N. Xie, L. He and Y. Yin, *Nat. Commun.*, 2014, **5**, 5459.
355 K. Yang, X. Chen, Z. Zheng, J. Wan, M. Feng and Y. Yu, *J. Mater. Chem. A*, 2019, **7**, 3863–3873.
356 A. T. Smith, H. Ding, A. Gorski, M. Zhang, P. A. Gitman, C. Park, Z. Hao, Y. Jiang, B. L. Williams, S. Zeng, A. Kokkula, Q. Yu, G. Ding, H. Zeng and L. Sun, *Matter*, 2020, **2**, 680–696.
357 Y. Wei, B. Han, Z. Dong and W. Feng, *J. Mater. Sci. Technol.*, 2019, **35**, 1951–1958.
358 U. Joost, A. Šutka, M. Oja, K. Smits, N. Döbelin, A. Loot, M. Järvekülg, M. Hirsimäki, M. Valden and E. Nõmmiste, *Chem. Mater.*, 2018, **30**, 8968–8974.
359 R. Aleisa, J. Feng, Z. Ye and Y. Yin, *Angew. Chem., Int. Ed.*, 2022, **61**, e202203700.
360 B. Kraeutler, C. D. Jaeger and A. J. Bard, *J. Am. Chem. Soc.*, 2002, **100**, 4903–4905.
361 B. Kraeutler, H. Reiche, A. J. Bard and R. G. Hocker, *J. Polym. Sci., Polym. Lett. Ed.*, 1979, **17**, 535–538.
362 A. J. Hoffman, H. Yee, G. Mills and M. R. Hoffmann, *J. Phys. Chem.*, 1992, **96**, 5540–5546.
363 C. Lü, Y. Cheng, Y. Liu, F. Liu and B. Yang, *Adv. Mater.*, 2006, **18**, 1188–1192.
364 A. J. Hoffman, G. Mills, H. Yee and M. R. Hoffmann, *J. Phys. Chem.*, 1992, **96**, 5546–5552.
365 R. Ojah and S. K. Dolui, *J. Photochem. Photobiol., A*, 2005, **172**, 121–125.
366 J. Wang and X. Ni, *J. Appl. Polym. Sci.*, 2008, **108**, 3552–3558.
367 C. Dong and X. Ni, *J. Macromol. Sci., Part A: Pure Appl. Chem.*, 2004, **41**, 547–563.
368 Z. Y. Huang, T. Barber, G. Mills and M. B. Morris, *J. Phys. Chem.*, 1994, **98**, 12746–12752.

369 H. Kong, J. Song and J. Jang, *Environ. Sci. Technol.*, 2010, **44**, 5672–5676.

370 X. Wang, Q. Lu, X. Wang, J. Joo, M. Dahl, B. Liu, C. Gao and Y. Yin, *ACS Appl. Mater Interfaces*, 2016, **8**, 538–546.

371 Q. Zhang, D. Q. Lima, I. Lee, F. Zaera, M. Chi and Y. Yin, *Angew. Chem., Int. Ed.*, 2011, **50**, 7088–7092.

372 X. L. García-Montelongo, A. Martínez-de la Cruz, S. Vázquez-Rodríguez and L. M. Torres-Martínez, *Mater. Res. Bull.*, 2014, **51**, 56–62.

373 P. A. Kots, S. Liu, B. C. Vance, C. Wang, J. D. Sheehan and D. G. Vlachos, *ACS Catal.*, 2021, **11**, 8104–8115.

374 P. A. Zapata, A. Zenteno, N. Amigó, F. M. Rabagliati, F. Sepúlveda, F. Catalina and T. Corrales, *Polym. Degrad. Stab.*, 2016, **133**, 101–107.

375 R. E. Day, *Polym. Degrad. Stab.*, 1990, **29**, 73–92.

376 A. X. Gao, J. D. Bolt and A. A. Feng, *Plast., Rubber Compos.*, 2008, **37**, 397–402.

377 C. Anton-Prinet, G. Mur, M. Gay, L. Audouin and J. Verdu, *Polym. Degrad. Stab.*, 1998, **61**, 211–216.

378 A. Rahimi and J. M. García, *Nat. Rev. Chem.*, 2017, **1**, 0046.

379 T. El Darai, A. Ter-Halle, M. Blanzat, G. Despras, V. Sartor, G. Bordeau, A. Lattes, S. Franceschi, S. Cassel, N. Chouini-Lalanne, E. Perez, C. Déjugnat and J.-C. Garrigues, *Green Chem.*, 2024, **26**, 6857–6885.

380 R. S. Braido, L. E. P. Borges and J. C. Pinto, *J. Anal. Appl. Pyrolysis*, 2018, **132**, 47–55.

381 N. Daraboina and G. Madras, *Ind. Eng. Chem. Res.*, 2008, **47**, 6828–6834.

382 B.-S. Kang, S. G. Kim and J.-S. Kim, *J. Anal. Appl. Pyrolysis*, 2008, **81**, 7–13.

383 L. Wimberger, G. Ng and C. Boyer, *Nat. Commun.*, 2024, **15**, 2510.

384 T. Uekert, C. M. Pichler, T. Schubert and E. Reisner, *Nat. Sustainable*, 2021, **4**, 383–391.

385 O. G. Mountanea, E. Skolia and C. G. Kokotos, *Green Chem.*, 2024, **26**, 8528–8549.

386 R. Cao, D. Xiao, M. Wang, Y. Gao and D. Ma, *Appl. Catal., B*, 2024, **341**, 123357.

387 T. T. Nguyen and K. Edalati, *Chemosphere*, 2024, **355**, 141785.

388 M. Han, S. Zhu, C. Xia and B. Yang, *Appl. Catal., B*, 2022, **316**, 121662.

389 Z. Peng, R. Chen and H. Li, *ACS Sustainable Chem. Eng.*, 2023, **11**, 10688–10697.

390 S. Feng, P. T. T. Nguyen, X. Ma and N. Yan, *Angew. Chem., Int. Ed.*, 2024, e202408504, DOI: **10.1002/anie.202408504**.

391 F. Eisenreich, *Angew. Chem., Int. Ed.*, 2023, **62**, e202301303.

392 M. Zulfiqar, S. Chowdhury, S. Sufian and A. A. Omar, *J. Cleaner Prod.*, 2018, **203**, 848–859.

393 S. Weon, E. Choi, H. Kim, J. Y. Kim, H. J. Park, S. M. Kim, W. Kim and W. Choi, *Environ. Sci. Technol.*, 2018, **52**, 9330–9340.

394 Y. Ye, Y. Feng, H. Bruning, D. Yntema and H. H. M. Rijnaarts, *Appl. Catal., B*, 2018, **220**, 171–181.

395 Y. Uesugi, H. Nagakawa and M. Nagata, *ACS Omega*, 2022, **7**, 11946–11955.

396 G. Dong, Y. Wang, H. Lei, G. Tian, S. Qi and D. Wu, *J. Cleaner Prod.*, 2020, **253**, 120021.

397 E. Pino, C. Calderon, F. Herrera, G. Cifuentes and G. Arteaga, *Front. Chem.*, 2020, **8**, 365.

398 L. Wang, D. Wu, Z. Guo, J. Yan, Y. Hu, Z. Chang, Q. Yuan, H. Ming and J. Wang, *J. Alloys Compd.*, 2018, **745**, 26–32.

399 L. Minchi, F. Cao, Z. Xinni, C. Youqiang and L. Xuhua, *Chem. Phys. Lett.*, 2019, **736**, 136807.

400 C. Lv, X. Lan, L. Wang, Q. Yu, M. Zhang, H. Sun and J. Shi, *Catal. Sci. Technol.*, 2019, **9**, 6124–6135.

401 C. Ni, Y. Tang, H. R. S. Abdellatif, X. Huang, D. Xie and J. Ni, *J. Electrochem. Soc.*, 2020, **167**, 126505.

402 F. Venditti, F. Cuomo, A. Ceglie, P. Avino, M. V. Russo and F. Lopez, *Langmuir*, 2015, **31**, 3627–3634.

403 J. Shao, W. Sheng, M. Wang, S. Li, J. Chen, Y. Zhang and S. Cao, *Appl. Catal., B*, 2017, **209**, 311–319.

404 Y. Ma, L. Han, H. Ma, J. Wang, J. Liu, L. Cheng, J. Yang and Q. Zhang, *Catal. Commun.*, 2017, **95**, 1–5.

405 L. Lu, R. Shan, Y. Shi, S. Wang and H. Yuan, *Chemosphere*, 2019, **222**, 391–398.

406 L. Ji, X. Liu, T. Xu, M. Gong and S. Zhou, *J. Sol-Gel Sci. Technol.*, 2019, **93**, 380–390.

407 N. Ramesh Reddy, M. Mamatha Kumari, M. V. Shankar, K. Raghava Reddy, S. W. Joo and T. M. Aminabhavi, *J. Environ. Manag.*, 2020, **277**, 111433.

408 J. T. Park, D. J. Kim, D. H. Kim and J. H. Kim, *Mater. Lett.*, 2017, **202**, 66–69.

409 T. H. Kim, G. M. Go, H. B. Cho, Y. Song, C. G. Lee and Y. H. Choa, *Front. Chem.*, 2018, **6**, 458.

410 A. Sanchez-Martinez, O. Ceballos-Sanchez, C. Koop-Santa, E. R. López-Mena, E. Orozco-Guareño and M. García-Guaderrama, *Ceram. Int.*, 2018, **44**, 5273–5283.

411 C.-Y. Kuo, C.-H. Wu, J.-T. Wu and Y.-R. Chen, *React. Kinet., Mech. Catal.*, 2014, **114**, 753–766.

412 I. Ganesh, *Appl. Surf. Sci.*, 2017, **414**, 277–291.

413 S. Y. Mendiola-Alvarez, M. A. Hernandez-Ramirez, J. L. Guzman-Mar, L. L. Garza-Tovar and L. Hinojosa-Reyes, *Environ. Sci. Pollut. Res. Int.*, 2019, **26**, 4180–4191.

414 J. Zhao, W. Li, X. Li and X. Zhang, *RSC Adv.*, 2017, **7**, 21547–21555.

415 N. F. Jaafar, A. A. Jalil, S. Triwahyono, J. Efendi, R. R. Mukti, R. Jusoh, N. W. C. Jusoh, A. H. Karim, N. F. M. Salleh and V. Suendo, *Appl. Surf. Sci.*, 2015, **338**, 75–84.

416 S. I. Mogal, D. O. Shah, T. Mukherjee, T. Shripathi and M. K. Mishra, *ACS Omega*, 2018, **3**, 12802–12812.

417 J. Singh, N. Tripathi and S. Mohapatra, *Nano-Struct. Nano-Objects*, 2019, **18**, 100266.

418 R. Shan, L. Lu, J. Gu, Y. Zhang, H. Yuan, Y. Chen and B. Luo, *Mater. Sci. Semicond. Process.*, 2020, **114**, 105088.

419 M. Scarisoreanu, A. G. Ilie, E. Goncearenco, A. M. Banici, I. P. Morjan, E. Dutu, E. Tanasa, I. Fort, M. Stan, C. N. Mihailescu and C. Fleaca, *Appl. Surf. Sci.*, 2020, **509**, 145217.

420 Y. Wen, B. Liu, W. Zeng and Y. Wang, *Nanoscale*, 2013, **5**, 9739–9746.

421 A. Bumajdad, M. Madkour, Y. Abdel-Moneam and M. El-Kemary, *J. Mater. Sci.*, 2013, **49**, 1743–1754.

422 Y. Yu, W. Wen, X. Y. Qian, J. B. Liu and J. M. Wu, *Sci. Rep.*, 2017, **7**, 41253.

423 M. A. Ibrahem, B. G. Rasheed, R. I. Mahdi, T. M. Khazal, M. M. Omar and M. O'Neill, *RSC Adv.*, 2020, **10**, 22324–22330.

424 O. Nasr, O. Mohamed, A.-S. Al-Shirbini and A.-M. Abdel-Wahab, *J. Photochem. Photobiol., A*, 2019, **374**, 185–193.

425 K. H. Leong, H. Y. Chu, S. Ibrahim and P. Saravanan, *Beilstein J. Nanotechnol.*, 2015, **6**, 428–437.

426 K. Saeed, I. Khan, T. Gul and M. Sadiq, *Appl. Water Sci.*, 2017, **7**, 3841–3848.

427 L. Rossi, P. I. Villabrille, S. Morales-Torres and J. A. Rosso, *Mater. Chem. Phys.*, 2023, **302**, 127740.

428 Q. Wang, X. Wang, M. Zhang, G. Li, S. Gao, M. Li and Y. Zhang, *J. Colloid Interface Sci.*, 2016, **463**, 308–316.

429 A. Malankowska, A. Mikołajczyk, J. Mędrzycka, I. Wysocka, G. Nowaczyk, M. Jarek, T. Puzyn and E. Mulkiewicz, *Environ. Sci.: Nano*, 2020, **7**, 3557–3574.

430 M. A. Mahadadalkar, G. Dhakal, S. Sahoo, D. Ranjith Kumar, M. L. Baynosa, V. Q. Nguyen, M. S. Sayed, A. M. Rabie, W. K. Kim and J.-J. Shim, *J. Ind. Eng. Chem.*, 2023, **124**, 402–411.

431 O. Sacco, J. J. Murcia, A. E. Lara, M. Hernández-Laverde, H. Rojas, J. A. Navío, M. C. Hidalgo and V. Vaiano, *Mater. Sci. Semicond. Process.*, 2020, **107**, 104839.

432 T. Tang, Z. Yin, J. Chen, S. Zhang, W. Sheng, W. Wei, Y. Xiao, Q. Shi and S. Cao, *Chem. Eng. J.*, 2021, **417**, 128058.

433 X. Li, J. Xiong, Y. Xu, Z. Feng and J. Huang, *Chin. J. Catal.*, 2019, **40**, 424–433.

434 S. Fang, Y. Liu, Z. Sun, J. Lang, C. Bao and Y. H. Hu, *Appl. Catal., B*, 2020, **278**, 119316.

435 J. Liu, J. Zheng, G. Yue, H. Li, Z. Liu, Y. Zhao, N. Wang, C. Sun and Z. Cui, *RSC Adv.*, 2022, **12**, 10258–10266.

436 J. Wang, G. Wang, X. Wang, Y. Wu, Y. Su and H. Tang, *Carbon*, 2019, **149**, 618–626.

437 H. Ge, F. Xu, B. Cheng, J. Yu and W. Ho, *ChemCatChem*, 2019, **11**, 6301–6309.

438 J. Li, C. Wu, J. Li, B. Dong, L. Zhao and S. Wang, *Chin. J. Catal.*, 2022, **43**, 339–349.

439 M.-J. Ran, M. Wang, Z.-Y. Hu, Y.-F. Huang, L.-D. Wang, L. Wu, M.-M. Yuan, J. Zhang, B. Li, G. Van Tendeloo, Y. Li and B.-L. Su, *J. Mater. Sci. Technol.*, 2025, **212**, 182–191.

440 Y.-Q. Wang, C. Yang and L.-H. Gan, *Int. J. Hydrogen Energy*, 2023, **48**, 19372–19384.

441 W. Zhang, Y. Hu, C. Yan, D. Hong, R. Chen, X. Xue, S. Yang, Y. Tian, Z. Tie and Z. Jin, *Nanoscale*, 2019, **11**, 9053–9060.

442 C.-y. Huang, R.-t. Guo, W.-g. Pan, J.-y. Tang, W.-g. Zhou, H. Qin, X.-y. Liu and P.-y. Jia, *J. CO2 Util.*, 2018, **26**, 487–495.

443 D.-E. Lee, D. J. Kim, S. Moru, M. G. Kim, W.-K. Jo and S. Tonda, *Appl. Surf. Sci.*, 2021, **563**, 150292.

444 A. Meng, B. Cheng, H. Tan, J. Fan, C. Su and J. Yu, *Appl. Catal., B*, 2021, **289**, 120039.

445 C. Ban, Y. Wang, J. Ma, Y. Feng, J. Ding, Y. Duan, X. Liu, B. Zhang, J. Tang, X. Tao, L. Gan, S. Tan and X. Zhou, *Sep. Purif. Technol.*, 2023, **326**, 124745.

446 W. Ding, X. Li, S. Su, Z. Liu, Y. Cao, L. Meng, S. Yuan, W. Wei and M. Luo, *Nanoscale*, 2023, **15**, 4014–4021.

447 P. Zhang, L. Chen, D.-H. Kuo, B. Wu, Z. Su, D. Lu, Q. Wu, J. Li, J. Lin and X. Chen, *J. Mater. Chem. A*, 2024, **12**, 7163–7177.

448 L. Feng, B. Li, Y. Xiao, L. Li, Y. Zhang, Q. Zhao, G. Zuo, X. Meng and V. A. L. Roy, *Catal. Commun.*, 2021, **155**, 106315.

449 X. Zhao, Z. Li, Y. Chen, L. Shi and Y. Zhu, *Appl. Surf. Sci.*, 2008, **254**, 1825–1829.